An investigation of dynamic transitions in crowded model soft colloids

Léo GURY

UNIVERSITY OF CRETE

Contents

Acknowledgements

I would like to first start by thanking my two supervisors Dr. Dimitris Vlassopoulos and Dr. Michel Cloitre for trusting me with the task of carrying out my Ph.D. I had the chance to collaborate with two extraordinary talented scientists who are exceptionally good at what they do. A wise man told me that everybody makes mistakes, but some people makes fewer than others, and I can probably count on one hand the number of times that I was right and they were wrong. Professionally, I could probably not have found better supervisors to help me with this work, and I am grateful for that.

4 years is a long time to spend away from friends and family, so I would also like to thank Dr. Lucille Chambon for helping me through this. Greece was probably not the place where we had imagined doing our Ph.D., but I was glad she was there all this time. I am very proud of her accomplishments.

I would also like to thank the whole polymer group for always being nice and helpful with me. I know I have not been involved too much in the life of the group, but I have the highest respect for all the past and present members of this group. I am convinced that they are all incredibly smart scientists, who always manage to make things work despite the suboptimal context.

Finally I would like to thank Dr. Antonio Giuliani for his help during my PhD, even after he left. He proposed to help me design the art for the article on jammed melts of star polymers that was selected to be on the cover of the journal. Although we decided to send another design, he helped me a lot with this project and I wanted to share his version of the phase diagram (see right page).

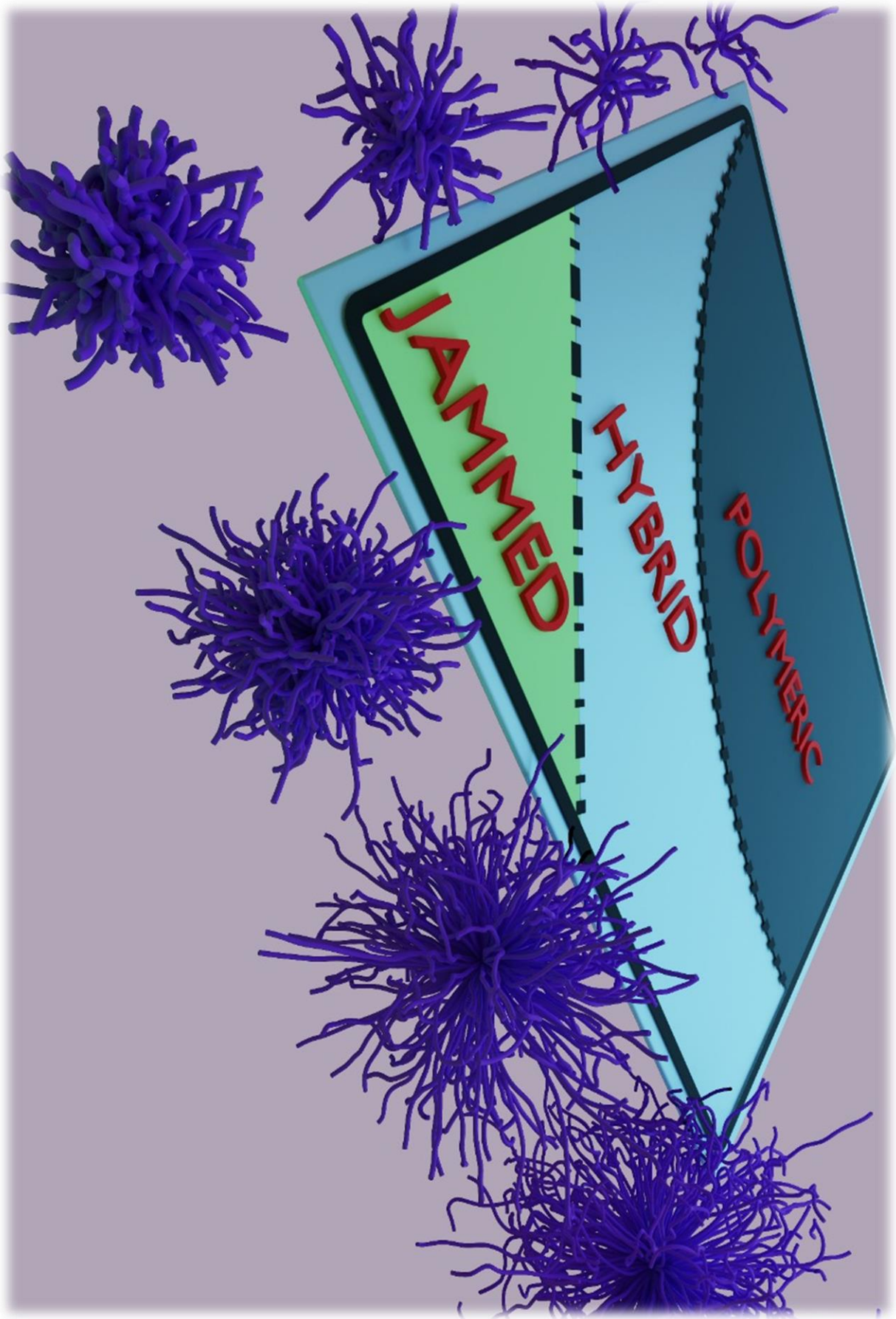
JAMMED
HYBRID
POLYMERIC

Abstract

At high packing fractions, colloidal suspensions are yield stress materials that are characterized by a solid behavior at rest and an ability to flow under a sufficient applied stress. While the formation of an organized crystalline phase may occur under certain conditions of concentration, preparation and monodipersity, most systems usually form disorganized glasses. The solid regime of hard colloids is theoretically limited by their close packing fraction (74% in the case of spheres), but the experimentally accessible limit is often the random close packing (64% for spheres) and therefore the solid regime only exist in a small range of packing fraction. The ability of soft colloids to deform and accommodate contacts (deswelling, faceting, interpenetration) extends the range of concentration at which they form a solid phase, but also complicate the evolution of the dynamic properties in this regime. As such, the systematic study of these properties requires the use of well-characterized model systems. In this work, we report on a careful examination of the rheological properties of the two main experimental model soft colloids, namely star polymers and microgel particles. In particular, we focus here on a very dense star polymer with nearly 900 short arms (5.8 $kg.mol^{-1}$ per arm). We perform a series of rheological tests both in the linear and nonlinear regime. The differences between the two systems may be attributed to the main microstructural difference, the presence of dangling chains in star polymers, which are absent in microgels. We also find striking similarities, not only between the two investigated systems, but also in the data of the available literature on soft colloids, which suggests a possible universal behavior. In particular, we find that a change in the evolution of dynamic properties inside the solid regime seems ubiquitous, and we call it jamming. Several arguments point towards a transition to a regime where elasticity becomes dominated by contacts when the packing fraction reaches values very close to 1. If proven correct, this may provide a useful link between the microstructural properties (chemical composition, softness) of soft colloids and their macroscopic rheological properties (elasticity, yielding, and behavior under flow). The objective of this work is therefore to provide and disseminate reliable data to help create solid bases for the design of novel soft materials with increased performances.

Chapter 1 – Introduction

Soft matter is a part of materials science that takes interest in the study of materials whose mechanical response is large compared to the applied stimulus. It is in direct opposition with solid mechanics, which deals with hard materials such as metals, ceramics or molecular crystals. In the field of soft matter, materials typically have elastic moduli smaller than 1MPa, thus including soft solids and liquids but excluding for example polymer glasses. It is by essence a multidisciplinary field at the border between fluid mechanics, chemistry and polymer physics. Experimental soft matter systems are aplenty, from model ones used to understand fundamental behavior to existing products on the market, with common examples being polymer melts and solutions, biological systems such as cells, bacteria, or viruses, food products such as ice cream and yogurt, and of course colloidal suspensions in the form of viscoelastic liquids, gels and glasses, which are at the center of this work.

Colloids are a type of fragmented solids similar to granular materials (powders, sand, grain …) but with the crucial property of being constituted of sub-micrometric particles. The typical size of colloids varies between 1 nanometer and 10 micrometers, therefore they are affected by molecular forces such as Van der Waals interactions, electrostatic interaction and more importantly thermal fluctuations also called Brownian motion. This gives them extremely interesting properties in terms of organization (liquid crystals, gels…) and responsiveness (temperature, ionic force, electric field…). Moreover, there small size renders their collective behavior dictated by statistical physics, and individual particles will try to explore all possible states to find their energy minimum. This is not unlike atoms and molecules, except that their bigger size shifts the associated timescales to experimentally accessible values. Originally, colloids have been viewed as large-scale replicas of atoms and molecules, and were considered a formidable substitute for the study of molecular and atomistic assemblies such as crystals and glasses[1]. Because of their ability to explore space randomly due to Brownian motion, entropy is a defining quantity at the heart of colloidal physics. At this scale, entropy is responsible for several phenomena, such as depletion, osmotic pressure, free volume interactions and

crystallization. In a nutshell, entropy ultimately governs the energy landscape, and as such, the position and motion of the whole system of particles.

There are a number of challenges in the field of colloids and an important one is to directly relate the molecular characteristics to the material properties. Many experimental techniques can be used to assess the microstructure, such as the scattering of light, X-rays or neutrons, optical and electronic microscopy or different spectroscopy techniques. Here we will mostly discuss the rheology of different soft colloidal systems. Rheology is the study of the flowing of materials. It can be applied to a wide range of flows, from geological movement of the earth crust and sea ice, to microscopic flows inside the cells. Rheology finds a crucial importance in industry as a way to design and control the properties of soft materials such as viscous liquids, pastes and gels. It has numerous application in the petrochemical industry, in the extraction of oil, but also in the handling and processing of the refined materials, like plastics and rubbers. The cosmetic and cleaning products industries also use rheology as a tool to increase their products' quality and efficiency, as well as for comfort of use and customer satisfaction. In a lot of cases, rheology is also used in quality control to ensure that a product has been properly made and that it meets its expected quality standards. For these purposes, a wide range of experiments can be designed, each probing a different aspect of the material response to deformation or flow. Because of the industrial importance of rheological properties, companies have been created long ago in order to provide reliable instruments to measure them. In this work, we will focus mostly on shear rheology, which is the study of flow in a force field parallel to the materials edges, in the absence of compression or elongation. Very well controlled geometries have become the norm in shear rheology, with the two main ones being the bob-and-cup or Couette cell and the other one the parallel plate geometry. A variant of the parallel plate geometry consists in replacing one or both of the plates by a cone with a very small yet finite angle at the tip. This ensures an equal repartition of shear inside the sample, as will be described further in Chapter 2 – Materials and Methods.

With the use of rheology, we intend here to unveil some of the mystery left around the flow and structural behaviors of model soft colloidal systems[2–9]. The goal here is not to design new materials or tune new properties, but rather to understand the physical

mechanisms behind the behavior we observe, and link microscopic structure and chemistry to macroscopic properties of the materials. There has been an increasing number of applications for yield stress fluids, but there is still progress to be made in the direction of selecting and designing materials with the right microstructure leading to improved properties[10–12]. The quantitative description of yield stress fluids is therefore needed. As such, we used here well-known model systems of the field, namely star polymers and microgels[3].

Microgels are soft colloids made of a spherical, micron-size crosslinked polymer network. In simple words, they are similar to tiny pieces of macroscopic gels which are then suspended in a medium and behave as soft colloids. In our case, the microgels we used are partially charged, which gives them the ability to swell enormously in the presence of water. More information on the swelling mechanism will be given in Chapter 2 – Materials and Methods. At the particle scale, the mechanical properties are defined mostly by the crosslink density, which is in this case almost homogeneous across the particle size and therefore the dangling ends have a negligible size compared to the particle size. At high concentration, microgels have been showed to form facets to accommodate neighbors, proving their deformability. They also contain a large amount of solvent due to osmotic pressure. These precise microgels have been studied methodically at low and intermediate concentration before[13] and have partly initiated and severely guided most of the work presented here.

Star polymers consist of a number of linear polymer chains all linked together to a common center. Apart from the chemistry of the individual arms, the two main parameters of importance for the star architecture are the branching functionality (the number of chains in a particle) and the arm length (the number of monomers in each individual arm chain). It has been shown in theory, computer simulations and experiments[14,15] that both these factors largely influence the mechanical response of star polymers, however a quantitative understanding is still missing. Star polymers belong to the group of soft colloids since they are able to swell by absorbing solvent (in good solvency conditions) and deform or interdigitate when they are confined. At the particle level, this means that both their size and shape depend on the external conditions of temperature, pressure and number density. Stars polymers have the enormous advantage

to be well-characterized systems in which chemists can systematically vary both the branching functionality and the arm length almost independently[16,17]. The use of complex synthesis procedures also allows for a very good control of the polydispersity, which makes them ideal model systems in the world of soft colloids. The star polymers are notably different from the microgels used here in that they possess long dangling ends able to interdigitate and can be prepared in the melt state, without any solvent. Indeed, contrary to microgels, they form homogeneous, mechanically coherent solids in the melt.

Figure 1 shows a cartoon representation of the qualitative phenomena at play when the concentration of colloids is increased. Starting from the dilute, liquid suspension, hard and soft colloidal suspensions first exhibit viscoelastic properties such as shear-thinning when the number density (experimentally, this means the particle concentration) is increased. Upon further increase of the concentration beyond a characteristic threshold, the material solidifies. In some cases, a colloidal crystal can be formed first, which usually turns into a solid phase called a colloidal glass. As is the case for molecular glasses, this phase consists of a dense, disorganized suspension of particles which has solid-like properties over long periods of time. Near the liquid-solid transition, the liquid or solid behavior strongly depends on the timescale of observation, thus rendering the exact definition of the transition unclear. Rheological signatures of this regime are for example the divergence of the zero-shear viscosity and the apparition of a plateau in the elastic shear modulus of the material, which becomes larger than the viscous modulus. As we dig further into the solid phase, for example by increasing the concentration, the particles get closer and form a stronger solid (increase of the elastic modulus), while the timescale related to flow is pushed to longer timescales to the point that it rapidly shifts out of the experimentally accessible range. At this point, the hindrance of particle reorganization by crowding effects makes the diffusion extremely slow, because the collective motion of several tens of particles is required. This type of density-driven slowdown of the diffusion is called “caging”, which refers to the effective cage that neighboring particles form around one test particle. This has the effect of countering Brownian motion on large length scales, and therefore the particles usually get stuck in a metastable state. Although a thermodynamically favorable state should in principle exist which has the absolute minimum of energy, the inability of the particles to

explore all states blocks the system into a local energy minimum, which it can only escape after extremely long times. This type of system is sometimes referred to as kinetically trapped or arrested and is commonly seen in a lot of different situations.

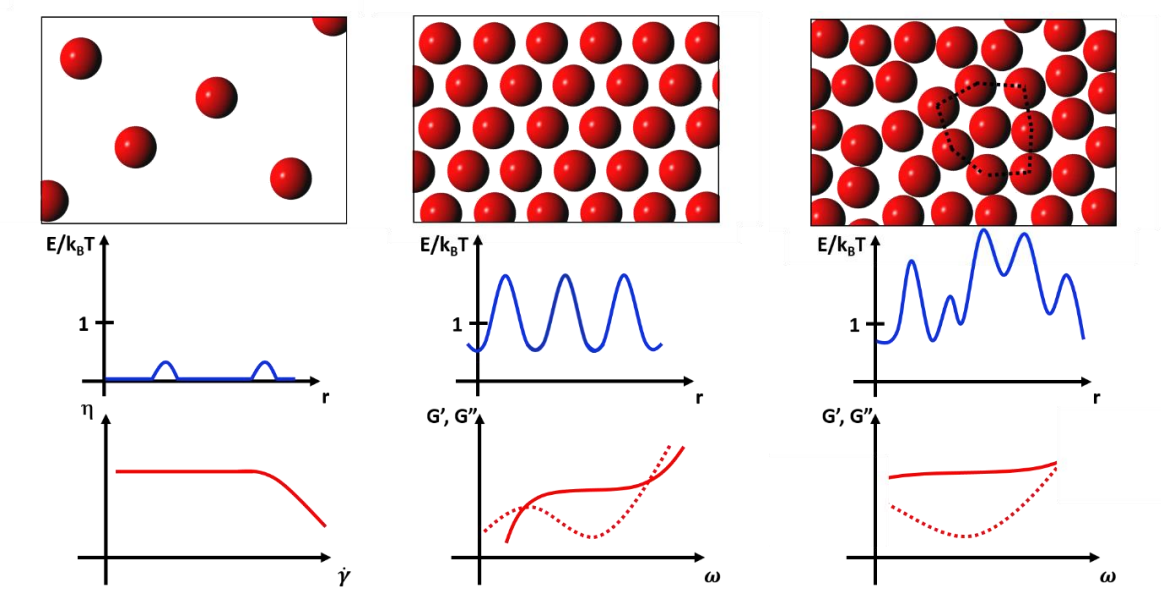

Figure 1. Top: Cartoon representation of the different phases in colloidal suspensions. Left: Liquid; center: crystal; right: glass. Middle: Typical interaction potential between particles in the different phases described above. Bottom: Rheological signature of each of the phases described above. Left: Shear-thinning liquid; center: viscoselastic solid; right: solid with very long relaxation time.

For hard spherical particles with a seemingly infinite interaction potential on contact, the maximum packing of particles is geometric and corresponds to the so-called hexagonal close packing of spheres, which is $\frac{\pi}{3\sqrt{2}}$ or about 0.74[18]. This means that there exist a theoretical maximum for the number of spherical hard colloids there can be in a given volume, and that even at this limit, only about 74% of the total volume can be occupied by the particles, the rest being either the suspending fluid or air. In the dry state, hard sphere systems usually form porous, hard and fragile materials that have poor rheological value due to their inability to flow. Although the theoretical limit is the hexagonal close packing, it is extremely difficult to obtain such high densities in practice, since this would require that all particles fall exactly in the right place. As explained above, real life experimental systems become solids at high packing fraction and therefore the relative motion of particles is effectively arrested. For this reason, the commonly obtain highest packing fraction is closer to the random close packing value of about 0.64[19], where

particles are disorganized. The beauty of large numbers and statistical physics makes it that, even though the particles form metastable states and are completely disorganized, the average over all the system gives an extremely robust value for the densest random packing. However, this also means that there can be local heterogeneities of the density throughout the sample, which can have a huge influence on flow and mechanical properties in general.

Since hard spheres only have short-range interactions on contact, the solid phase only appears in a limited range of concentration. The phase diagram of monodisperse hard spheres have been studied in depth[20], and is represented on Figure 2. From packing fraction of about 0.494, there is a coexistence of a colloidal crystal with a glass. The crystalline phase then expands up to a packing fraction of 0.545 when the whole system becomes crystalline. Above packing fractions of 0.58, the crystalline phase progressively gives way to a disorganized glass phase up to the maximum random packing of 0.64. It is important to note that polydispersity and shape both have a big influence on the phase diagram of hard particles. Although these axes will not be explored in this work, which is limited to spherical particles, we can cite as examples the considerably bigger fluid regime of polydisperse spheres, and their ability to reach much higher packing fractions[20]; and the ability of anisotropic particles like hard rods to form liquid crystals[21], which are organized states of matter with lower entropy than their disorganized counterpart. It is important to note that the maximum random packing of M&Ms is 0.68 due to their ellipsoidal shape[22].

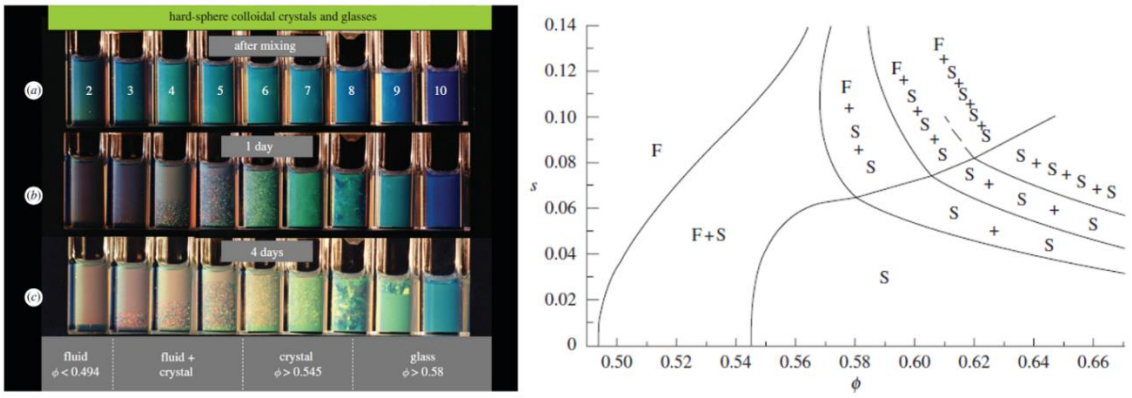

Figure 2. The phase diagram of hard spheres[20]. The left picture represents ten samples at different packing fraction of colloidal hard spheres left to equilibrate over 4 days. The right-

hand side diagram shows the multiple phases of hard sphere suspensions as a function of packing fraction ϕ and polydispersity index s.

This geometrical restriction on the maximum packing is gradually alleviated as the interaction potential of the particles is soften. Effectively, this means that the elastic modulus of the particles are progressively lowered down to values that make deformation at the particle level possible. Point contacts no longer define the maximum packing and the formation of facets[23], as can be seen in foams for instance[24], becomes a possible mechanism through which the packing fraction can be increased, this time up to values approaching unity. In fact, in the case of star polymers, which are considered extremely soft systems due to their polymeric nature[3], the existence of a coherent solid phase in the melt proves that the shape adjustment is such that the entire accessible volume can be filled with the polymer.

There are several mechanisms through which soft colloids can increase their packing fraction well above what is permitted to hard colloids. One that we have already mentioned is the change of shape. Spheres are the most symmetrical and have the lowest surface-to-volume ratio of all geometrical shapes, meaning that a lot of systems will spontaneously form spheres if they are left free to decide. Examples include polymer coils, spherical micelles, or in this case star polymers. Spheres are also the worst packing (convex) geometric shapes, and therefore the modification of the spherical shape of a colloid towards any other convex one will result in a more efficient packing[25].

Another possible mechanism to increase the number density of soft colloids is the reduction of the size of the particles, or deswelling. Since a lot of soft colloids can swell in good solvency conditions, which is the case here for microgels and stars to different degrees, their size in dilute, unconstrained conditions are usually much bigger than at higher concentrations. For stars and microgels in particular, the chemical potential of the solvent must be equal inside and outside of the particle, which tends to homogenize the concentration throughout the sample. Since the solute concentration is higher inside the particle than outside, where it is null, there is a strong osmotic pressure difference between the inside and the outside of the particle, with the particle boundaries effectively acting as a semi-permeable membrane in this case. Molecules of solute (here, monomers), are kept inside the particle by covalent bonds while solvent molecules are

free to move through. Therefore this osmotic pressure tends to pull the solvent molecules inside the particles to decrease the local concentration of solute, effectively swelling the particle size. This effect is compensated by the stretching of the polymer chains, which acts as springs against the total dissolution of the colloid, therefore reaching an equilibrium at a swollen yet finite size. The position of the equilibrium therefore depends on the local concentration of solute and the energy required to stretch a polymer chains, which both can be tuned by carefully designing the particle architecture. In the case of the microgels studied here, this effect is driven further towards the swelling of the particle by the presence of counter-ions near the charged polymers composing the microgels. In this case, additionally to the osmotic pressure due to the presence of the polymer, there is an additional osmotic term coming from the homogenization of the ion concentration that causes a larger swelling.

Finally, star polymers also exhibit another way to accommodate a higher number density by interdigitating. Indeed, by construction, they possess long dangling ends (with size comparable to the particle size), which may allow for the effective sharing of the same volume by two or more neighboring stars. This effect has been studied in the past and computer simulations have shown that low functionality stars may even share the same center of mass[26], similarly to linear polymer coils. However, the increase of functionality rapidly prevents this from happening, leaving a smaller volume accessible for interpenetration. Ultimately, this provides a striking similarity with grafted nanoparticles, which usually consists of a hard core grafted with polymeric chains. Such particles cannot share the same center of mass because of the hard interaction of the cores, but are considered soft because of the possible interpenetration of the polymeric arms. For stars however, the unavailable volume at the center depends mainly on the branching functionality[15,27], whereas grafted nanoparticle inter-particle distance is ultimately limited by their core size.

All of the above-mentioned arguments have a severe influence on the rheological properties of soft colloids, especially when the concentration is increased to values where the contacts between particles become important. In this regime, our microgels and star polymers of interest form a disorganized solid phase. However, there have been evidence of an additional transition inside the glass regime of microgels[13], characterized by a

different rheological behavior. The primary goal of this work is to understand this transition that we call jamming, and to assess its existence in other soft systems, namely here star polymers. This problematic is summed up in Figure 3, with a particular emphasis on the role of softness on the phase diagram and especially on the jamming transition.

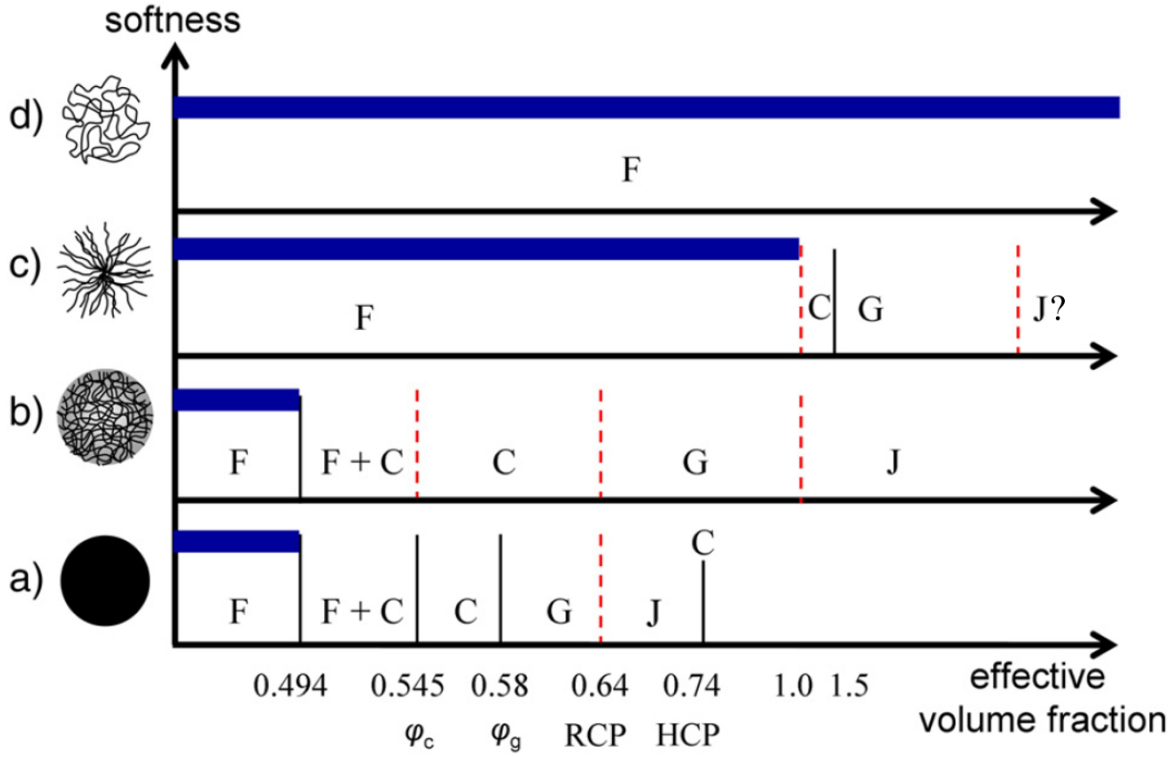

Figure 3. Comparison of the simplified phase diagram of soft and hard spherical colloids. The typical softness increases from bottom (hard sphere) to top (polymer coil). The two main intermediate systems – microgels and stars – are also represented. The jamming regime of star polymers remains unclear. F=fluid; C=crystal; G=glass; J=jamming.

After a second chapter (Chapter 2 – Materials and Methods) in which all the samples and the experimental protocols will be described, Chapter 3 – Colloidal jamming in multiarm star polymer melts[28], will focus on the study of extremely high branching functionality star polymers in the melt. This chapter described in depth the differences between star polymers and regular linear polymers and concludes on the presence of a solid regime even at infinitely long timescales that replaces terminal flow and that we attribute to the colloidal jamming of the stars. Comparison with an abundant literature on the matter shows that there might be a universal behavior of stars and grafted particles that we present under the form of a state diagram differentiating between the polymeric-dominated regime, a hybrid transitional regime and a colloidal-dominated regime.

Then Chapter 3 – Jamming of concentrated solutions of microgels and star polymers, will focus on the evolution of the jammed state in star polymers with concentration and its rheological signatures. This chapter will heavily rely on a systematic comparison with the better studied microgels to draw parallels between the two systems. It also concludes on the differences that can be seen in the rheological behavior of these two model systems and gives an interpretation regarding the mechanisms leading to these differences. Finally, an attempt at scaling the shear elasticity in a variety of jammed soft systems points towards a potential universality in soft colloids.

Chapter 4 – Stress relaxation and internal stresses, will deal mostly with the very rich rheological response of star polymer melts and suspensions during and after steady flows. Once again, we draw parallels with the behavior of microgels, also pointing out some quantitative differences that make high functionality stars a unique system amongst soft colloids. In particular, residual stresses after flow are meticulously described and measured, and their link to ageing, creep and stress relaxation is investigated.

Chapter 5 – Structural changes in an ageing star polymer glass and Chapter 6 – The second virial coefficient of grafted nanoparticles in dilute regime, report on other projects related to the study and characterization of soft colloids. Chapter 5 mostly describes an experimental technique consisting of a dynamic light scattering (DLS) experiment in a sheared cell. This provides an efficient tool to investigate the structure of a star polymer glass after shear, which exhibits unusual time-dependent properties. Chapter 6 reports on a comparison of different grafted nanoparticles in the dilute regime and the influence of the particle architectures on their interaction potentials. To do that, we use static and dynamic light scattering to measure the second virial coefficient, indicative of the interactions between particles, and compare our findings to a simple theoretical model for grafted nanoparticles.

References

(1) Mattsson, J.; Wyss, H. M.; Fernandez-Nieves, A.; Miyazaki, K.; Hu, Z.; Reichman, D. R.; Weitz, D. A. Soft Colloids Make Strong Glasses. *Nature* **2009**, *462* (7269), 83–86. https://doi.org/10.1038/nature08457.

(2) Löwen, H. Colloidal Soft Matter under External Control. *Journal of Physics: Condensed Matter* **2001**, *13* (24), R415–R432. https://doi.org/10.1088/0953-8984/13/24/201.

(3) Vlassopoulos, D.; Cloitre, M. Tunable Rheology of Dense Soft Deformable Colloids. *Curr. Opi. Colloid Int. Sci.* **2014**, *19* (6), 561–574. https://doi.org/10.1016/j.cocis.2014.09.007.
(4) Vlassopoulos, D.; Cloitre, M. Bridging the Gap between Hard and Soft Colloids. *Soft Matter* **2012**, *8* (15), 4010–4013. https://doi.org/10.1039/C2SM90031A.
(5) Mewis, J.; Wagner, N. J. *Colloidal Suspension Rheology*; Cambridge series in chemical engineering; Cambridge University Press: Cambridge ; New York, 2012.
(6) Vlassopoulos, D.; Fytas, G. From Polymers to Colloids: Engineering the Dynamic Properties of Hairy Particles. In *High Solid Dispersions*; Cloitre, M., Ed.; Advances in Polymer Science; Springer Berlin Heidelberg, 2009; pp 1–54.
(7) Royall, C. P.; Poon, W. C. K.; Weeks, E. R. In Search of Colloidal Hard Spheres. *Soft Matter* **2012**, *9* (1), 17–27. https://doi.org/10.1039/C2SM26245B.
(8) Frigaard, I. Simple Yield Stress Fluids. *Curr. Opi. Colloid Int. Sci.* **2019**, *43*, 80–93. https://doi.org/10.1016/j.cocis.2019.03.002.
(9) Philippe, A.-M.; Truzzolillo, D.; Galvan-Myoshi, J. The Glass Transition of Soft Colloids. 10.
(10) Jaeger, H. M. Celebrating Soft Matter's 10th Anniversary: Toward Jamming by Design. *Soft Matter* **2015**, *11* (1), 12–27. https://doi.org/10.1039/C4SM01923G.
(11) Nelson, A. Z.; Ewoldt, R. H. Design of Yield-Stress Fluids: A Rheology-to-Structure Inverse Problem. *Soft Matter* **2017**, *13* (41), 7578–7594. https://doi.org/10.1039/C7SM00758B.
(12) Nelson, A. Z.; Schweizer, K. S.; Rauzan, B. M.; Nuzzo, R. G.; Vermant, J.; Ewoldt, R. H. Designing and Transforming Yield-Stress Fluids. *Current Opinion in Solid State and Materials Science* **2019**. https://doi.org/10.1016/j.cossms.2019.06.002.
(13) Pellet, C.; Cloitre, M. The Glass and Jamming Transitions of Soft Polyelectrolyte Microgel Suspensions. *Soft Matter* **2016**, *12* (16), 3710–3720. https://doi.org/10.1039/C5SM03001C.
(14) Ren, J. M.; McKenzie, T. G.; Fu, Q.; Wong, E. H. H.; Xu, J.; An, Z.; Shanmugam, S.; Davis, T. P.; Boyer, C.; Qiao, G. G. Star Polymers. *Chemical Reviews* **2016**. https://doi.org/10.1021/acs.chemrev.6b00008.
(15) Likos, C. N.; Löwen, H.; Watzlawek, M.; Abbas, B.; Jucknischke, O.; Allgaier, J.; Richter, D. Star Polymers Viewed as Ultrasoft Colloidal Particles. *Phys. Rev. Lett.* **1998**, *80* (20), 4450.
(16) Roovers, J.; Zhou, L. L.; Toporowski, P. M.; van der Zwan, M.; Iatrou, H.; Hadjichristidis, N. Regular Star Polymers with 64 and 128 Arms. Models for Polymeric Micelles. *Macromol.* **1993**, *26* (16), 4324–4331. https://doi.org/10.1021/ma00068a039.
(17) Gauthier, M.; Munam, A. Synthesis of 1,4-Polybutadiene Dendrimer−Arborescent Polymer Hybrids. *Macromolecules* **2010**, *43* (8), 3672–3681. https://doi.org/10.1021/ma1004056.
(18) Hales, C. The Sphere Packing Problem. 36.
(19) Jaeger, H. M.; Nagel, S. R. Physics of the Granular State. *Science* **1992**, *255* (5051), 1523–1531. https://doi.org/10.1126/science.255.5051.1523.
(20) Pusey, P. N.; Zaccarelli, E.; Valeriani, C.; Sanz, E.; Poon, W. C. K.; Cates, M. E. Hard Spheres: Crystallization and Glass Formation. *Philosophical Transactions of the Royal Society A: Mathematical, Physical and Engineering Sciences* **2009**, *367* (1909), 4993–5011. https://doi.org/10.1098/rsta.2009.0181.

(21) Cortes, L. B. G.; Gao, Y.; Dullens, R. P. A.; Aarts, D. G. A. L. Colloidal Liquid Crystals in Square Confinement: Isotropic, Nematic and Smectic Phases. *Journal of Physics: Condensed Matter* **2017**, *29* (6), 064003. https://doi.org/10.1088/1361-648X/29/6/064003.
(22) Donev, A. Improving the Density of Jammed Disordered Packings Using Ellipsoids. *Science* **2004**, *303* (5660), 990–993. https://doi.org/10.1126/science.1093010.
(23) Bouhid de Aguiar, I.; van de Laar, T.; Meireles, M.; Bouchoux, A.; Sprakel, J.; Schroën, K. Deswelling and Deformation of Microgels in Concentrated Packings. *Scientific Reports* **2017**, *7* (1). https://doi.org/10.1038/s41598-017-10788-y.
(24) Weaire, D. The Rheology of Foam. *Curr. Opi. Colloid Int. Sci.* **2008**, *13* (3), 171–176. https://doi.org/10.1016/j.cocis.2007.11.004.
(25) Chen, E. R.; Klotsa, D.; Engel, M.; Damasceno, P. F.; Glotzer, S. C. Complexity in Surfaces of Densest Packings for Families of Polyhedra. *Physical Review X* **2014**, *4* (1). https://doi.org/10.1103/PhysRevX.4.011024.
(26) Vlassopoulos, D.; Pakula, T.; Fytas, G.; Roovers, J.; Karatasos, K.; Hadjichristidis, N. Ordering and Viscoelastic Relaxation in Multiarm Star Polymer Melts. *EPL (Europhysics Letters)* **1997**, *39* (6), 617.
(27) Daoud, M.; Cotton, J. P. Star Shaped Polymers : A Model for the Conformation and Its Concentration Dependence. *Journal de Physique* **1982**, *43* (3), 531–538. https://doi.org/10.1051/jphys:01982004303053100.
(28) Gury, L.; Gauthier, M.; Cloitre, M.; Vlassopoulos, D. Colloidal Jamming in Multiarm Star Polymer Melts. *Macromol.* **2019**, *52* (12), 4617–4623. https://doi.org/10.1021/acs.macromol.9b00674.

Chapter 2 – Materials and Methods

2.1 – Materials

Polymers

Details of the synthesis of the high functionality (f>150) star polymers were published by Gauthier et al.[1]. Carbosilane dendrimers were used to provide a chemical core for the stars. Short polybutadiene chains (M_n=1.2kg.mol^{-1}) containing around 50% of 1,2-polybutadiene were grafted onto the cores to form star-like hybrids. The dangling double bonds of the polybutadiene short chains were then used as coupling sites for the grafting of longer chains of 1,4-polybutadiene, yielding a star-like structure with a large number of arms. In this study, the RS128-PBD5 star was used. The stars used in this study have a number-average branching functionality f_n=875 arms and a number-average molar mass M_n=5.8kg.mol^{-1} per arm or a number-average branching functionality of f_n=929 arms number-average molar mass M_n=4.0kg.mol^{-1} per arm. Lower functionality star polymers (f<150) were synthesized[2–4] by direct addition of the long polybutadiene chains onto the dendritic carbosilane cores of different generations to yield 32, 64 or 128 theoretical arms. The star molar mass and the molar mass of the arms were measured independently by light scattering and vapor pressure osmometry respectively[2], yielding an accurate measure of the functionality (the coupling reaction is not complete). The details of all the polymers used in this work are given in Table 2-1. Note that a linear polybutadiene was studied as well for reference (see chapter 3). All polybutadienes have the same microstructure (>90% 1,4-addition based on NMR)[5].

Squalene was used as a good solvent for polybutadiene 1,4-addition. It was appropriate for rheological measurements because of its low toxicity and very high boiling point (T_b=275°C) at atmospheric pressure. Cyclohexane, an athermal co-solvent, was added to ensure a homogeneous dissolution. A small amount (<2mg) of 2,6-di-tert-butyl-p-cresol (>99% purity from Fluka) was added to prevent oxidization of the sample without any noticeable influence on the experiments. After one day of mixing under constant

gentle stirring (homogeneity could be asserted by eye), the samples were exposed to ambient conditions of temperature and pressure until most of the cyclohexane was evaporated. The samples were then placed in vacuum until their mass remained constant over time, ensuring that the cyclohexane was completely evaporated. Due to the small amount of original star sample available, all investigated solutions were prepared by successive dilution of the previous one, starting from the melt.

Table 2-1. Molecular characteristics of star and linear polymers

Code	Structure	f	M_a (kg.mol^{-1})	$Đ_{arm}$ (M_w/M_n)	T_g (°C)	M_{star} (kg.mol^{-1})	PDI_{star} ($M_{w,star}/M_{n,star}$)	R_h (nm)
Linear 155K	Linear	1	155	-	-96	155	-	-
6407	Star	62	6.3	-	-92	403	-	10.9
12807	Star	12	6.8	-	-92	870	-	14.2
RS128PBD3	Star	39	24.4	1.06	-	8600	1.14	40
RS128PBD5	Star	87	5.8	1.13	-93	5300	1.08	23
RS64PBD5	Star	92	4.0	1.1	-93	3800	1.03	21

f: number-average functionality (number of arms); M_a: number-average molar mass of one star arm; $Đ_{arm}$: Dispersity of the star arms; T_g: glass transition temperature (DSC); M_{star}: molar mass of the entire particle; PDI_{star}: Polydispersity index of the entire star; R_h: hydrodynamic radius in athermal solvent (cyclohexane, DLS).

Microgels

Microgels are spherical crosslinked polymer networks synthesized by emulsion polymerization[6]. Those employed in this work were made of a random co-polymer containing on average 64 wt% of ethyl acrylate, 35 wt% of methacrylic acid and 1 wt% of dicyclopentenyl-oxyethyl methacrylate acting as a bifunctional crosslinker. The synthesis was carried out at low pH to avoid the deprotonation of the methacrylic acid moieties. The starved conditions of the reaction ensured a good homogeneity of the crosslinker throughout the particle[7], thus limiting the size of the dangling chains. The virtual absence of dangling chains is a key feature of these microgels, which has a significant importance on their rheological behaviour[8]. At pH>5, the deprotonation of the methacrylic acid moieties introduces negative charges attached to the polymer network. These charges attract the positive free counterions (in most cases sodium ions Na^+) in solution due to electrostatic interactions, which in turn displaces the osmotic balance inside and outside of the microgel particles. The presence of a big number of counterions inside the particles

attracts water molecules due to the effective osmotic pressure difference, causing a significant swelling of the particles (up to 1000 times the initial volume)[9]and consequently a huge increase of the volume fraction. This property allows the microgel particles to form solid phases at about 1 wt%.

The microgels we used in this work have a swollen hydrodynamic radius in the completely swollen (pH=7), dilute regime of 300 nm. We estimate the overlap concentration from the liquid-to-solid transition in water: c*=0.9 wt%. The osmotic equilibrium responsible for the swelling of the microgels is changed when the concentration is varied, and therefore we expect the microgels to deswell significantly with increasing concentration[10,11]. At contact, the osmotic equilibrium is broken (not enough water) and the size of the particles is mostly governed by the available volume (faceting)[6,9].

Grafted nanoparticles

Grafted nanoparticles composed of a silica core and polystyrene (PS) chains[12–14] were used in chapter 6. Their structural and chemical characteristics are given in Table 2-2. The use of surface-initiated ATRP as the synthesis method allows for the dense grafting of long polymer chains on the surface.

Table 2-2.Molecular characteristic of the Si-PS grafted nanoparticles

Code	DP	M_a (kg.mol^{-1})	M_w (10^6 kg.mol^{-1})	f	R_0 (nm)	σ (nm^{-2})	Rh (nm)	R (nm)
DP130	135	14	1.3	24900	57	0.61	97	80
DP440	441	46	2.1	24900	57	0.61	123	125
DP790	788	82	2.7	21200	57	0.52	170	155
DP980	981	102	3.0	20000	57	0.49	224	171
DP2690	2692	280	6.3	19200	57	0.47	436	343
DP480	480	50	1.8	13100	59	0.3	140	180
DP1170	1170	122	1.6	3500	59	0.08	145	142
DP1300	1300	135	4.3	23200	59	0.53	190	171
DP2480	2480	258	5.5	17100	59	0.39	430	227

DP: degree of polymerization (number of monomers per chain); M_a: weight-average molar mass of one grafted chain (arm); M_w: weight-average molar mass of the particle; f: equivalent functionality (number of grafted chains); R_0: silica core radius; σ: grafting density; R_h: hydrodynamic radius of the particle (DLS); R_{SLS}: radius of the particle (SLS).

Other grafted nanoparticles with a silica core and polymethyl methacrylate (PMMA) chains were also used in chapter 6. They were synthesized using surface-initiated ATRP (grafting from) to achieve a high grafting density. Details of synthesis have been published by Ohno et al.[15]. Their molecular characteristics are listed in Table 2-3. The samples were diluted in the good solvent toluene and a mixture of slightly worse solvents o-dimethoxy benzene (Veratrole) and dimethyl formamide (DMF).

Table 2-3. Molecular characteristic of the Si-PMMA grafted nanoparticles

Code	DP	M_a ($kg.mol^{-1}$)	M_w (10^6 $kg.mol^{-1}$)	f	R_0 (nm)	σ (nm^{-2})	R_h (nm)	R_{SLS} (nm)
PMMA 41-ver/DMF	410	41	2.8	34500	65	0.65	133	133
PMMA 41-toluene	410	41	2.8	34500	65	0.65	123	119
PMMA 402-ver/DMF	4020	402	15.25	34500	65	0.65	420	396
PMMA 41-toluene	4020	402	15.25	34500	65	0.65	470	382

DP: degree of polymerization (number of monomers per chain); M_a: weight-average molar mass of one grafted chain; M_w: weight-average molar mass of the particle; f: equivalent functionality (number of grafted chains); R_0: silica core radius; σ: grafting density; R_h: hydrodynamic radius of the particle (DLS); R_{SLS}: radius of the particle (SLS)

2.2 – Instruments

Melt rheology

Linear viscoelastic spectra were obtained on a strain-controlled shear rheometer (ARES from TA, USA) equipped with 8 mm diameter stainless steel parallel plates and a convection oven for temperature control. Nitrogen gas was used to regulate the temperature inside the oven between -100°C and +40°C. At each temperature thermal equilibration was ensured by means of dynamic time sweep measurements in the linear regime.

Solution rheology

Rheological experiments with the star and microgel solutions were performed on a Physica MCR 501 rotational shear rheometer from Anton Paar (Austria). Although the instrument is ultimately stress-controlled, the feedback loop was fast enough to use it in

strain-controlled mode on the time scale of the experiments. A standard 60mm metallic bottom plate was used as the lower measuring tool, which was connected to a Peltier unit for temperature control. The temperature was not varied in the experiments and kept to a constant value of 23°C. Four different metallic cones were used as the upper measuring tool depending on the concentration of the samples. For very high concentrations (c_{star}>80 wt%; $c_{microgel}$>10 wt%), an 8mm diameter cone with an angle of 1° was used. For intermediate concentrations, (50 wt%<c_{star}<80 wt%; 5 wt%<$c_{microgel}$<10 wt%), a 12.5mm diameter cone with an angle of 1° was used. For low concentrations (15% wt < c_{star} <50%wt; 1 wt%< $c_{microgel}$<5 w%), a 25mm diameter cone with an angle of 2° was used. For dilute concentrations (c_{star}<15% wt), a 50mm diameter cone with an angle of 1° was used.

Light scattering

Light scattering was performed for the characterization of dilute samples of stars, microgels and grafted particles. We used a commercial ALV-5000 (Germany) instrument equipped with a goniometer. The angle between the incident and the scattered light was varied between 30° and 150°. An Nd-YAG LASER with a wavelength of 532 nm (green) and a power of 120mW was used as the light source. Filters can be added on the optical path to lower the incident power for strongly scattering samples. The VV polarization geometry was used (both incident and scattered beam were polarized vertically with respect to the scattering plane). The temperature of the bath containing the sample was fixed at 20°C for all experiments.

2.3 – Protocols

Sample loading

The choice of the tool is essential because a compromise must be reached between the amount of available sample, the torque detection level and the ability to load the sample in the gap. Indeed, the selected tool must be large enough to ensure a good detection of the signal. However, when dealing with highly elastic pastes with a long relaxation time, as it is the case for these samples at high concentrations, the loading of the sample is difficult due to the inability of the material to easily squeeze in between the

two parts of the tool, creating significant normal forces. By default, the maximum normal force is capped by the Physica 501 rheometer at 15N, well below the maximum normal force level of 50N after which the instrument may suffer permanent damage. Since the relaxation of these normal forces can be extremely long (hours or days), we accelerated the relaxation process by applying large amplitude oscillations (>100%) as the upper tool was lowered. This method was proven to be very efficient to reduce the loading times from potential hours to about 15 minutes. In particular for microgels, the loading time is a critical parameter since water evaporates rather fast compared to the time frame of the experiment, despite the necessary precautions taken. When approaching the gap position, the amplitude of the oscillations was usually reduced (20%) to ensure the best possible loading of the sample.

Time-temperature superposition

For melts of star polymers, time-temperature superposition (TTS) was used to effectively cover a frequency range typically inaccessible to this type of rheometer, allowing measurements of the linear rheological properties of the polymers over about 14 decades of frequency. At each temperature, a dynamic frequency sweep (DFS) test was performed from 100 rad/s to 0.1 rad/s at a constant strain of 5%. For the lower temperature measurements, this strain was lowered to 1%. For each sample, it was ensured that all the strains used were within the linear regime (measurements at different strain amplitudes gave the same results). It was also ensured that each data set could be superimposed over at least one decade of frequency by adjusting the temperature difference between sets. The master curves are presented at the same distance from T_g, with a reference temperature $T_{ref}=T_g+73K$.

Shift factors were calculated both using the ARES Orchestrator software and manually. The horizontal shift factors were obtained by shifting the phase angle data to obtain a master curve, while the vertical shift factors were taken from the density change of 1,4 polybutadiene[16]. Very good agreement was found with the shift factor calculation based on the software (see chapter 3). The data were eventually horizontally shifted by a constant to account for the slightly different glass temperatures (T_g) of the different polymers. All the data shown below are represented at the same distance from T_g, such that the phase angle data close to the glass region superimpose. This shift is almost

negligible due to the small difference in T_g among the polymers (Table 2-1). The good quality of the master curves is confirmed by the sensitive van Gurp –Palmen plot[17] (see Chapter 3, Figure A3-2). Based on these results one may safely conclude that both polymeric and colloidal modes are governed by the monomeric friction, which is a consequence of the fact that the fraction of the real chemical core (which has different friction) in these stars is very small.

Rejuvenation protocol

Since the high-concentration solutions of stars and microgels have such long relaxation times, a rejuvenation protocol was used prior to any rheological test to ensure that the samples were put in the same reproducible state each time. We will show in chapters 4 and 5 that the choice of this protocol has a significant impact on the subsequent measurements, but the aim of this step is to provide a reproducible starting point. Several studies have addressed the steady shear rejuvenation protocols involving the shearing of the sample at a constant (high) shear rate to ensure the liquefaction of the sample and the erasing of any prior history[6,18]. We find that such protocols can be tricky, often resulting in the expulsion of part of the sample outside of the gap of the instrument. Moreover, such high shearing is not necessary to effectively erase any prior shear history. We opted for a much more gentle oscillatory rejuvenation in the nonlinear regime, which typically consists of large-amplitude oscillations (γ_0=100 %, ω=1 rad.s^{-1}) for 60s.

As will be further discussed in chapter 5, the duration of the rejuvenation protocol directly influences the direction of the stored internal stress in the material. The normal stress is always pushing towards the 0 strain position. Therefore, in the case of a rejuvenation as described above, the last oscillation cycle stops at a strain of sin(60)=-0.3 and the normal stress is positive. The duration of the oscillatory rejuvenation can be changed, and this will be discussed in chapter 5.

Following the rejuvenation protocol, different rheological measurements were performed. Unless specified otherwise, a measurement was performed immediately after the rejuvenation protocol (no waiting time). For all samples, we always performed first a strain sweep at an angular frequency ω=1 rad.s^{-1} and deformation amplitude between

γ_0=0.01 % and γ_0=500 % (or until the signal was lost due to low torque limitations) to estimate the linear regime of the viscous (G") and the elastic (G') moduli. The linear regime was characterized by strain-independent moduli (G', G") (Figure 2-1). The stress was also measured and the oscillatory yield strain and yield stress was determined at the intersection of the high deformation and low deformation asymptotes of the obtained stress curve (Figure 2-1).

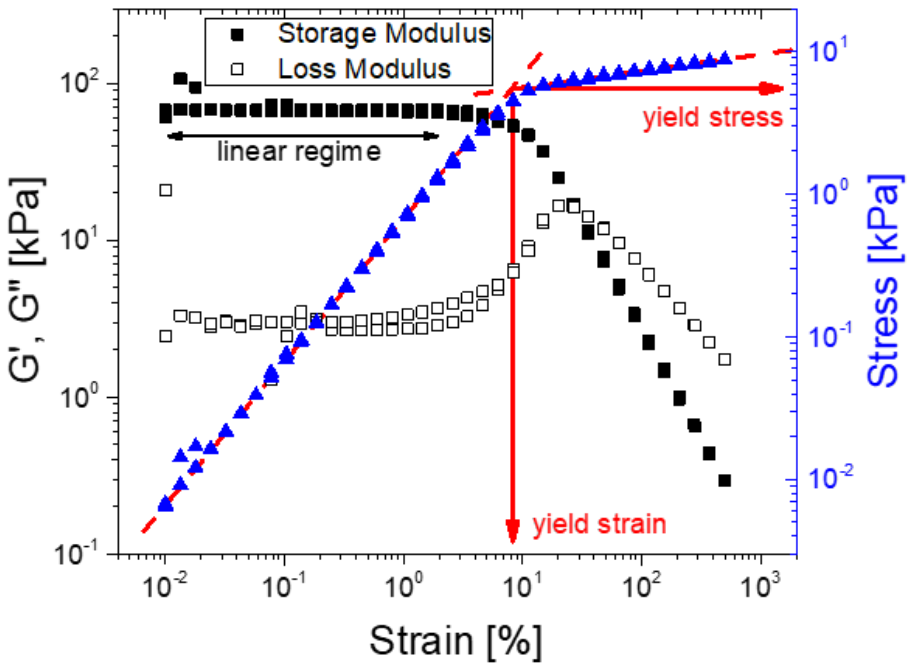

Figure 2-1. Typical strain sweep measurement of stars and microgels in the solid regime. This data come from the measurement of a 3c (50 wt%) solution of star RS128PBD5 in squalene, but the qualitative features of the curve are similar for all solid samples. The black squares represent the elastic (filled) and viscous (empty) moduli which can be read on the left axis. The horizontal black double arrow represents the extent of the linear regime (limited at low strain amplitudes by the resolution of the instrument). The blue triangles represent the stress, which can be read on the right axis. The red arrows point to the yield strain (horizontal) and the yield stress (vertical).*

Afterwards, a frequency sweep at angular frequencies between ω=100 rad.s^{-1} and ω=0.01 rad.s^{-1} (or until the signal was lost due to low torque) and maximum deformation γ_0=1% was carried out to obtain the elastic (G') and viscous (G") moduli. In some cases of interest, the range of frequency was extended up to 6000 rad.s-1 with the help of a homemade high-frequency rheometer equipped with a piezoelectric transducer[19] (Figure 2-2). Note that for solutions we did not use TTS to avoid any change of solvent quality,

hence particle interactions (though star polymers in squalene were shown to obey TTS albeit over a limited temperature range[20]). In the solid regime, the stars and the microgels typically display a higher G' relatively to the G", and the plateau modulus value is taken as the value of G' at the frequency where G" is minimum (Figure 2-2). The G' and G" crossover at low frequencies rapidly disappear from the accessible frequency range when the concentration of stars or microgels is increased.

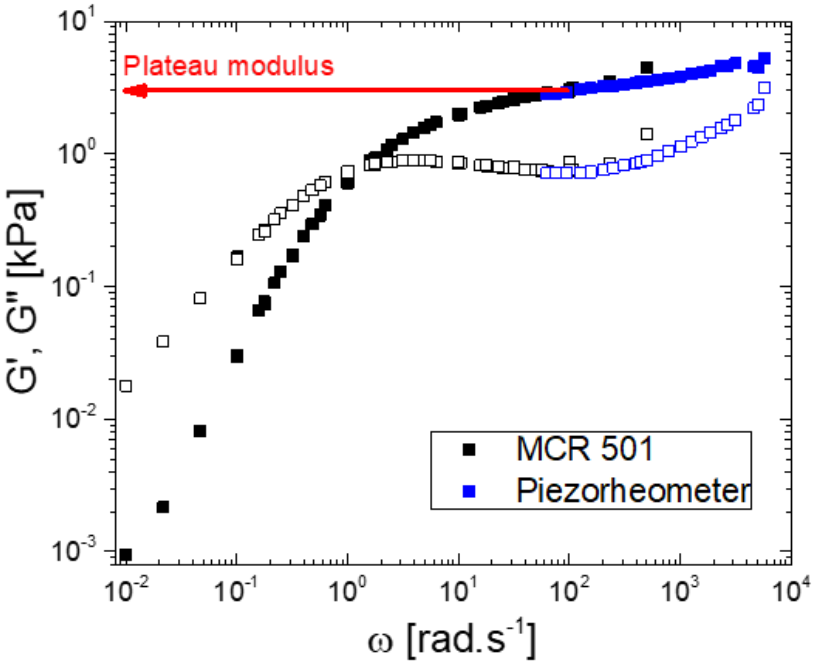

Figure 2-2. Typical dynamic frequency sweep test for stars and microgels in the solid regime. This data come from a 1.1c (18 wt%) solution of the stars RS128PBD5 in squalene. The black symbols are the G' (filled) and G" (open) obtained with the Physica MCR 501. The blue symbols are the G' (filled) and G" (open) obtained with a homemade piezorheometer[19]. The red arrow points towards the value of G' at minimum G" that we call plateau modulus.*

Following the linear characterization of the samples, the flow curve was measured. For dilute samples of microgels and stars in the liquid regime, the standard mode of the MCR 501 were used to progressively increase the shear rate step-by-step and measure the corresponding steady state stress and viscosity. The shear rate was varied between $10^{-3}s^{-1}$ and $10^{3}s^{-1}$ although the low shear rates are rapidly limited by the accuracy of the torque detection (>0.1 μN.m). For more concentrated samples of microgels and stars in

the solid regime, start-up experiments were used to identify the transient regime of the stress-strain curves.

The start-up experiment consists in a sudden increase of the shear rate from 0 to the command value set between $5.10^{-4}s^{-1}$ and $50s^{-1}$. The response time of the instrument is about 50 to 100 ms (depending on the shear rate), after which the command value was reliably achieved. No significant overshoot of the shear rate was measured during this step. The steady shear was maintained until a total strain of 1500% was reached, after which the shear rate was instantly brought back to 0. The decrease of the shear rate is again dictated by the response time of the instrument and is comparable to the start-up time (50 to 100 ms). The shearing time is dictated by the shear rate and the total strain of 1500% at the end of the experiment. Thus, the shearing was maintained for $t_f = \frac{15}{\dot{\gamma}}$ with t_f the duration of the experiment and 3.10^{-1} s< t_f < 3.10^4 s. The steady state was characterized by a constant stress with time and was always achieved at the end of the experiment except for some particular cases at high concentrations of microgels during which part of the sample broke (fractured) and escaped from the gap (see chapter 4). The steady state value of stress was measured as the average stress between strain amplitude values of 1300 % and 1500%. The steady state viscosity was calculated as the measured stress divided by the command shear rate.

Directly after the start-up experiments, stress relaxation was performed. During this test, the command value of the shear rate is set to 0 and the stress was let to relax. We performed this experiment for at least the same time as the preceding start-up experiments, such that the relaxation was measured for at least t_f. In some particular cases of interest, the stress relaxation was measured for up to 1000 times t_f, which could realistically only be done after high-shear-rate experiments.

Occasionally, other types of rheological measurements, such as creep experiments, were performed, depending on the question to be addressed. The details of these tests will be described in details in each chapter when needed.

Creep-to-linear data conversion

Constant stress (creep) experiments were performed on some of the star solutions and melts. At low values of stress, the creep compliance J(t) can theoretically be used to calculate the linear viscoelastic spectrum G'(ω), G"(ω)[21–24]. We used the dedicated software "NLREG" to convert the creep data into linear data[25]. Although the technical details of the conversion will not be explained here, the software can solve nonlinear ill-posed inverse problems using Tikohnov regularization methods (for example for rheology or photon correlation spectroscopy). It is based on the equivalence of the frequency domain and the time domain through an integral equation. Since the entire time domain cannot be measured (given instrumental limitations), the conversion is an ill-posed problem, meaning that we cannot get enough experimental information to uniquely calculate the integral. The software uses a nonlinear regularization method to estimate the logarithm of the relaxation time spectrum from the creep data and calculates the equivalent oscillatory elastic and viscous moduli G'(ω) and G"(ω). In oscillatory measurements, the duration of the experiment is many times the inverse of the lowest frequency, because the instrument needs to perform several oscillations at this frequency to obtain good signal statistics. Using creep, the lowest measurable frequency is given by the inverse of the duration of the experiment. This allows for the extension of the linear viscoelastic spectrum towards the low frequency regime on experimentally accessible timescales (days).

In the case of the star solutions and melts that we used in this work, the conversion was proven efficient, but sensitive to noise in the original data. Moreover, creep results were difficult to reliably obtain for these systems due to the interaction with long-time residual stresses (see chapter 5).

Dynamic Light Scattering

Dynamic light scattering was performed with very dilute samples of stars, microgels and grafted particles and the auto-correlation of the time-dependent scattered intensity I(q,t) was calculated according to Equation 1[26] :

$$g_2(q,t) = \frac{<I(q,t)\, I(q,t+t_0)>}{<I(t)>^2} \qquad \text{(Equation 1)}$$

where q is the wave vector of the scattered light (Equation 2), t is the time, $g_2(q,t)$ is the intensity auto-correlation function, t_0 is the lag time and the <> operator denotes the average value.

$$q = \frac{4\pi n_0 \sin(\theta/2)}{\lambda} \quad \text{(Equation 2)}$$

where θ is the angle between the incident light and the scattered light (angle of observation), n_0 is the optical index of the suspending medium and λ is the wavelength of the incident light.

The field auto-correlation function is connected to the intensity auto-correlation function by the Siegert relation (Equation 3)[27]. The Siegert relation can only be applied when the electric field is Gaussian[26,27], which can be a limitation for example in the case of non-ergodic, solid samples. The field auto-correlation has the maximum value for short lag times t_0 because the position of the scattering particles is the same as at time t, and therefore the scattered intensity is the same. When particles have time to move because of Brownian motion or other external forces (gravity, shear …), the correlation between time t and $t+t_0$ is lost and the auto-correlation function takes its minimum value.

$$g_2(q,t) = 1 + g_1(q,t)^2 \quad \text{(Equation 3)}$$

where $g_2(q,t)$ is the intensity auto-correlation function and $g_1(q,t)$ is the field auto-correlation function.

In the simple case of dilute solutions of Brownian particles at rest, the decay of the auto-correlation function is well captured by a single-mode exponential decay (Figure 2-3), which characteristic time depends on the diffusion coefficient of a particle (Equation 4). This equation only holds for small particles ($qR \ll 1$) in theory, although in practice the deviation is usually negligible.

$$D_0 = \frac{1}{\tau q^2} \quad \text{(Equation 4)}$$

where D_0 is the self-diffusion coefficient of one particle in the dilute regime, τ is the characteristic time of the exponential decay of C(q,t) and q is the wave vector of the scattered light.

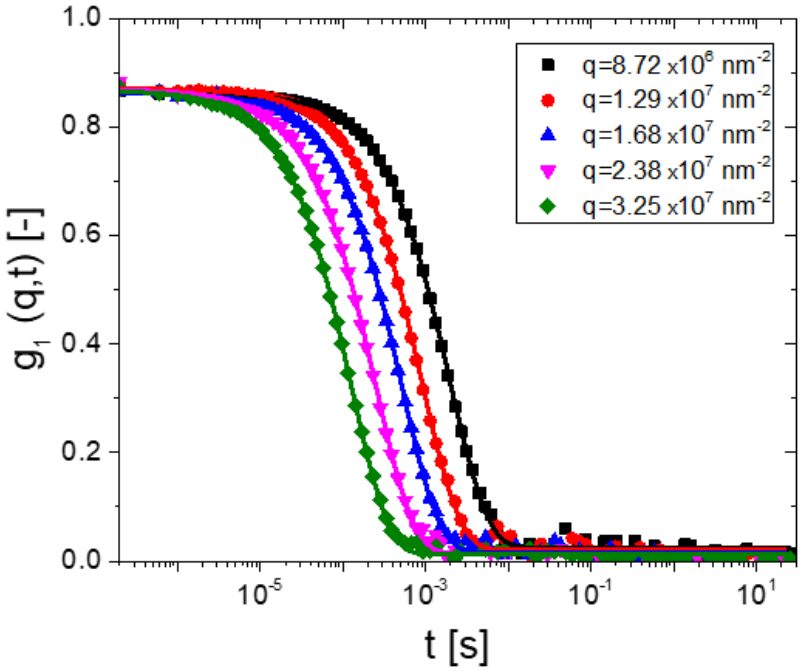

Figure 2-3. Field auto-correlation functions for the star RS128PBD5 in the dilute regime (c<<c) in cyclohexane. The data (symbols) were measured at five different angles between 30° and 150°. The lines through the data are the best fits using a single-mode exponential decay (no stretching).*

In the case of dilute spherical particles, the self-diffusion coefficient is directly connected to the hydrodynamic radius of the particle by the so-called Stokes-Einstein-Sutherland equation (Equation 5)[28]. The hydrodynamic radius calculated with this method is effectively the radius of the spherical particle (considered hard, non-porous) with the same diffusion coefficient.

$$D_0 = \frac{k_B T}{6\pi\eta R_h} \qquad \text{(Equation 5)}$$

Where k_B is the Boltzmann constant, T is the temperature, η is the solvent viscosity and R_h is the hydrodynamic radius.

This method gives an estimated of the effective hydrodynamic radius of the stars, microgels and grafted particles in the dilute regime. For the stars, which molecular weight is known, we can estimate the effective volume fraction corresponding to this hydrodynamic radius (Equation 6). This overlap concentration provides a way to rescale the concentration of different colloidal particles, based on their behavior in the dilute

regime, and will be used extensively in chapters 4 and 5. In practice, the overlap concentration corresponds to the concentration at which the average concentration of the macroscopic sample concentration and the average material concentration inside the particle become equal. By extension, it is usually considered as the critical concentration at which particles start to touch each other in the solution. For soft colloids, this concept is fundamentally incorrect, since their shape and volume depend on concentration, but it provides a simple way to estimate the volume fraction. A discussion on the validity of this approach is proposed in Appendix I.

$$c^* = \frac{M_n/N_A}{4/3\pi R_h^3} \qquad \text{(Equation 6)}$$

where c* is the overlap concentration, M_n is the number-average molar of the star and N_A is the Avogadro number.

Static Light Scattering

Static light scattering was used to characterize the size and the interactions of dilute solutions of grafted nanoparticles (see chapter 6). The average intensities of the light scattered by the samples were measured as a function of the wave vector and the concentration in particles. The scattered intensity, the wave vector and the concentration are connected by Equation 7[27]:

$$\frac{Kc}{I} = \frac{1}{M_w}\left[1 + \frac{q^2 R_g^2}{3} + O(q^4)\right] + 2A_2 c + O(c^2) \qquad \text{(Equation 7)}$$

where K is a numerical factor depending on the light and solution properties (Equation 8), M_w is the weight-average molar mass of the diffracting objects, q is the wave vector, R_g is the radius of gyration of the diffracting objects, and A_2 is the second coefficient of the virial expansion.

$$K = 4\frac{\pi^2 n_0^2}{N_A \lambda^4}\left(\frac{dn}{dc}\right)^2 \qquad \text{(Equation 8)}$$

where n_0 is the optical index of the solvent, N_A is the Avogadro number, λ is the wavelength of the incident light and dn/dc is the increment of the optical index with the concentration.

Therefore, the extrapolation of the intensity at q=0 and c=0 (Zimm plot[27]) yields an estimation of the radius of gyration and the second virial coefficient of the particles in their suspending medium. This property will be used in chapter 6 on polymer-grafted nanoparticles.

References

(1) Gauthier, M.; Munam, A. Synthesis of 1,4-Polybutadiene Dendrimer−Arborescent Polymer Hybrids. *Macromolecules* **2010**, *43* (8), 3672–3681. https://doi.org/10.1021/ma1004056.

(2) Roovers, J.; Zhou, L. L.; Toporowski, P. M.; van der Zwan, M.; Iatrou, H.; Hadjichristidis, N. Regular Star Polymers with 64 and 128 Arms. Models for Polymeric Micelles. *Macromol.* **1993**, *26* (16), 4324–4331. https://doi.org/10.1021/ma00068a039.

(3) Zhou, L. L.; Roovers, J. Synthesis of Novel Carbosilane Dendritic Macromolecules. *Macromolecules* **1993**, *26* (5), 963–968. https://doi.org/10.1021/ma00057a013.

(4) L. L. Zhou; N. Hadjichristidis; P. M. Toporowski; J. Roovers. Synthesis and Properties of Regular Star Polybutadienes with 32 Arms. *Ruuber Chem. Tech.* **1992**, *65* (2), 303.

(5) Jacques Roovers. Linear Viscoelastic Properties of Polybutadiene. A Comparison with Molecular Theories | Polymer Journal https://www.nature.com/articles/pj198620 (accessed Jan 24, 2019).

(6) Pellet, C.; Cloitre, M. The Glass and Jamming Transitions of Soft Polyelectrolyte Microgel Suspensions. *Soft Matter* **2016**, *12* (16), 3710–3720. https://doi.org/10.1039/C5SM03001C.

(7) Acciaro, R.; Gilányi, T.; Varga, I. Preparation of Monodisperse Poly(*N* -Isopropylacrylamide) Microgel Particles with Homogenous Cross-Link Density Distribution. *Langmuir* **2011**, *27* (12), 7917–7925. https://doi.org/10.1021/la2010387.

(8) *High Solid Dispersions*; Cloitre, M., Ed.; Advances in Polymer Science; Springer Berlin Heidelberg: Berlin, Heidelberg, 2010; Vol. 236.

(9) Cloitre, M.; Borrega, R.; Monti, F.; Leibler, L. Structure and Flow of Polyelectrolyte Microgels: From Suspensions to Glasses. *Comptes Rendus Physique* **2003**, *4* (2), 221–230. https://doi.org/10.1016/S1631-0705(03)00046-X.

(10) Romeo, G.; Imperiali, L.; Kim, J.-W.; Fernández-Nieves, A.; Weitz, D. A. Origin of De-Swelling and Dynamics of Dense Ionic Microgel Suspensions. *The Journal of Chemical Physics* **2012**, *136* (12), 124905. https://doi.org/10.1063/1.3697762.

(11) Borrega, R.; Cloitre, M.; Betremieux, I.; Ernst, B.; Leibler, L. Concentration Dependence of the Low-Shear Viscosity of Polyelectrolyte Micro-Networks: From Hard Spheres to Soft Microgels. *Europhysics Letters (EPL)* **1999**, *47* (6), 729–735. https://doi.org/10.1209/epl/i1999-00451-1.

(12) Cang, Y.; Reuss, A. N.; Lee, J.; Yan, J.; Zhang, J.; Alonso-Redondo, E.; Sainidou, R.; Rembert, P.; Matyjaszewski, K.; Bockstaller, M. R.; et al. Thermomechanical Properties and Glass Dynamics of Polymer-Tethered Colloidal Particles and Films.

Macromolecules **2017**, *50* (21), 8658–8669. https://doi.org/10.1021/acs.macromol.7b01752.
(13) Choi, J.; Hui, C. M.; Pietrasik, J.; Dong, H.; Matyjaszewski, K.; Bockstaller, M. R. Toughening Fragile Matter: Mechanical Properties of Particle Solids Assembled from Polymer-Grafted Hybrid Particles Synthesized by ATRP. *Soft Matter* **2012**, *8* (15), 4072. https://doi.org/10.1039/c2sm06915f.
(14) Hui, C. M.; Pietrasik, J.; Schmitt, M.; Mahoney, C.; Choi, J.; Bockstaller, M. R.; Matyjaszewski, K. *Surface-Initiated Polymerization as an Enabling Tool for Multifunctional (Nano-)Engineered Hybrid Materials*; Springer: Berlin ; New York, 2014; Vol. 26.
(15) Ohno, K.; Morinaga, T.; Koh, K.; Tsujii, Y.; Fukuda, T. Synthesis of Monodisperse Silica Particles Coated with Well-Defined, High-Density Polymer Brushes by Surface-Initiated Atom Transfer Radical Polymerization. *Macromolecules* **2005**, *38* (6), 2137–2142. https://doi.org/10.1021/ma048011q.
(16) Kapnistos, M.; Vlassopoulos, D.; Roovers, J.; Leal, L. G. Linear Rheology of Architecturally Complex Macromolecules: Comb Polymers with Linear Backbones. *Macromol.* **2005**, *38* (18), 7852–7862. https://doi.org/10.1021/ma050644x.
(17) van Gurp, M.; Palmen, J. Time-Temperature Superposition for Polymeric Blends. *Rheol. Bull.* 4.
(18) Moghimi, E.; Jacob, A. R.; Koumakis, N.; Petekidis, G. Colloidal Gels Tuned by Oscillatory Shear. *Soft Matter* **2017**, *13* (12), 2371–2383. https://doi.org/10.1039/C6SM02508K.
(19) Athanasiou, T.; Auernhammer, G. K.; Vlassopoulos, D.; Petekidis, G. A High-Frequency Piezoelectric Rheometer with Validation of the Loss Angle Measuring Loop: Application to Polymer Melts and Colloidal Glasses. *Rheologica Acta* **2019**, *58* (9), 619–637. https://doi.org/10.1007/s00397-019-01163-x.
(20) Helgeson, M. E.; Wagner, N. J.; Vlassopoulos, D. Viscoelasticity and Shear Melting of Colloidal Star Polymer Glasses. *J. Rheol.* **2007**, *51* (2), 297–316. https://doi.org/10.1122/1.2433935.
(21) Kim, M.; Bae, J.-E.; Kang, N.; Soo Cho, K. Extraction of Viscoelastic Functions from Creep Data with Ringing. *J. Rheol.* **2015**, *59* (1), 237–252. https://doi.org/10.1122/1.4904394.
(22) Kwon, M. K.; Lee, S. H.; Lee, S. G.; Cho, K. S. Direct Conversion of Creep Data to Dynamic Moduli. *J. Rheol.* **2016**, *60* (6), 1181–1197. https://doi.org/10.1122/1.4961484.
(23) Vyas, B. M.; Orpe, A. V.; Kaushal, M.; Joshi, Y. M. Passive Microrheology in the Effective Time Domain: Analyzing Time Dependent Colloidal Dispersions. *Soft Matter* **2016**, *12* (39), 8167–8176. https://doi.org/10.1039/C6SM00829A.
(24) Evans, R. M. L.; Tassieri, M.; Auhl, D.; Waigh, T. A. Direct Conversion of Rheological Compliance Measurements into Storage and Loss Moduli. *Phys. Rev. E* **2009**, *80* (1), 012501. https://doi.org/10.1103/PhysRevE.80.012501.
(25) Honerkamp, J.; Weese, J. A Nonlinear Regularization Method for the Calculation of Relaxation Spectra. *Rheologica Acta* **1993**, *32* (1), 65–73. https://doi.org/10.1007/BF00396678.
(26) Bruce J. Berne; Robert Pecora. *Dynamic Light Scattering*; New York University Press, 1976.

(27) *Light Scattering from Polymer Solutions and Nanoparticle Dispersions*; Springer Laboratory; Springer Berlin Heidelberg: Berlin, Heidelberg, 2007.
(28) Einstein, A. Elementare Theorie der Brownschen Bewegung. *Zeitschrift für Elektrotechnik und Elektrochemie* **1908**, *14* (17), 235–239. https://doi.org/10.1002/bbpc.19080141703.

Chapter 3 - Colloidal jamming in multiarm star polymer melts

Abstract

Star polymers with intermediate branching functionalities (64 and 128 arms) are known to exhibit a hybrid viscoelastic response, relaxing stress via a fast polymeric arm retraction and a slow colloidal mode. We show that, in the limit of very high functionalities (above 800) and very short arms (3 entanglements or less), the colloidal mode following arm relaxation exhibits a plateau with a modulus much smaller than expected from the entanglement value, and does not relax within the experimentally accessible frequency window. Analysis of the relaxation modes indicates that even in the melt state, stars with ultra-high branching functionalities effectively behave like jammed colloids. Their low modulus makes them easily processable, unlike highly entangled linear polymers. A simple state diagram in the melt is proposed with two control parameters, the functionality and the number of entanglements per arm (as a measure of arm size), showing three distinct regimes based on dynamics: polymeric, hybrid polymeric-colloidal and jammed. These results are briefly discussed in view of other highly branched polymers with density heterogeneities (microgels, bottlebrushes) exhibiting non-terminal solid-like response and supersoft elastomeric features. For the present stars in particular, which are model soft colloids, these findings contribute to the ongoing discussion on jamming in soft matter.

3.1 – Introduction

Linear or lightly branched polymer melts can mix topologically while maintaining a uniform monomer density throughout the macromolecules, resulting in linear viscoelastic spectra which are understood within the framework of a multi-scale relaxation process encompassing regimes from segmental to global dynamics[1]. On the other hand, densely branched macromolecules such as multiarm star polymers, which serve as archetype soft colloids[2], are characterized by an inhomogeneous intramolecular

monomer density, which is higher at the center where monomers belonging to different arms practically touch one another, and decays toward the periphery[3]. For solutions, Daoud and Cotton predicted three monomer density regimes[4]: the inner melt-like core regime, the intermediate theta-like (coat or unswollen) regime, where the blobs are ideal and only solvent can penetrate at high concentrations and, for good solvents, the outer excluded volume (or swollen) regime, where the blobs are swollen and star-star interpenetration can take place in dense solutions. The soft pair interactions between stars can be successfully described by a coarse-grained potential, exhibiting logarithmic repulsions at short distances and Yukawa-type repulsions at long distances[5]. In general, the branching functionality (number of arms, f) and arm length (molar mass Ma) of the arms are the control parameters governing their macroscopic properties at different concentrations[2]. When the solvent is removed in the melt state, the inherent mismatch in density is compensated by star interpenetration and shape adjustment.

Multiarm stars in the melt display hallmarks of both polymers and colloidal suspensions[1,6,7]. At high frequencies, the viscoelastic data reflect local dynamics and they collapse onto the linear viscoelastic spectrum of the corresponding linear polymers. At intermediate frequencies a rubbery plateau is detected for stars with entangled arms, which interpenetrate to reduce density heterogeneities. Of particular interest is the terminal relaxation at the low-frequency end of the plateau region, which is characterized by a two-step decay, in sharp contrast to the single terminal relaxation processes of low-functionality stars, linear homopolymers, or even colloidal hard spheres[8]. The faster relaxation is due to the star arm retraction and depends on the arm length but not on the branching functionality, whereas the slow mode is associated with structural rearrangements of the stars, which are essentially solvent-free soft colloids; it depends on both f and Ma[6,9]. The connection between slow relaxation and the existence of monomer density heterogeneities was demonstrated through SAXS measurements, which revealed the occurrence of weak ordering in stars[3,10,11]. This type of spatial organization, called liquid-like order, reflects excluded volume interactions at the macromolecular size scale.

Stars, which are virtually chemically uniform (the homopolymer arms are grafted to a very tiny core) exhibit similarities with but also clear differences from polymer-grafted

nanoparticles. Density heterogeneities in these systems come mainly from their internal structure comprising a large core with grafted arms and to a lesser degree from the arms. Their structure and dynamics depend primarily on the grafting density and the size of the grafted chains[12,13]. Due to their hybrid nature, these materials, which are called solvent-free colloids, exhibit a rich rheological behavior ranging from viscoelastic liquid (typically for low grafting densities and long chains[14]) to viscoelastic solids (at higher grafting densities and shorter chains[10,15]). Only in the limit of extremely small cores (approaching the monomeric scale of the grafted chain), grafted nanoparticles may be considered as stars[16].

Another example of particles which can be thought of as soft colloids in the melt state are microphase separated block copolymers[17,18]. The rheology of body-centered-cubic mesophase of various diblock and triblock copolymer melts (self-assembled into spherical micelles) bears analogies with that of colloidal crystals[19,20]. It should be noted however, that since these micelles form because of the enthalpic repulsion between the blocks, they are sensitive to temperature and are in this respect different.

In view of the above, an outstanding challenge is to understand how and to what extent the dynamics of multiarm star polymers in the melt state can be described using concepts borrowed from soft colloids. Pertinent emerging questions concern the nature of the slow mode, and whether star polymers exhibit features of glassy dynamics in the melt. In this work we present experimental data that complete the overall description of multiarm star polymer melts and answer these questions. Our results are particularly relevant to soft colloids, whose properties can be described by a conceptual framework based on two pillars, microgels and stars[2]. They will be useful in understanding the transition from solution to melt behavior and the possible jamming of soft colloids.

3.2 – Description of the linear viscoelasticity of star polymer melts with varying functionality

The linear viscoelastic responses of a linear polybutadiene with a molar mass 155 kg.mol^{-1} and a star with f = 128 and M_a = 6.8 kg.mol^{-1} (f: functionality; M_a: molar mass of the arms) are compared in Figure 3-1. All the master curves were obtained by applying

the time-temperature superposition principle (see also Appendix A3-1). The master curves are presented at the same distance from T_g, with a reference temperature $T_{ref}=T_g+73K$.

While the behavior of these two polymers is identical at high frequencies, there are noticeable differences at low frequencies. This is emphasized in the inset of Figure 3-1 which depicts the linear spectrum in the form of tan(δ). The rubbery plateau of the star is comparable to that of the linear polymer but it weakly decreases with decreasing frequency.

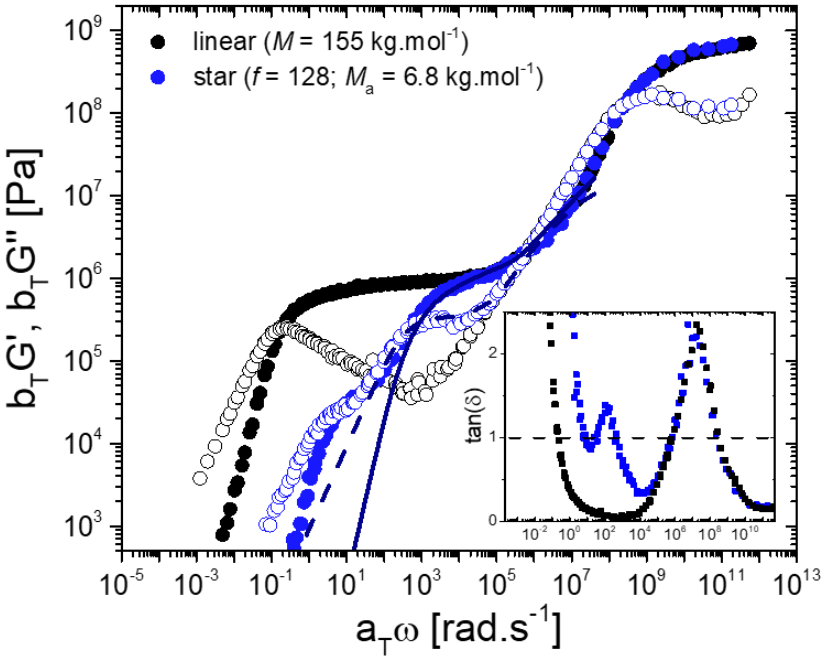

Figure 3-1. Linear viscoelastic spectra for linear and a 128-arm star polybutadiene polymer. The storage modulus G' is represented by filled symbols and the loss modulus G'' by open symbols. Inset: Respective data for tan(δ)=G''/G'. Lines represent the best fit of the data to the BoB model (see text and Appendix A3-3 for details).

Concomitantly, the arm relaxation (the faster of the two terminal modes) time of the star is much faster compared to that of the linear polymer[1,6,7,9,21]. A closer look at the low-frequency behavior reveals peculiarities of the star: the terminal regime is signaled by two distinct modes, as well evidenced by the tan(δ) plot in the inset of Figure 3-1, where three successive crossovers between G' and G" are observed, i.e. where tan(δ)=1. This is the rheological signature of the star particle microstructure[7,9]. The faster terminal

mode is of polymeric origin, and the slower one of colloidal origin. These two distinct modes are replaced by a broad shoulder for the 64-arm star indicating that the colloidal behavior depends strongly on functionality (See Appendix A3-2).

A comparison is provided in Figure 3-2a and 3-2b between the same linear polybutadiene and two star polymers with very high branching functionalities and low arm molar masses: f = 875 and Ma = 5.8 kg.mol-1, f = 929 arms and Ma = 4.0 kg.mol-1, respectively. These are called dense stars in the following. The master curves are presented at the same distance from T_g, with a reference temperature $T_{ref}=T_g+73K$.

While the behavior at high frequency again matches that of the linear polymer (corresponding to a tube diameter of about 4 nm), no terminal flow was reached for these two systems. Instead, both stars exhibit a low-frequency elastic plateau with a modulus approximately 10 times smaller than that of the entanglement plateau modulus of the linear polymer, suggesting larger-scale topological (cage-like) constraints. Both plateaus decrease weakly with decreasing frequency. This behavior is also reflected in the phase angle variations, depicted in the insets of Figures 2a and 2b, which take very low values at low frequencies. The fact that tan(δ) remains below unity at the local maxima indicates that there is no crossover between the elastic and viscous moduli in this frequency range. Thus, the material remains solid down to the lowest accessible frequencies.

Creep experiments at very low stress levels can provide information about the linear viscoelastic regime once properly converted[22–24]. As a consequence of their very slow relaxation these stars are able to keep internal stresses for long times. These internal stresses have a significant effect on the creep data, and therefore the creep conversion into linear data is difficult in this case, leading to ambiguities (see Chapter 5). Waiting for several days is the only reliable solution that was found in this case, yielding reliable and reproducible data from creep. A long-time creep experiment at a stress of 1 kPa was performed on one of the stars (f=929, M_a=4.0 kg.mol^{-1}) and the result was converted into linear data (see Chapter 2) and compared to the master curve obtained with TTS. The conversion of creep data agrees well with the conventional oscillatory data in the frequency range accessible for both experiments, although we observe a somewhat lower G" in this region. This technique allows to extend the frequency range significantly

towards the low frequencies and seem to provide an estimation of the possible crossover between G' and G" in this sample. This result is however subject to a lot of uncertainties, since it requires the reliable measurement of the material deformation (very small) for several days and a mathematical conversion of the (often scattered) data that has proven sensitive to noise in the original creep data. The obtained value for the crossover should therefore be taken as a rough estimation at best, which marks the lower bound for the crossover.

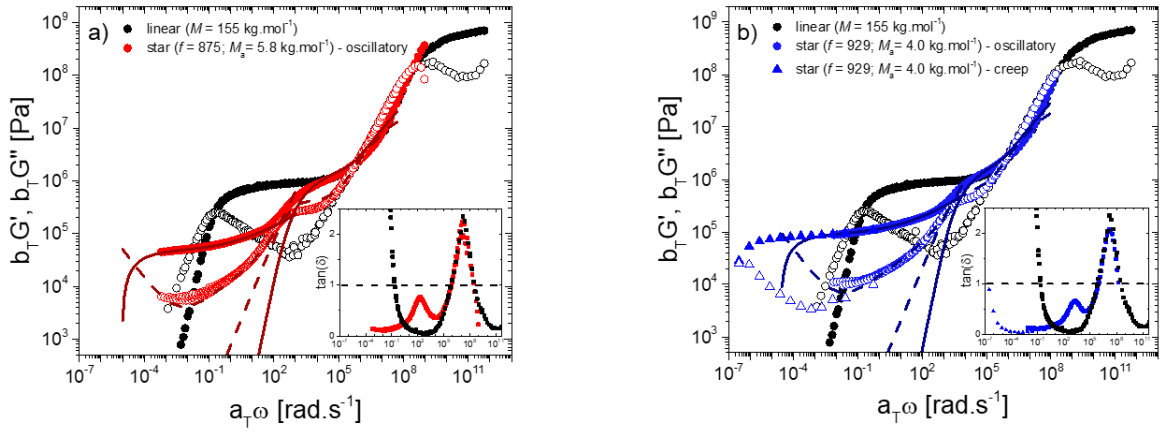

Figure 3-2. Linear viscoelastic spectra for linear polybutadiene and two polybutadiene stars with extreme functionalities and low arm molar masses: f = 875 and M_a = 5.8 kg.mol-1 (a); f = 929 and M_a = 4.0 kg.mol-1 (b). The green triangles represent the data converted from creep (see text). Inset: Respective tan(δ) data. Lines represent the best fit of the oscillatory data to the BoB model (high frequencies) and the MCT (low frequencies).

This observed behavior is a manifestation of the colloidal nature of these systems, which experience topological constraints on the scale of their own size. Even in the frequency range where the star arms have relaxed, the material does not flow but behaves like an elastic solid. Hence there is a transition from a polymeric regime where elasticity is dominated by entanglements and slow retraction of the arms, to a colloidal regime, where star polymers effectively act as elastic soft spheres. Their softness depends mainly on the branching functionality[2,5]. At extreme functionalities (f=900) they are less soft than at f=128 and they can be considered as approaching the hard sphere limit[25]. In such a case, particle-level excluded volume effects dramatically slow-down their center-of-mass motion resulting in caging, and the stars jam over the time scales corresponding to the experimental frequency window, like microgel particles, emulsions or foams[2,26,27].

This unexpected behavior arises from the extremely high branching functionality and the short arm length. In such a case, the stars are trapped in strong cages and to escape, they have to overcome a high energy barrier, hence they are effectively jammed. In this context, we expect that stars with higher branching functionality and shorter arms should exhibit a higher colloidal plateau modulus (compare the low frequency regions of Figures 3-2a and 3-2b), but further theoretical or numerical studies would be needed to fully unravel the microscopic behavior of such dense systems. In conclusion, from a colloidal perspective, when the branching functionality increases and the arm molar mass decreases, the cages around the particles evolve from fuzzy and soft to harder with sharper potential wells[5].

3.3 – Scaling of the multiple relaxation times in the viscoelastic spectrum of dense star polymer melts

To further support the above picture of a polymer-to-colloid transition in multiarm star polymers, the relaxation times of the first and second modes were compared to existing data from the literature for other star systems[7]. The branch-on-branch BoB model[28] was used to fit the rubbery plateau of the stars and provided an estimate of the polymeric relaxation time τ_p (taken as the inverse of the crossover frequency between G' and G"). Details are presented in the Appendix A3-3. This relaxation time τ_p is reported in Figure 3-3a along with data from the literature[6,9,29]. The solid line is the prediction for the polymeric relaxation time of star polymers using the tube model[1,30], which is given by:

$$\frac{\tau_p}{\tau_e} = AZ^{5/2}\exp[\nu Z] \qquad \text{(Equation 1)}$$

where τ_p and τ_e are the arm relaxation time and Rouse time of an entanglement segment[1], respectively, Z is the number of entanglements per arm (for which we consider the entanglement molar mass M_e of linear chains), ν is a numerical parameter with a value of 0.4, and A is a constant. With A=5, the experimental data and the prediction are in excellent agreement. This supports the polymeric origin of the relaxation time τ_p. However, some comments are in order. First, the two high-functionality stars presented here are very dense. Their core is estimated in the framework of the Daoud-Cotton model[4]:

$$R_c = b\sqrt{f} = 15\ nm \qquad \text{(Equation 2)}$$

where b=0.5 nm is the Kuhn length which is to be compared to the size of a star in the melt estimated from the density:

$$\tilde{R} = \sqrt{\frac{M_w}{\rho N_A}} = 20\ nm \qquad \text{(Equation 3)}$$

where M_w the weight-average molar mass, ρ the density and N_A the Avogadro number.

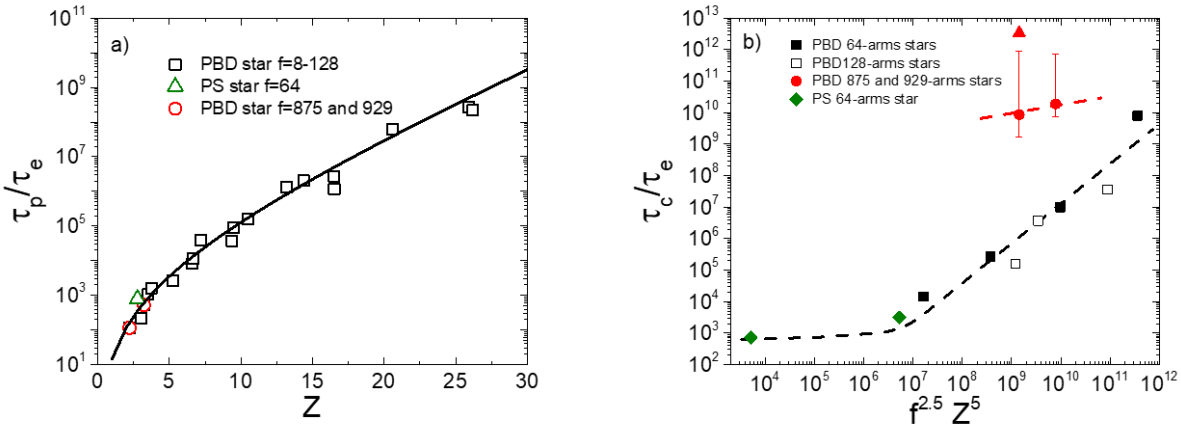

Figure 3-3. Relaxation time of (a) polymeric mode and (b) colloidal mode for different polybutadiene (black squares and red circles) and polystyrene (green diamonds) star polymers as a function of the number of entanglements per arm, Z, and a combination of functionality f and Z, respectively. The red circles represent the dense stars from Figure 2 and the black squares are from literature data[6,7,9]. Added in the plot is data points from polystyrene stars (green triangles) with 64 arms from recent literature[29] to confirm its generality. The red triangle represent the estimation of the crossover time for the high functionality star obtained thanks to the conversion of creep data (see text). The line in a) represents the prediction from the tube model (see text); the black dashed line is an empirical scaling from the literature (see text). The red dashed line in b) is drawn to guide the eye.

Hence, these stars are situated in the Daoud-Cotton core region or, alternatively in the frequently used terminology in grafted nanoparticles, in the concentrated polymer brush region[31]. Under this condition, the topological constraints of the star arms differ from the classic picture of entangled stars[1]. However, it is possible that the constraints imposed on an arm by its neighbors inside one star may have similar consequences as inter-star entanglements regarding viscoelasticity. There are two arguments here: first, even though the monomer density profile inside such a dense star should be steep[32], the outer

segments still attempt at interpenetrating in order to reduce the small density heterogeneities[6,33]. Second, computer simulations of dense spherical brushes suggest that dynamics of the arms is slowed-down due to the confinement they feel from their neighbors at high grafting densities[34,35]. In the present stars, the equivalent grafting density is very high (almost 2.9 nm^{-2} around the chemical core and 0.32nm^{-2} around the estimated Daoud-Cotton core). Therefore, the arms are severely constrained and their dynamics can be described by fitting the BoB model, mapping onto the dynamics of entangled stars even though entanglements may not exist, at least not in the classic sense of physical network formation by means of arm interpenetration[1]. Note that such mapping has been performed for similar reasons of topological constraints in other branched polymers as well[36]. Interestingly, the extracted times from the BoB fit comply with the generic representation of arm relaxation time in Figure 3-3a.

The low-frequency storage and loss moduli were further fitted to mode coupling theory (MCT) predictions using the same parameters as in the literature for hard and soft sphere glasses[37,38] in order to provide a phenomenological description of the jammed mode. Extrapolating the MCT lines to the cross-over frequency, it is possible to obtain a long relaxation time τ_c. This characteristic time is an estimate that provides an order of magnitude of the terminal colloidal relaxation time we should expect for such systems. The characteristic times τ_c are plotted on Figure 3-3b for the two dense stars of functionality 875 and 929, along with the terminal relaxation data from Refs. 6 and 9. We also plot the empirical scaling of the slow relaxation time with $f^{5/2}Z^5$ proposed in Ref. 7. This scaling proves effective for the two intermediate functionalities (f = 64 and 128). However it clearly does not hold for the extreme functionalities investigated here. Below, we propose some arguments to explain this difference.

3.4 – State diagram of star polymer melts

Careful examination of the different datasets available for a wide range of stars suggests that there are two parameters influencing the longest relaxation time in star polymers: the branching functionality (f) and the number of entanglements per arm (Z). Let us focus first on Z which seems to have a dual effect on the colloidal mode. It needs to be small enough to ensure that the stars have a relatively large equivalent core in order

to behave like colloidal particles where arm relaxation and center-of-mass motion are decoupled[9,39]. Increasing Z shifts the polymeric relaxation time τ_p to longer timescales and also increases the colloidal relaxation time τ_c, as shown in Figure 3-3b. Moreover f also needs to be large enough for stars to behave as colloids, pretty much for the same reasons. Increasing f significantly increases the colloidal relaxation time so that eventually, dense stars like the ones studied here become dynamically arrested. It is important to note that this arrest cannot be described by the classic scaling for stars of intermediate functionality[7,9], as shown in Figure 3-3b. Hence it represents a transition which exhibits the hallmarks of colloidal jamming in the melt. This phenomenology can be summarized in the qualitative dynamic diagram in Figure 3-4, which gives evidence for three regimes in the f-Z space based on viscoelastic relaxations: polymeric (arm relaxation), hybrid (arm relaxation followed by center-of-mass motion of the star and jammed (arm relaxation followed by long time colloidal trapping with no observable terminal flow). A conceptually similar diagram recently proposed for polystyrene stars with low functionalities up to 64[29], also shows a transition from polymer to hybrid (polymeric and colloidal) response.

In Figure 3-4, we reproduce some data points from that work to show the generality of the approach. We also extend our analysis to polymer-grafted nanoparticles and find that data from the literature of silica-g-PEO particles with very high grafting densities[15] fall into our jamming region. A very recent set of silica-g-PS particles with constant grafting densities and varying brush length[40] is also added and provides a remarkable insight into the transition between the three regimes. Indeed, our qualitative predictions almost accurately predicted the behavior observed for these particles.

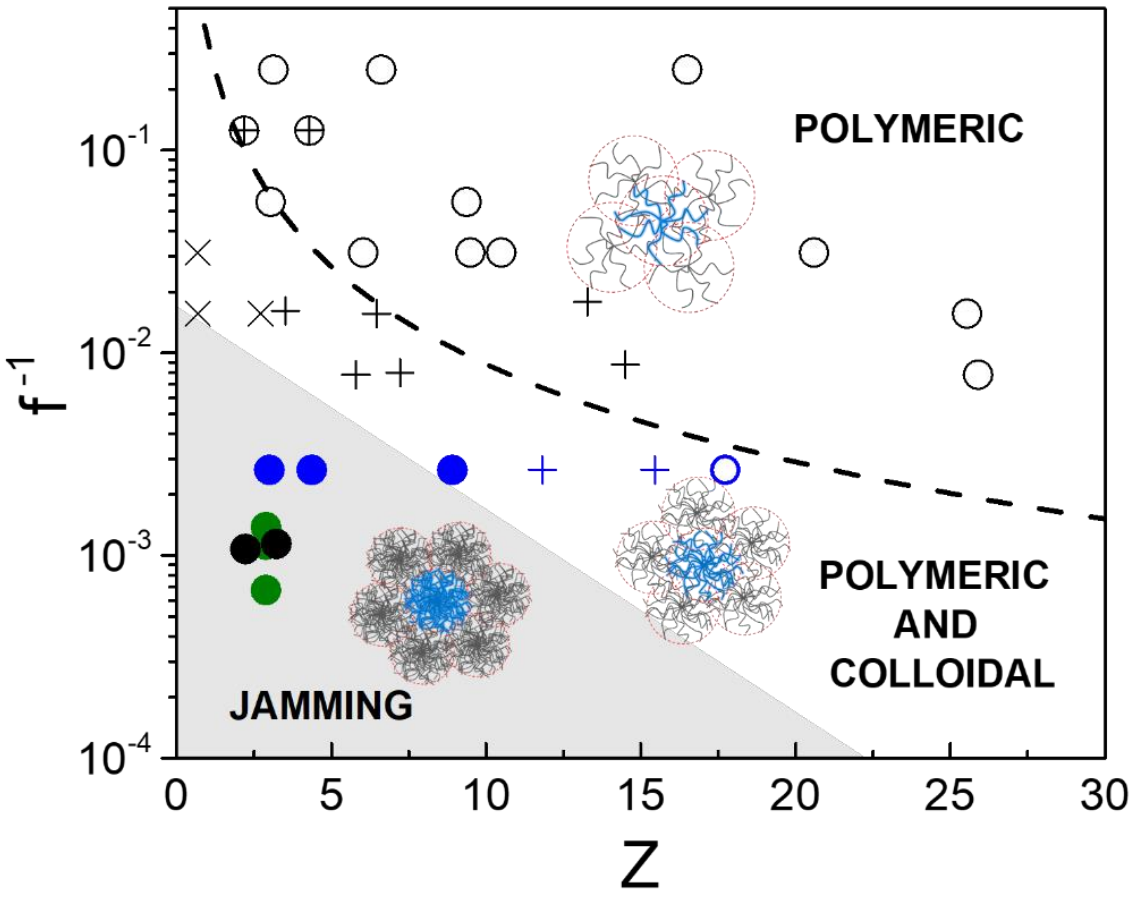

Figure 3-4. Dynamic state diagram for melts of star polymers in terms of viscoelastic behavior as function of the inverse functionality f^{-1} and the number of entanglement per arm Z. The circles are data points for polymeric behavior[6,7,9], the + crosses represent stars with a hybrid polymeric-colloidal response[6,7,9], and the full symbols represent dense stars where the slow colloidal mode is arrested (jamming). For generality, polystyrene stars from recent literature[29] are also represented as crossed circles for the polymeric behavior and x crosses for the hybrid behavior. In addition, polymer grafted nanoparticles are also represented as green (Si-PEO)[15] and blue (Si-PS)[40] symbols. The same nomenclature is used to differentiate the three regimes. The dashed line represents the empirical equation Z/f = 0.2 as a qualitative boundary between the two domains.

Different conclusions can be drawn from the above analysis. Firstly, the colloidal relaxation time is several orders of magnitude larger than the estimated polymeric relaxation time for the two dense stars. By any measure, this complies with dynamic arrest[41]. Secondly, it is clear that this relaxation time largely depends on functionality. Based on this, we propose that the present stars exhibit a form of soft colloidal jamming, here in the melt, similar to that observed in foams, emulsions and microgels at high volume fractions. Qualitatively similar behavior has been observed in melts of grafted nanoparticles. The amorphous solid material has features of a colloidal glass, i.e., an

extended plateau storage modulus exceeding in magnitude the weakly frequency-dependent loss modulus, and non-ergodicity, despite the fact that the core volume fraction is well below 0.58[10,15,42,43]. Interestingly, linear viscoelastic data with nanoparticles of 10 nm diameter, grafted with about 380 polyisoprene chains, which exhibit an extended plateau region followed by a slow terminal crossover[15] fit onto the jamming region of this diagram. The viscoelastic properties of these systems were shown to depend on grafting density and size of grafts and could also exhibit features of colloidal jamming[15]. Moreover, recent data with polystyrene-grafted silica nanoparticle melts having constant grafting density and varying molar mass of polystyrene, also comply with this picture[40]. Hence, the representation of Figure 3-4 should be generic. However, given that stars and grafted nanoparticles are different (in particular with respect to core size), we prefer to restrict our discussion to well-defined stars of the same chemistry, while pointing out the analogies with other systems. A more general description shall be presented in the future[40].

There is also an interesting analogy with microgel melts, the only other soft colloidal system which is chemically homogeneous. The limited available linear viscoelastic data on polystyrene microgels in the melt have been compared against those of entangled linear chains in three regimes: (i) at high frequencies, the data reflect local dynamics and are indistinguishable for different systems; (ii) the intermediate plateau region has an amplitude similar to that of the entanglement network and its extent in frequency depends on the degree of crosslinking; (iii) the terminal relaxation is slowed-down as compared to linear polymers, and for high degrees of crosslinking it is arrested in the accessible frequency range, which was proposed at the time as a proof for non-reptative polymer dynamics[44,45]. However, the (solvent-free) colloidal nature of such systems arising from excluded volume effects at the scale of the entire particle was not considered. The strong qualitative similarities with the present results suggest the possible occurrence of colloidal jamming in microgel melts as well.

Finally but importantly, the plateau modulus of the jammed colloidal mode is approximately ten times smaller than the entanglement plateau of the polymeric arms. This has important consequences on the processability and deformability of these systems, making them very useful in potential applications, similarly to supersoft

elastomeric bottlebrushes[46,47]. In particular, the polybutadiene polymers used in the current investigation could not be easily processed, since their high plateau modulus of about 1 MPa makes them prone to slip[48]. However, with a modulus of 100 kPa or less, their handling is much facilitated. Interestingly, the total molar masses of the two dense stars are about 5000 kg.mol^{-1} for f=875 and 4000 kg.mol^{-1} for f=929. Considering pure reptation, linear chains of the same molar mass are estimated to have polymeric relaxation times of the same order of magnitude as those reported in Figure 3-3 for the colloidal relaxation times, hence they can also be considered as jammed, simply due to the larger number of entanglements; however, their modulus is prohibitively large[49]. Thus, by changing the architecture from linear to star, it is possible to obtain materials with tunable properties from viscoelastic liquids to solids with a modulus making them amenable to processing.

3.5 - Conclusions

Star polymers with very high functionalities (above 800) and very short arms (3 entanglements or less) exhibit a unique linear viscoelastic spectrum in the melt: following arm relaxation, the slow colloidal mode exhibits a plateau with a modulus much below the entanglement value, and does not relax within the experimentally accessible frequency window. Based on analysis of the relaxation modes and comparison with stars having lower functionalities and longer arms, we conclude that these systems exhibit extrapolated normalized terminal times which are several decades slower, hence they are clearly different and behave like jammed colloids. The results from different star melts can be compiled in the form of a simple state diagram with two control parameters, the branching functionality and the number of entanglements per arm (as a measure of arm size); this diagram shows three distinct regimes based on dynamics: polymeric, hybrid polymeric-colloidal and jammed. The exact boundary between these domains is quantitatively undetermined and it is clear that additional experiments with wider range of branching functionality and arm length will help resolving the jamming domain. Stars and microgels are different from grafted particles which are composite systems. Yet, they all exhibit features of jamming in the melt. Finally, the low modulus of the colloidal star mode suggests that high-functionality stars can be easily processable, unlike highly entangled linear polymers. This provides a link to other highly branched polymers like

bottlebrushes, dendronized or wedge polymers exhibiting non-terminal solid-like response and supersoft elastomeric character.

Appendix 3.1 – Shift factors used for the master curves of linear and star polymer melts

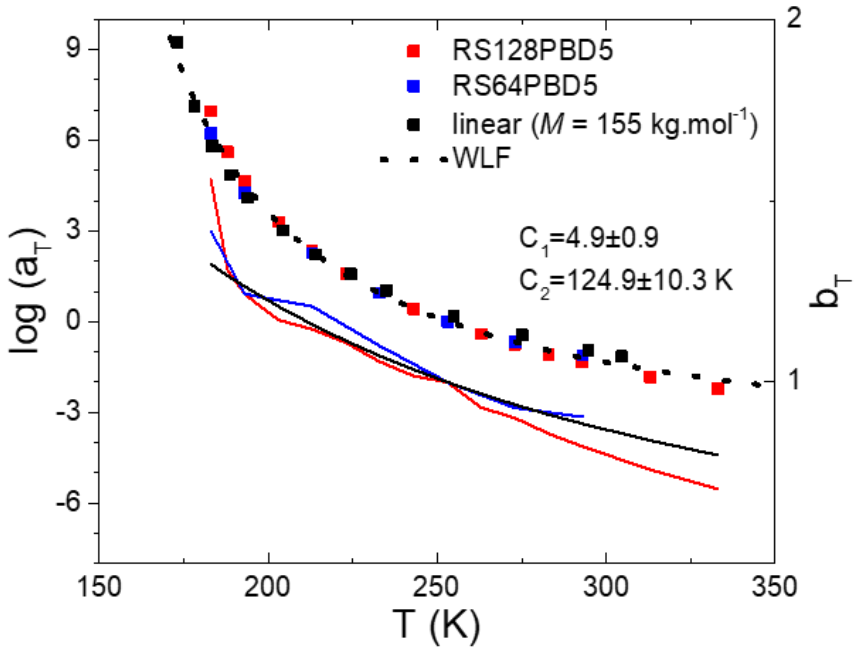

Figure A3-1a. Horizontal (a_T, triangular markers) and vertical (b_T, plain lines) shift factors used in the TTS master curves. The reference temperature used T_{ref} was such that T_{ref}-T_g=73K. The dashed line through the markers is an average fit following the Williams-Landel-Ferry (WLF) equation[50] (Equation 4). The average C_1 and C_2 values determined from the fits are reported on the figure.

$$\log(a_T) = \frac{C_1(T-T_{ref})}{C_2+T-T_{ref}} \qquad \text{(Equation 4)}$$

The three sets of shift factors superimpose well over the range of measured temperatures. However, in the case of the dense star with f=875 and M_a=5.8 kg.mol^{-1}, some clarification needs to be made regarding the high temperatures (273K and above). This corresponds to the colloidal plateau regime where the elastic modulus is much larger than the viscous modulus and almost independent of frequency. Therefore, the accurate

determination of the shift factor in this region is difficult, and indeed it is possible to see on the master curve that the overlap of G" for different temperatures is not perfect. This is a result of both the low values (and therefore inaccurate) of the phase angle in this region, as well as a possible breakdown of the time-temperature superposition method because of different mechanical processes, possibly dominated by particle contacts rather than constraints at the polymeric arm level. Nevertheless, within the accuracy of the experiments, the master curves are robust and the claim that one monomeric friction coefficient dictates the overall dynamics is reasonable (and consistent with the nearly unchanged T_g between samples). We also provide the sensitive van Gurp-Palmen plot (Figure A3-1b) leading to the same conclusions.

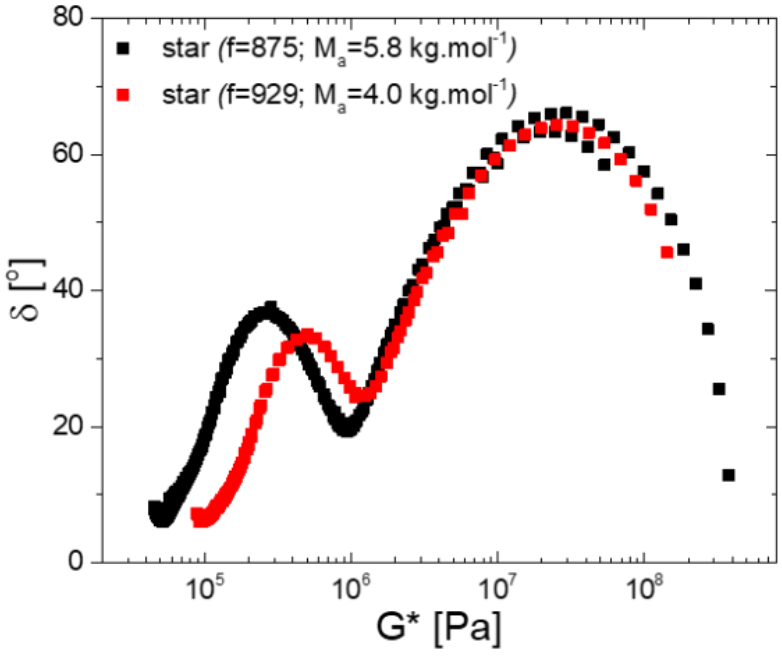

Figure A3-1b. Representation of the linear viscoelastic spectra of the two highest-functionality stars (Figure A3-1a of the main text) in the form of the van Gurp-Palmen plot of phase angle vs complex modulus.

Appendix A3.2 – Additional linear viscoelastic spectrum

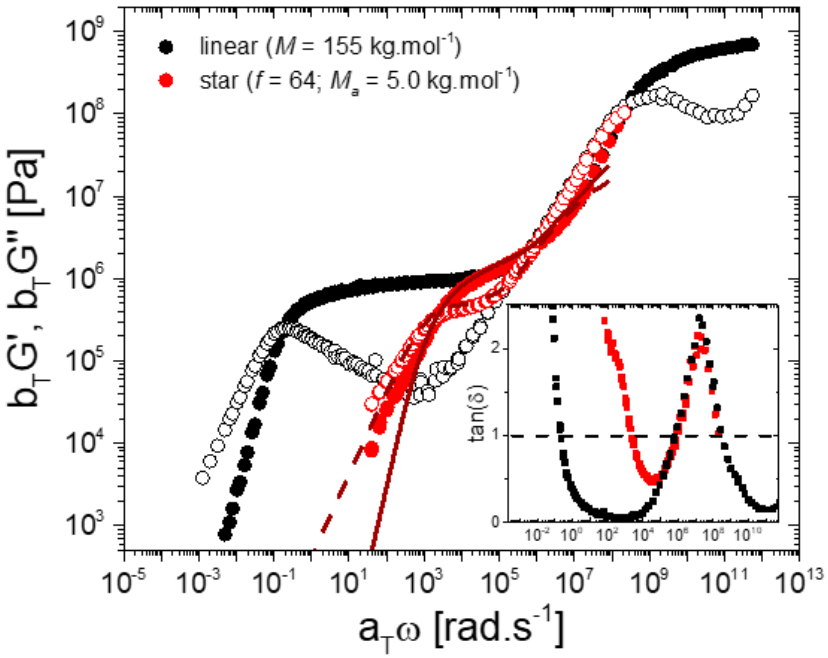

Figure A3-2. Linear viscoelastic spectrum of a polybutadiene star with f=64 arms and M_a=5 kg.mol^{-1} per arm (red), compared to the spectrum of linear polybutadiene with a weight-average molar mass of 155 kg.mol^{-1}. The lines through the data are the Bob-model[28] fits to G' and G" in the rubbery plateau regime. The tangent of the phase angle for the star and the linear polymer is provided in the inset.

Appendix A3.3 – Details from the MCT and BoB model fits to the star data

Polymeric fit (Branch on branch (Bob) model): Polybutadiene star polymers

M_0= 105 g.mol^{-1}

M_e= 1800 g.mol^{-1}

Plateau modulus= 10^6 Pa

Code	τ_e (s)	ω_e (rad.s^{-1})	τ_p (s)
6405	1.30 x10^{-6}	7.71 x10^{5}	3.58 x10^{-4}
12807	1.46 x10^{-6}	6.83 x10^{5}	1.12 x10^{-3}
RS64PBD5	1.14 x10^{-6}	8.74 x10^{5}	1.36 x10^{-4}
RS128PBD5	1.39 x10^{-6}	7.19 x10^{5}	7.21 x10^{-4}

Colloidal fit (Mode coupling theory, MCT):

The contribution from energy storage due to Brownian motion was neglected[51], as well as the dependence of the moduli on the volume fraction and size of the particles. For sample RS64PBD5, the applicability of the model is at the limit because the minimum in *G*" cannot be clearly identified within the frequency range investigated. The fit used the following expressions for *G*' and *G*".

$$G'(\omega) = G_p + G_\sigma \left[\Gamma(1-a')\cos\left(\frac{\pi a'}{2}\right)(\omega t_\beta)^{a'} - B\Gamma(1+b')\cos\left(\frac{\pi b'}{2}\right)(\omega t_\beta)^{-b'}\right]$$

$$G''(\omega) = G_\sigma \left[\Gamma(1-a')\sin\left(\frac{\pi a'}{2}\right)(\omega t_\beta)^{a'} - B\Gamma(1+b')\sin\left(\frac{\pi b'}{2}\right)(\omega t_\beta)^{-b'}\right] + \eta\omega$$

where G_p is the plateau modulus, G_σ is the viscoelastic amplitude, t_β is the β-relaxation time (taken as the inverse of the frequency at which *G*" is minimum) and η is the high-frequency suspension viscosity. These are the fitting parameters and are selected to best represent the data.

The variables *a*', *b*' and *B* are mode coupling parameters selected in agreement with literature[49] for colloidal hard spheres. The parameter values are given below:

a'=0.301

b'=0.545

B=0.963

Code	t_β (s)	G_σ (Pa)	G_p (Pa)	η (Pa.s)	τ_c (s)
RS128PBD5	343.76	3507	44907	536.23	2.67 x10^4
RS64PBD5	100	5953.5	87162.16	79.7	9.90 x10^3

References

(1) Michael Rubinstein, Ralph H Colby. *Polymer Physics*; Oxford University Press: Oxford, 2003.

(2) Vlassopoulos, D.; Cloitre, M. Tunable Rheology of Dense Soft Deformable Colloids. *Curr. Opi. Colloid Int. Sci.* **2014**, *19* (6), 561–574. https://doi.org/10.1016/j.cocis.2014.09.007.

(3) Pakula, T.; Geyler, S.; Edling, T.; Boese, D. Relaxation and Viscoelastic Properties of Complex Polymer Systems. *Rheola Acta* **1996**, *35* (6), 631–644. https://doi.org/10.1007/BF00396512.

(4) Daoud, M.; Cotton, J. P. Star Shaped Polymers : A Model for the Conformation and Its Concentration Dependence. *Journal de Physique* **1982**, *43* (3), 531–538. https://doi.org/10.1051/jphys:01982004303053100.

(5) Likos, C. N.; Löwen, H.; Watzlawek, M.; Abbas, B.; Jucknischke, O.; Allgaier, J.; Richter, D. Star Polymers Viewed as Ultrasoft Colloidal Particles. *Phys. Rev. Lett.* **1998**, *80* (20), 4450.

(6) Pakula, T.; Vlassopoulos, D.; Fytas, G.; Roovers, J. Structure and Dynamics of Melts of Multiarm Polymer Stars. *Macromol.* **1998**, *31* (25), 8931–8940. https://doi.org/10.1021/ma981043r.
(7) Vlassopoulos, D.; Fytas, G.; Pakula, T.; Roovers, J. Multiarm Star Polymers Dynamics. *Journal of Physics: Condensed Matter* **2001**, *13* (41), R855.
(8) Mewis, J.; Wagner, N. J. *Colloidal Suspension Rheology*; Cambridge series in chemical engineering; Cambridge University Press: Cambridge ; New York, 2012.
(9) Kapnistos, M.; Semenov, A. N.; Vlassopoulos, D.; Roovers, J. Viscoelastic Response of Hyperstar Polymers in the Linear Regime. *J. Chem. Phys.* **1999**, *111* (4), 1753–1759. https://doi.org/10.1063/1.479436.
(10) Agarwal, P.; Srivastava, S.; Archer, L. A. Thermal Jamming of a Colloidal Glass. *Phys. Rev. Lett.* **2011**, *107* (26). https://doi.org/10.1103/PhysRevLett.107.268302.
(11) Snijkers, F.; Cho, H. Y.; Nese, A.; Matyjaszewski, K.; Pyckhout-Hintzen, W.; Vlassopoulos, D. Effects of Core Microstructure on Structure and Dynamics of Star Polymer Melts: From Polymeric to Colloidal Response. *Macromol.* **2014**, *47* (15), 5347–5356. https://doi.org/10.1021/ma5008336.
(12) Hore, M. J. A. Polymers on Nanoparticles: Structure & Dynamics. *Soft Matter* **2019**, *15* (6), 1120–1134. https://doi.org/10.1039/C8SM02110D.
(13) R. Advincula; M.R. Buchmeiser; D. J. Dyer; T. Fukuda; A. Goto; T. Matsuda; K. Ohno; Y. Tsujii; S. Yamamoto. *Surface-Initiated Polymerization. I & II*; Rainer Jordan, Ed.; Advances in polymer science; Springer: Berlin ; New York, 2006.
(14) Sugimoto, M.; Ishizuka, K.; Hatano, K.; Sukumaran, S. K.; Aoki, Y. Viscoelastic Behavior of PMMA/Grafted PBA Nanoparticle Systems in the Molten State. *Rheol. Acta* **2017**, *56* (10), 779–785. https://doi.org/10.1007/s00397-017-1037-9.
(15) Kim, S. A.; Mangal, R.; Archer, L. A. Relaxation Dynamics of Nanoparticle-Tethered Polymer Chains. *Macromol.* **2015**, *48* (17), 6280–6293. https://doi.org/10.1021/acs.macromol.5b00791.
(16) Chremos, A.; Panagiotopoulos, A. Z. Structural Transitions of Solvent-Free Oligomer-Grafted Nanoparticles. *Phys. Rev. Lett.* **2011**, *107* (10), 105503. https://doi.org/10.1103/PhysRevLett.107.105503.
(17) Halperin, A. Polymeric Micelles: A Star Model. *Macromolecules* **1987**, *20* (11), 2943–2946. https://doi.org/10.1021/ma00177a051.
(18) Ruzette, A.-V.; Leibler, L. Block Copolymers in Tomorrow's Plastics. *Nat. Mater* **2005**, *4* (1), 19–31. https://doi.org/10.1038/nmat1295.
(19) Sebastian, J. M.; Lai, C.; Graessley, W. W.; Register, R. A. Steady-Shear Rheology of Block Copolymer Melts and Concentrated Solutions: Disordering Stress in Body-Centered-Cubic Systems. *Macromol.* **2002**, *35* (7), 2707–2713. https://doi.org/10.1021/ma011523+.
(20) Kossuth, M. B.; Morse, D. C.; Bates, F. S. Viscoelastic Behavior of Cubic Phases in Block Copolymer Melts. *J. Rheol.* **1998**, *43* (1), 167–196. https://doi.org/10.1122/1.550981.
(21) Fetters, L. J.; Kiss, A. D.; Pearson, D. S.; Quack, G. F.; Vitus, F. J. Rheological Behavior of Star-Shaped Polymers. *Macromol.* **1993**, *26* (4), 647–654. https://doi.org/10.1021/ma00056a015.
(22) Kwon, M. K.; Lee, S. H.; Lee, S. G.; Cho, K. S. Direct Conversion of Creep Data to Dynamic Moduli. *J. Rheol.* **2016**, *60* (6), 1181–1197. https://doi.org/10.1122/1.4961484.

(23) Evans, R. M. L.; Tassieri, M.; Auhl, D.; Waigh, T. A. Direct Conversion of Rheological Compliance Measurements into Storage and Loss Moduli. *Phys. Rev. E* **2009**, *80* (1), 012501. https://doi.org/10.1103/PhysRevE.80.012501.
(24) Vyas, B. M.; Orpe, A. V.; Kaushal, M.; Joshi, Y. M. Passive Microrheology in the Effective Time Domain: Analyzing Time Dependent Colloidal Dispersions. *Soft Matter* **2016**, *12* (39), 8167–8176. https://doi.org/10.1039/C6SM00829A.
(25) Truzzolillo, D.; Marzi, D.; Marakis, J.; Capone, B.; Camargo, M.; Munam, A.; Moingeon, F.; Gauthier, M.; Likos, C. N.; Vlassopoulos, D. Glassy States in Asymmetric Mixtures of Soft and Hard Colloids. *Physical Review Letters* **2013**, *111* (20). https://doi.org/10.1103/PhysRevLett.111.208301.
(26) Cohen-Addad, S.; Höhler, R. Rheology of Foams and Highly Concentrated Emulsions. *Curr. Opi. Colloid Int. Sci.* **2014**, *19* (6), 536–548. https://doi.org/10.1016/j.cocis.2014.11.003.
(27) Cohen-Addad, S.; Höhler, R.; Pitois, O. Flow in Foams and Flowing Foams. *Annual Review of Fluid Mechanics* **2013**, *45* (1), 241–267. https://doi.org/10.1146/annurev-fluid-011212-140634.
(28) Das, C.; Inkson, N. J.; Read, D. J.; Kelmanson, M. A.; McLeish, T. C. B. Computational Linear Rheology of General Branch-on-Branch Polymers. *J. Rheol.* **2006**, *50* (2), 207–234. https://doi.org/10.1122/1.2167487.
(29) Johnson, K. J.; Glynos, E.; Sakellariou, G.; Green, P. Dynamics of Star-Shaped Polystyrene Molecules: From Arm Retraction to Cooperativity. *Macromol.* **2016**, *49* (15), 5669–5676. https://doi.org/10.1021/acs.macromol.6b00456.
(30) Doi, M.; Kuzuu, N. Y. Rheology of Star Polymers in Concentrated Solutions and Melts. *J. Polym. Sci.: Polym. Lett. Ed.* **1980**, *18* (12), 775–780. https://doi.org/10.1002/pol.1980.130181205.
(31) Ohno, K.; Morinaga, T.; Takeno, S.; Tsujii, Y.; Fukuda, T. Suspensions of Silica Particles Grafted with Concentrated Polymer Brush: Effects of Graft Chain Length on Brush Layer Thickness and Colloidal Crystallization. *Macromolecules* **2007**, *40* (25), 9143–9150. https://doi.org/10.1021/ma071770z.
(32) Wijmans, C. M.; Zhulina, E. B. Polymer Brushes at Curved Surfaces. *Macromol.* **1993**, *26* (26), 7214–7224. https://doi.org/10.1021/ma00078a016.
(33) Lo Verso, F.; Yelash, L.; Binder, K. Dynamics of Macromolecules Grafted in Spherical Brushes under Good Solvent Conditions. *Macromol.* **2013**, *46* (11), 4716–4722. https://doi.org/10.1021/ma400446r.
(34) Reith, D.; Milchev, A.; Virnau, P.; Binder, K. Computer Simulation Studies of Chain Dynamics in Polymer Brushes. *Macromol.* **2012**, *45* (10), 4381–4393. https://doi.org/10.1021/ma202745b.
(35) Kirkwood, K. M.; Leal, L. G.; Vlassopoulos, D.; Driva, P.; Hadjichristidis, N. Stress Relaxation of Comb Polymers with Short Branches. *Macromol.* **2009**, *42* (24), 9592–9608. https://doi.org/10.1021/ma900950s.
(36) Helgeson, M. E.; Wagner, N. J.; Vlassopoulos, D. Viscoelasticity and Shear Melting of Colloidal Star Polymer Glasses. *J. Rheol.* **2007**, *51* (2), 297–316. https://doi.org/10.1122/1.2433935.
(37) Mason, T. G.; Weitz, D. A. Linear Viscoelasticity of Colloidal Hard Sphere Suspensions near the Glass Transition. *Phys. Rev. Lett.* **1995**, *75* (14), 2770.
(38) Grest, G. S.; Fetters, L. J.; Huang, J. S.; Richter, D. Star Polymers: Experiment, Theory, and Simulation. In *Advances in Chemical Physics*; Prigogine, I., Rice, S. A.,

Eds.; John Wiley & Sons, Inc.: Hoboken, NJ, USA, 2007; pp 67–163. https://doi.org/10.1002/9780470141533.ch2.
(39) Mattsson, J.; Wyss, H. M.; Fernandez-Nieves, A.; Miyazaki, K.; Hu, Z.; Reichman, D. R.; Weitz, D. A. Soft Colloids Make Strong Glasses. *Nature* **2009**, *462* (7269), 83–86. https://doi.org/10.1038/nature08457.
(40) Daniele Parisi; E. Buening; Leo Gury; B. C. Benicewicz; Michel Cloitre; Sanat K. Kumar; Dimitris Vlassopoulos. (Unpublished).
(41) Chremos, A.; Panagiotopoulos, A. Z.; Koch, D. L. Dynamics of Solvent-Free Grafted Nanoparticles. *J. Chem. Phys.* **2012**, *136* (4), 044902. https://doi.org/10.1063/1.3679442.
(42) Chremos, A.; Douglas, J. F. Particle Localization and Hyperuniformity of Polymer-Grafted Nanoparticle Materials. *Annalen der Physik* **2017**, *529* (5), 1600342. https://doi.org/10.1002/andp.201600342.
(43) Antonietti, M.; Pakula, T.; Bremser, W. Rheology of Small Spherical Polystyrene Microgels: A Direct Proof for a New Transport Mechanism in Bulk Polymers besides Reptation. *Macromol.* **1995**, *28* (12), 4227–4233. https://doi.org/10.1021/ma00116a025.
(44) Lindenblatt, G.; Schärtl, W.; Pakula, T.; Schmidt, M. Synthesis of Polystyrene-Grafted Polyorganosiloxane Microgels and Their Compatibility with Linear Polystyrene Chains. *Macromol.* **2000**, *33* (25), 9340–9347. https://doi.org/10.1021/ma001328f.
(45) Daniel, W. F. M.; Burdyńska, J.; Vatankhah-Varnoosfaderani, M.; Matyjaszewski, K.; Paturej, J.; Rubinstein, M.; Dobrynin, A. V.; Sheiko, S. S. Solvent-Free, Supersoft and Superelastic Bottlebrush Melts and Networks. *Nat. Mater* **2016**, *15* (2), 183–189. https://doi.org/10.1038/nmat4508.
(46) Rathgeber, S.; Pakula, T.; Wilk, A.; Matyjaszewski, K.; Lee, H.; Beers, K. L. Bottle-Brush Macromolecules in Solution: Comparison between Results Obtained from Scattering Experiments and Computer Simulations. *Polymer* **2006**, *47* (20), 7318–7327. https://doi.org/10.1016/j.polymer.2006.06.010.
(47) Lim, F. J.; Schowalter, W. R. Wall Slip of Narrow Molecular Weight Distribution Polybutadienes. *J. Rheol.* **1989**, *33* (8), 1359–1382. https://doi.org/10.1122/1.550073.
(48) Andablo-Reyes, E. A.; Auhl, D.; de Boer, E. L.; Romano, D.; Rastogi, S. A Study on the Stability of the Stress Response of Nonequilibrium Ultrahigh Molecular Weight Polyethylene Melts during Oscillatory Shear Flow. *J. Rheol.* **2017**, *61* (3), 503–513. https://doi.org/10.1122/1.4979334.
(49) Götze, W.; Sjögren, L. Comments on the Mode Coupling Theory for Structural Relaxation. *Chemical Physics* **1996**, *212* (1), 47–59. https://doi.org/10.1016/S0301-0104(96)00094-8.
(50) Williams, M. L.; Landel, R. F.; Ferry, J. D. The Temperature Dependence of Relaxation Mechanisms in Amorphous Polymers and Other Glass-Forming Liquids. *Journal of the American Chemical Society* **1955**, *77* (14), 3701–3707. https://doi.org/10.1021/ja01619a008.
(51) Mason, T. G.; Weitz, D. A. Optical Measurements of Frequency-Dependent Linear Viscoelastic Moduli of Complex Fluids. *Phys. Rev. Lett.* **1995**, *74* (7), 1250–1253. https://doi.org/10.1103/PhysRevLett.74.1250.

Chapter 4 - Jamming transition in the solid regime of hairy colloids

Abstract

Colloidal star polymers are comprised of a large number of polymeric arms covalently bound to a common central core, which very small. They can be viewed as a limit case of grafted nanoparticles with very small core size compared to the typical size of the whole particle. Since they are mainly composed of polymeric arms, their dynamics should be somewhat similar to polymers, but with severe constraints on the localization of the chain end attached to the core. Here we investigate a type of star polymers with very high branching functionality (875 arms) and small arm length (3 entanglements) that display both polymeric and colloidal rheological characteristics. The melt linear viscoelastic spectrum reveals an unexpected second elastic plateau at low frequencies, which is attributed to the jamming of the centers of mass of the star particles. Upon dilution, this plateau remains until a completely liquid sample is obtained. The evolution of the value of the elastic plateau with the concentration, in addition to other linear and non-linear rheological properties divide the concentration range into 3 distinct regimes: the viscoelastic liquid, the colloidal glass and the jammed or space-filling regime in which we expect the volume fraction to be very close to 1. The comparison of the stars to previous results on polyelectrolyte microgels provides a way to distinguish between the polymeric and colloidal features and their evolution with concentration.

4.1 – Introduction

Suspensions of soft colloids at high concentration can form amorphous solid states called colloidal glasses[1–4]. Although this has been known for a long time, there is still a lot to understand regarding the nature of this phase transition and the structural changes in the organization of the particles when they enter the solid regime. For hard spheres, the transition is now fairly well captured by theoretical models such as the phenomenological

mode coupling theory (MCT)[5] or its verses[6–8], although its validity deep in the glass regime is still questionable. Over the past few years, substantial progress has been made in the systematic description and characterization of soft colloids and in particular microgels[9], thanks to the progress of computer simulations[10,11] and experimental techniques such as microscopy[12]. It is now established that spherical soft particles at high concentrations form facets when squeezed, going from a regime dominated by free volume interactions (thermal glass) to a regime where contacts are the main origin of the material elasticity (jammed glass). In good solvent, most soft particles including star polymers and microgels can swell because of the osmotic pressure difference between the inside and the outside of the particle[13]. This effect can lead to a swelling ratio of the order of 1000 in volume, depending on the equilibrium between chain stretching and osmotic pressure. Deswelling can therefore occur at larger concentrations due to the decrease of the osmotic pressure difference and the displacement of this equilibrium[13]. This is a second way to decrease the volume occupied by each particle and therefore allow a higher number concentration. Star polymers and some microgels also possess long dangling ends that are able to interdigitate at high concentrations when the particles are in contact[14], therefore effectively reducing the total volume occupied by the particles by sharing the same volume between two or more particles. This type of overlap is only possible if the particles can somehow interpenetrate, and would therefore be absent in the case of soft elastic spheres, as is the case for emulsions and some microgel particles. Because of these three possible changes of the effective volume of the particles, the determination of the volume fraction of soft colloids remains a challenge.

The solid phase formed by concentrated soft colloids can be described as a generic yield stress fluid, which behaves as a solid at rest but is able to flow under stress. As such, it becomes possible to measure the behavior of these materials under flow as if they were liquids. The transition between the solid state to the liquid state is often called yielding, and has been studied at length in numerous experimental systems and computer simulations[15]. The information given by the non-linear response and the transient regime of soft colloids is often complex and subject to interpretation, but may contain clues that are not accessible with linear experiments, that only probe the resting (quasi-equilibrated) material.

In this chapter we describe the linear and non-linear rheological response of two model systems in the field of soft colloids, star polymers and microgels. The aim of this work is to gain further insight on the microstructure-dynamics relation of these soft colloidal suspensions at rest and under flow, especially in the highly concentrated regime of microgels and up to the melt state for stars. For microgels, computer simulations and experiments have already provided a good understanding of the systems at low and intermediate concentrations, and revealed a possible transition inside the glass regime that was called jamming[13,16]. We continue the experimental work by exploring the higher concentrations to confirm the existence of this transition and explicitly obtain and analyze the rheological signatures of the jammed regime. The star polymers we use here are unique in that they have an extremely high number of arms (branching functionality f=875) which are very short (molar mass of each arm M_a=5.8kg.mol^{-1}), and thus we expect that they are considerably harder than other stars from the literature[17,18]. Typically, star polymers are considered as much softer than microgels[17], but the use of such dense stars should bridge the gap between the two. Hence, we expect a similar rheological behavior and ask the question of the existence of a similar jamming transition in the glass regime of star polymers.

More than 35 years ago, Daoud and Cotton provided the eponymous classic model for the conformation of star polymers[19]. This model divides a star polymer in good solvent into three distinct parts based on scaling laws, with a dense core at the center, then a melt-like region and finally a Gaussian or swollen layer at the periphery. Each region has a specific size that depends only on the branching functionality and the size of the arms. In particular, the size of the core region varies like the square root of the branching functionality. In most cases from the literature[20,21], where the branching functionality rarely gets larger than 150, this region remains rather small compared to the particle size, but in our case of extreme functionality and small arms, it may represent a large portion of the total size: $R_c \approx b\sqrt{f} \approx 15\ nm$ compared to the swollen hydrodynamic radius of 23 nm (see Chapter 2). Since the model of Daoud and Cotton is based solely on scaling laws in the dilute regime, it is dangerous to explicitly derive an exact size for the core, but it is fair to say that it may represent a significant fraction of our stars, thus implying much harder interactions between particles than what has been previously studied. This makes

our star system a good candidate to investigate the jamming transition observed in the theoretically harder microgels[17].

In a first part, we present the linear viscoelastic behavior of star polymers. We show that the evolution of the elastic plateau modulus resembles a lot the one of microgels, and identify a possible transition inside of the solid regime, that we called jammed glass. In a second part, we explore in details the non-linear rheology of star polymers and show that the same transition concentration is again found at the peak of the critical shear rate marking the onset of flow in flow curves. In addition, the yield strain of the solutions is showed to increase with the concentration up to the same critical concentration again, after which it caps at about 10%. Fin a third part, we will show that the transient regime of start-up flow experiments also display an interesting evolution as the concentration is increased, with the appearance of second overshoot. Since this is not observed in microgels, we argue that this can be an effect of the interdigitation of the dangling chains in stars, which are virtually absent in microgels. Finally in a fourth part, we will describe a way to rescale the concentration, as the distance from the jamming point, which hints at a possible universality of jamming not only in dense stars and microgels, but across multiple different soft systems.

4.2 - Linear viscoelastic behavior of star solutions and melts

The frequency-dependent elastic (storage) and viscous (loss) moduli (G' and G", respectively) are presented in figure 4-1 for six concentrations representative of the different states of the material. For purposes of comparison with other systems, the concentration is normalized by the overlap concentration c*. Physically, c* describes the concentration beyond which the hydrodynamic volumes of the particles start to overlap. The overlap concentration c* provides a useful albeit questionable way of determining volume fraction to compare particles of different size, chemistry and architecture (see Appendix I).

At the lower concentrations (0.88c* and below), the material exhibits a viscoelastic liquid behavior with very low elasticity. The slopes 1 and 2 for the viscous and

elastic moduli, respectively, are typical for materials in the terminal flow regime. The extrapolation of these slopes to higher frequencies marks a crossover of G' and G" around 1000 rad.s^{-1}, which suggests that the material behaves as a liquid on timescales longer than 1 ms, in agreement with the macroscopic liquid behavior observed. The transition from a liquid to a solid behavior occurs between 1c* and 1.1c*, as shown by the progressive shifting of the crossover between G' and G" to the lower frequencies and the apparition of a prolonged plateau for G'. At 1.1c* the high-frequency crossover could not be detected, however from the examination of the entire dataset it seems that the elastic plateau of G' spans over about 3 decades of frequency which gives considerable elasticity to the material. The persistence of the terminal regime at low frequencies indicates that this material is however able to slowly flow at timescales on the order of 1s.

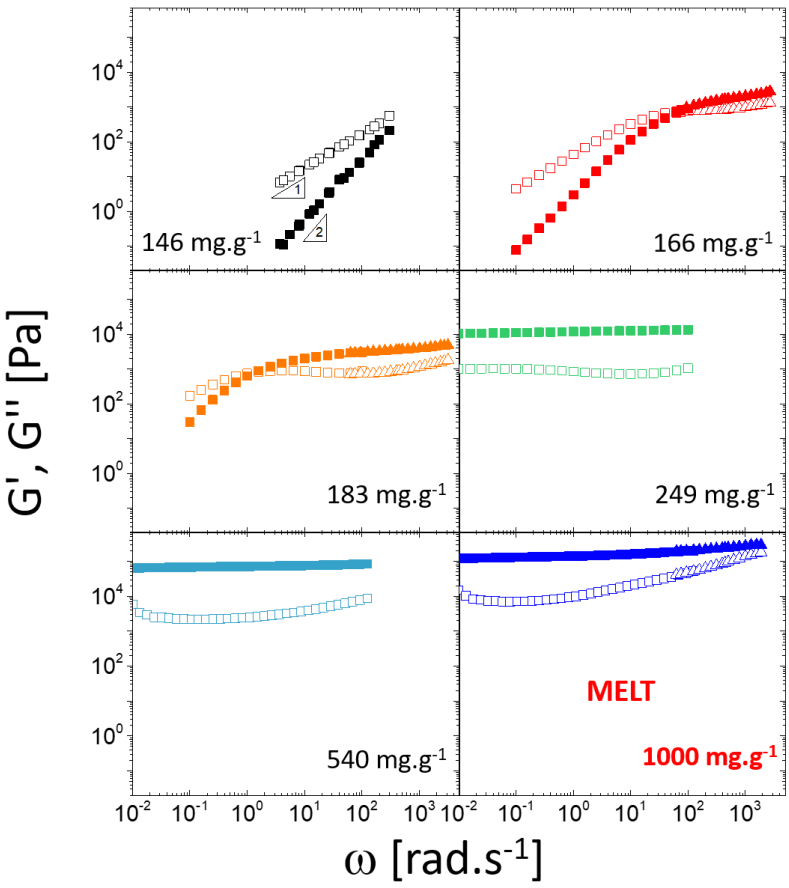

Figure 4-1. Linear viscoelastic spectra of 6 star solutions at different concentrations (f=875, M_a=5.8kg.mol^{-1}). The filled symbols represent the elastic moduli and the empty symbols represent the viscous moduli. The slopes of 1 and 2 are represented besides the data to indicate the terminal regime

At 1.5c*, G' is larger than G" over the whole accessible range of frequency and thus the material is a solid. The magnitude of the elastic modulus increases very weakly with increasing frequency and the viscous modulus follows a non-monotonic frequency dependence with a minimum around 0.5 rad.s^{-1}, typical of colloidal glasses and melts or solutions of entangled polymers. In this case, neither the magnitude of the elastic modulus nor the frequency range correspond to the expected values for polybutadiene solutions or melts. Although no experiments could be performed to verify this, it is strongly believed that this elastic plateau is of colloidal origin, with stars effectively behaving as soft colloidal particles. This behavior was observed for all concentrations higher than 1.5c* and up to the melt (6c*) and no significant qualitative differences were observed. In the melt, previous experiments showed that the elastic modulus indeed plateaus again at higher frequencies, and with a magnitude matching very well the expected value for entangled 1,4-polybutadiene (around 1 MPa). This high frequency plateau is very short and is only observable over about 2 decades in frequency, as expected for such low molecular weight arms (5.8 kg.mol^{-1}). The master curve obtained by means of time-temperature superposition (TTS) for the star melt is shown in Figure 4-2, along with the master curve of linear polybutadiene of the same microstructure, for reference.

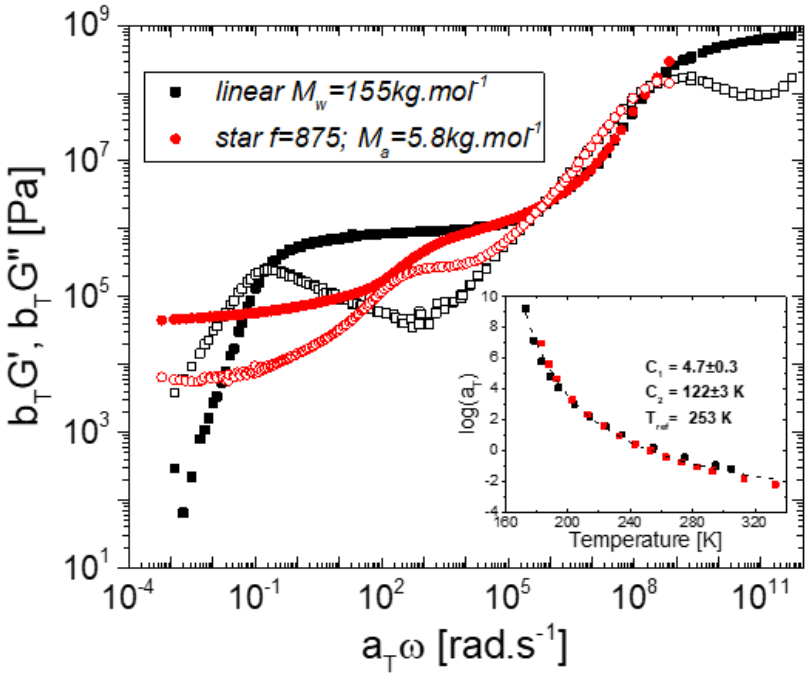

Figure 4-2. Linear viscoelastic spectra of a linear 1,4-polybutadiene polymer and a star 1,4-polybutadiene polymer. The filled symbols represent the elastic moduli and the empty symbols represent the viscous moduli. The master curves were obtained by TTS. Inset: Horizontal shift factor of the same materials along with the best fit to the Williams-Landel-Ferry[22] equation.

Note on the master curve of star polymer melts:

In addition to the observation of two elastic plateaus, we note that no terminal flow was detected at low frequencies, which seems to indicate a jamming of the stars. Because of the lack of materials, no further experiments could be performed on this star polymer. However, efforts have been made towards investigating the low frequency regime for another very dense, similar polybutadiene star (f=929, M_a=4kg.mol^{-1}), using creep in the linear regime to extend the master curve. The results are presented on Figure 4-3, at the same reference temperature as the previous master curve of Figure 4-2. The linear data are converted from the longest waiting time (2 days). Despite the reasonably good overall shape of the full master curve, the conversion of the creep into oscillatory data is subject to error in this case, coming mostly from the inability of the material to relax fully the stress history (see Chapter 5). Therefore, the only robust conclusion that can be drawn from this is a lower bound for the terminal time, taken as $1/\omega_c$ where ω_c is the lowest crossover frequency. For this star, the colloidal plateau extends for at least 9

decades to reach extremely long relaxation times at room temperature. Under these conditions, it is fair to state that jamming effectively takes place in this system.

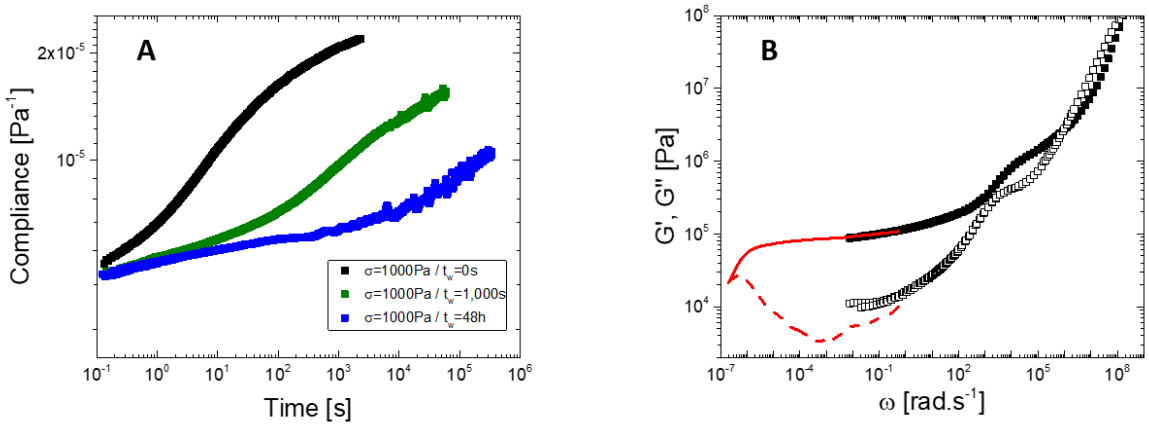

Figure 4-3. A) Creep compliance obtained after different waiting times (see Chapter 5). B) Extended master curve with the converted creep data in red. The black filled and empty symbols represent the elastic and viscous shear moduli respectively, obtained by TTS.

The relative zero-shear viscosity of the suspensions first follows a Batchelor-Einstein increase:

$$\eta_r = 1 + 2.5\varphi + 5.2\varphi^2 \qquad \text{(Equation 1)}$$

where φ=*kc* is the estimated volume fraction in dilute conditions and is proportional to the concentration[23]. At higher concentrations, the zero-shear viscosity increases rapidly and seems to diverge around c*. At the same time, a detectable elastic plateau modulus G_p can be measured and takes the value of G' at the minimum of G" as reported on Figure 4-4. The plateau modulus increases first rapidly with concentration to finally slows down around 2.5c*, similarly to the behavior of previously studied microgels[13]. Beyond this concentration, the increase of plateau modulus becomes close to linear up to the melt. These features provide a rheological division of the concentration range into three regimes: 1) 0-1c*: viscoelastic liquid; 2) 1-2.5c*: soft solid with colloidal glass signatures and 3) 2.5-6c* (melt): jamming regime. We differentiate the jamming regime from the colloidal glass in that the plateau modulus increases linearly with concentration and other signatures in the non-linear regime that will be described below.

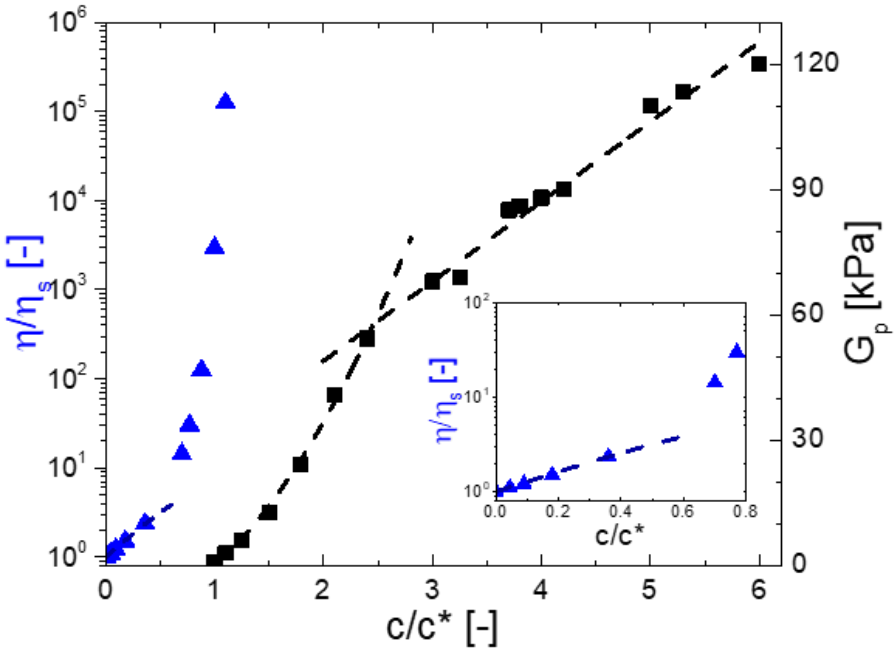

Figure 4-4. Evolution of the relative viscosity (left axis, blue triangles) and the plateau modulus (right axis, black squares) as a function of the reduced concentration of star polymers (f=875, M_a=5.8kg.mol^{-1}). Blue dashed line: the low concentration viscosity data are fitted with the Batchelor-Einstein equation (Equation 1). Black dashed line: power law fit followed by a linear fit to the data. Inset: Zoom on the low concentration regime.

The same analysis of zero-shear viscosity and plateau modulus was applied to the microgels and very similar results were obtained (Figure 4-5). Because it is technically difficult to estimate the molecular weight of each microgel particle, c* is that case was based on the apparition of a plateau in the viscoelastic spectrum, and thus coincides with the first measurable value of G' at the minimum of G". The plateau modulus exhibits the same fast increase as was observed in stars, followed by a slower, linear increase at higher concentration. This behavior was first reported by Cloitre and Pellet[16], and their data are included in the plot of Fig.4-5 at low and intermediate concentrations.

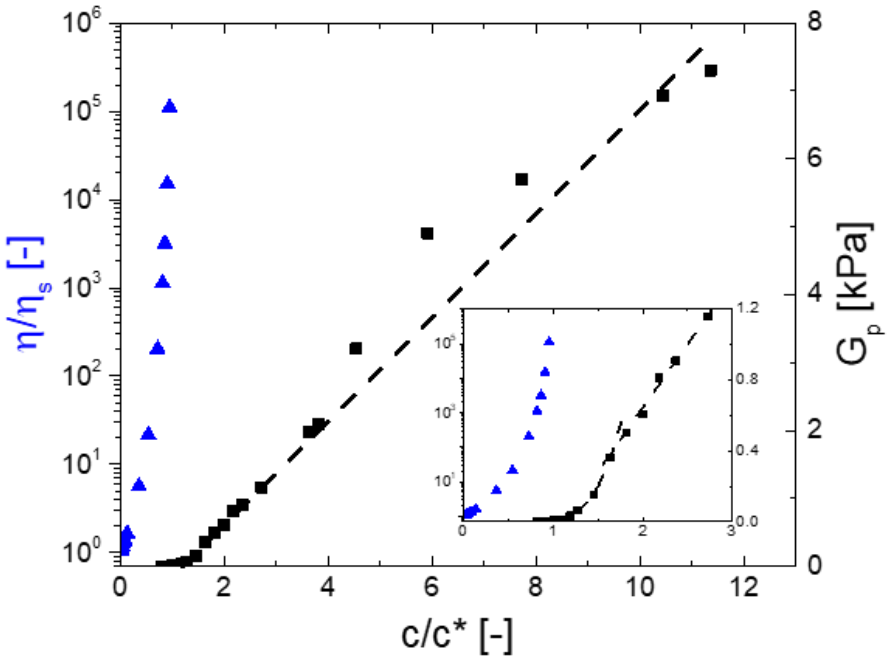

Figure 4-5. Evolution of the relative viscosity (left axis, blue triangles) and the plateau modulus (right axis, black squares) as a function of the reduced concentration of microgels. Black dashed lines: power law fit followed by a linear fit to the data. Inset: Zoom on the low concentration regime.

In conclusion, the linear viscoelastic behavior of stars in solution and the melt appear very complex. The master curve obtained with TTS for two ultra-high-functionality stars show a significant colloidal behavior at low frequencies (room temperature). This was detailed in Chapter 3 and leads to the conclusion that a melt of dense stars is effectively jammed. By changing the concentration, we could follow the evolution of the elasticity of star and microgel suspensions. They appear to be strikingly similar, consisting of a first liquid regime which ends with the divergence of the viscosity and the appearance of a solid regime characterized by the appearance of a plateau elastic modulus. This modulus first increases rather fast with concentration and eventually slows down at a concentration of about 40 wt% (2.5 c*) for stars, beyond which its evolution is linear. We argue that this is the sign of a possible jamming transition in the solid regime of star polymers.

4.3 – Non-linear rheology of concentrated microgel and star solutions

Figure 4-6 shows a series of curves representing the stress measured as function of the applied shear rate, commonly referred to as flow curves. At low concentrations (c<0.7c*) the stress is proportional to the applied shear rate and thus the solutions behave like Newtonian liquids over the entire range of shear rates. When the concentration is increased, the solutions become shear thinning, viscoelastic liquids (0.7c*<c<1.1c*). Upon further increase of the concentration, the solutions finally exhibit a yield stress and the behavior becomes well-predicted by the Herschel-Bulkley model (c>1.5c*), meaning that the steady state stress σ follows the equation

$$\sigma = \sigma_y + k\dot{\gamma}^n \qquad \text{(Equation 2)}$$

where σ_y is he yield stress, k is a fit parameter often called consistency index, $\dot{\gamma}$ is the shear rate and n is the flow index. The solutions therefore gradually transit from the liquid state to the yield stress fluid behavior, i.e., they have solid-like properties at rest but are able to flow under a sufficiently large stress.

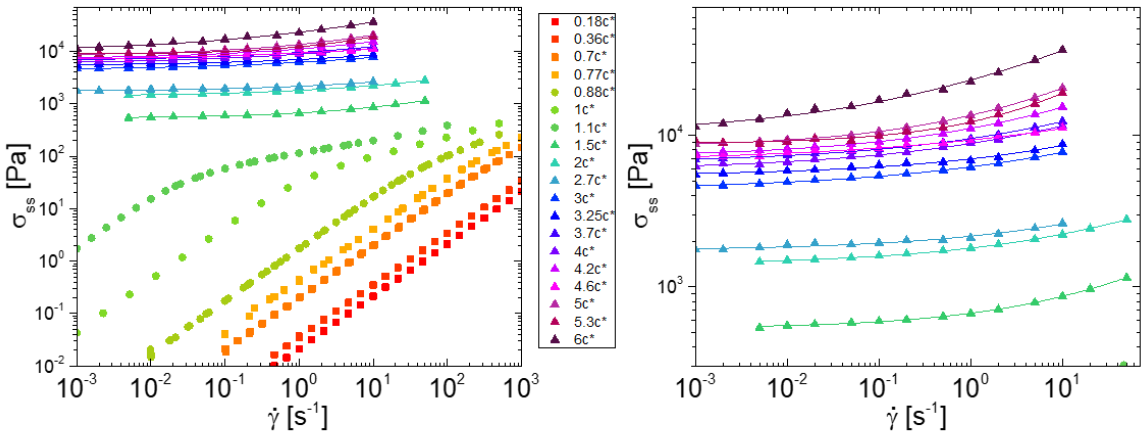

Figure 4-6. Left: Steady-state stress as a function of the shear rate (flow curves) for star solutions from the dilute regime to the melt. Right: Zoom in on the high concentration flow curves. Color coding is the same in both plots.

In the solid state, the stress normalized by the yield stress always follows the Herschel-Bulkley equation above with an approximately constant exponent of 0.3. Although amorphous materials following the Herschel-Bulkley equation (Equation 2) are

ubiquitous[24–28], in the majority of investigated jammed systems the exponent is close to 0.5. In this case, we argue that we barely explore the power-law regime, and therefore the accurate determination of the exponent is difficult and an actual value of 0.5 could be possible.

Because the exponent is always the same though, it is possible to reduce the flow curves at different concentrations into a master curve by horizontally shifting all the data by a shift factor a_C that depends on concentration. The resulting master curve can then be fitted with a Herschel-Bulkley model (Figure 4-7). The determination of a_c is achieved manually by using as a reference the lowest concentration displaying a Herschel-Bulkley behavior (1.5c*). This process is fairly robust and accurate for all concentrations, with an estimated error of about 10% on the value of a_c.

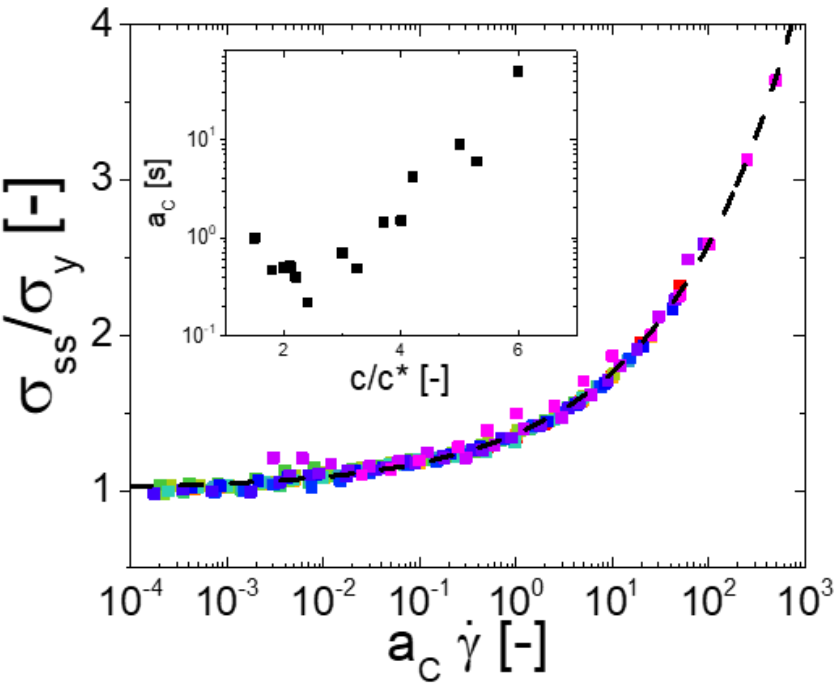

Figure 4-7. Flow maser curve of the solutions and melt of star polymers at different concentration, horizontally shifted. The dashed line is the best fit of the data following the Herschel-Bulkley equation (Equation 2). Inset: Horizontal shift factor as a function of concentration for all the different solutions of star polymers.

From the Heschel-Bulkley fits of the individual flow curves, one can calculate the critical shear rate:

$$\dot{\gamma}_c = (\frac{\sigma_y}{k})^{1/n}$$ (Equation 3)

that determines the boundary between the stress plateau regime for $\dot{\gamma} < \dot{\gamma}_{ch}$and the power-law regime for $\dot{\gamma} > \dot{\gamma}_{ch}$. This characteristic shear rate can also be calculated from the shift factors and the Heschel-Bulkley fit parameters of the master curve. Interestingly, $\dot{\gamma}_{ch}$ exhibits a clear non-monotonic behaviour with concentration. It first increases with increasing concentration up to around 100s^{-1} at c=2.4c* and then decreases rapidly to reach a value of 0.4s^{-1} in the melt state (Figure 4-8). Note that the relative flatness of the flow curves in the experimentally available range of shear rate makes the accurate determination of the parameters of the Herschel-Bulkley equation difficult, especially the flow index n, which has a big influence on the determination of the characteristic shear rate. However, the two methods described above are in very good agreement for all the data and therefore ensure a reliable estimation of the characteristic shear rate. Moreover, since this quantity varies by over two orders of magnitude, it does indeed reflect a change of behavior in the flow of the star suspensions.

The same analysis of the flow curves of microgels revealed a similar behavior of the characteristic shear rate at low concentrations. However, after a first clear increase with concentration, the characteristic shear rate of microgel suspensions only negligibly decreases and arguably remains constant given the measurement uncertainty. Hence, there is a clear qualitative difference between the microgels and the stars flow behavior at high concentration.

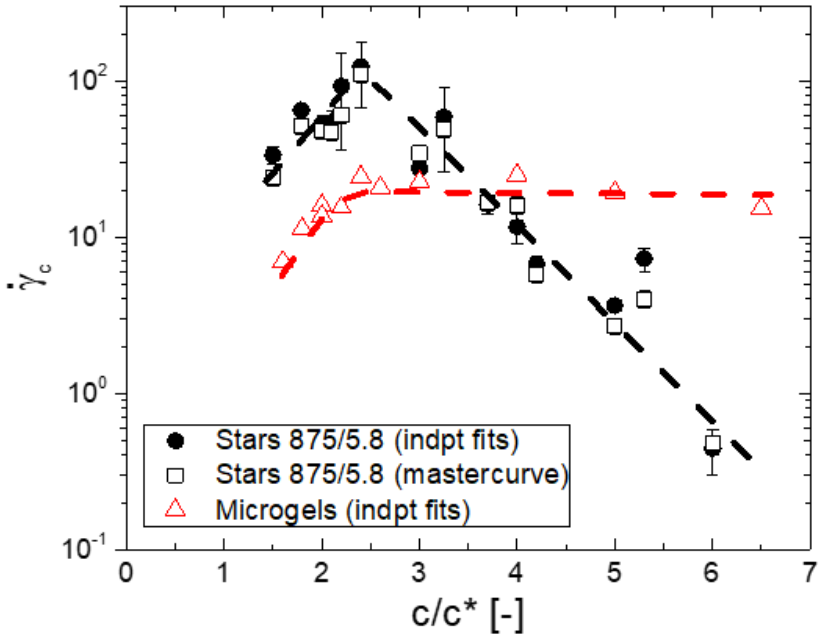

Figure 4-8. Critical shear rate (see text) as a function of the reduced concentration for microgels and star polymers. The dashed lines are a guide to the eye. The critical shear rate can be obtained from two methods for the stars, either by fitting each flow curve to the Herschel-Bukley model (filled black circles) or by fitting the master flow curve (empty black squares).

To explain this difference, we can look at the differences between microgels and stars. One of the most important is the presence of long dangling chains, which are virtually absent in these microgels. Due to their relative homogeneity of crosslinks, the maximum length for a dangling chain in a microgel is the distance between two crosslinks. This represents about 100 monomers, which is very small compared to the size of the particle. On the contrary, star polymers are basically made of dangling chains, except for a very small core in the center. Thus, stars may interdigitate over a small fraction of the chain length when the concentration is increased, which is effectively not possible for microgels. This additional mechanism allows for a different microstructure evolution as the concentration is increased, since it is expected that stars may overlap more at higher concentration. On the contrary, for microgels, the only possible way to increase the number density is to squeeze individual particles in a smaller volume. Thus the packing at higher concentration is the same as for lower concentration, except that the particles are effectively smaller.

A quantitative analysis of the critical shear rate requires more detailed microstructural information and more data with different systems, which are not available at the moment. Hence, we sketch here a suggestive path for interpretation as follows:

In the dilute regime, stars are swollen by the solvent and we can distinguish an external concentration of monomer, which is equal to the average concentration, and an internal concentration of monomers, which is the number of monomers of a star divided by its typical volume. In reality, we expect that the monomer density is a function of the distance from the star centre[19], but for the simplicity of the analysis, we consider it here as an average value throughout the star. In the dilute regime, the internal concentration is what we have referred to so far as the overlap concentration c*, and in practice this is the way this quantity is calculated. In theory, we therefore expect that the internal and the external concentrations become equal when the concentration reaches the overlap concentration (c=c*). In practice, it is known that the particle volume shrinks when the concentration is increased, due to osmotic effect[29,30], and consequently the internal concentration increases. Although the exact dependence of the particle volume on concentration is not known, we expect that it is a decreasing function of the total average concentration (see Appendix I on volume fraction). Whether this can viewed as an effective transition from a good to a theta solvency condition remains unclear.

We argue that the interpenetration of the stars arms cannot occur before the internal and the external (average) concentration become equal, and for the arguments cited above, this can only happen above the overlap concentration (c>c*). In the regime where the concentration is above c* but lower than the interpenetration concentration, particles interact as soft spheres and should therefore resemble the behavior observed in microgels. Since in this regime, deswelling is expected for both systems[16,29], the particles are getting smaller and therefore the critical shear rate increases. However, when interpenetration starts to occur in stars, we expect that a fraction of the energy needed to make particles flow at a given shear rate is used to prevent the favorable interpenetration of stars. Thus we rationalize the increased relative stress needed for the stars to flow compared to the non-interpenetrating microgels. This translates into a steeper flow curve and therefore a smaller critical shear rate. Since we expect interpenetration to become more pronounced as the concentration is increased, this

effect can explain the observed decreasing behavior of the critical shear rates in stars. One may also see in the decreasing critical shear rate a reflection of the increasing disentanglement time of the arms, which can interpenetrate further when the concentration is increased. In fact, one could argue that interpenetration may become the main mechanism allowing for denser packing of stars in this regime, while this is impossible for microgels, which can only shrink. Interestingly, if proven true, this process does not seem to have a significant influence on the linear behavior, while non-linear experiments are more sensitive.

In large-amplitude oscillatory measurements (LAOS), the same transition concentration of about 2.5c* is observed in the oscillatory yield strain of the suspensions (Figure 4-9). Below this concentration, the yield strain measured for stars steadily grows with concentration from 0 in the liquid state until a value of about 0.1. After this characteristic concentration of 2.5c*, the yield strain remains constant within experimental error up to the melt state, showing once again a smooth transition from concentrated suspensions to the melt in terms of rheological properties. The same observations were made in the case of microgel suspensions, which yield strain increased up to a maximum after which it remained constant.

There is an interesting point to be made regarding this increase and the stabilization of the yield strain to a value of about 0.1. First, we note that this is a general observation in most colloidal solids[31]. This value is also reminiscent of the Lindemann criterion for atomic solids[32]. The Lindemann criterion states that the melting of a solid should occur when the thermally-induced vibration of the atoms becomes sufficient for the atoms to collide. In practice, this means that the typical displacement of atoms should be 12% of the lattice size. Colloidal suspensions can be seen as a mesoscale version of atomic liquids and solids[33], which typical size allows for more direct observation techniques like microscopy. In atomic solids, the melting of the crystal is known to be caused by surface atoms, which vibrations are more intense and can therefore nucleate the melting process[34]. As such, it seems that the melting in atomic solids is mainly driven by local heterogeneities of the vibrations, mostly located at the surface for energetic reasons (the protection of the surface increases the effective melting temperature[35], this process is referred to as non-thermal melting),

We argue that a similar process might take place in colloidal suspensions, following the old concept of colloids seen as mesoscale atoms[36]. When the solid forms, local heterogeneities appear since the caging effectively traps the particles in a position that is not the thermodynamic equilibrium. Brownian motion becomes negligible at the experimental time scale, and the system is effectively solid. However, shear may provide additional energy to the system under the form of mechanical energy. In the framework of the Lindemann idea, the spatial heterogeneities of colloidal glasses cause a heterogeneity of the stress at the particle or cluster of particle level, which focuses the mechanical stress in local regions of the sample. These regions will therefore melt, and act as nucleation points for the total yielding of the sample.

When the concentration is increased beyond the solid transition, we expect that the glass becomes more homogeneous because the free volume decreases. Therefore the average cluster size has to increase until it reaches the total size of the sample. A case can be made that this happens at the jamming point, which is coherent with our description of jamming. Since the density heterogeneities gradually disappear, the melting nucleation points become sparse and therefore the yield strain increases. At the jamming, the position of the particles becomes somewhat homogeneous, thus the yield strain is close to the Lindemann value for the melting of solids. In other words, the melting occurs more homogeneously throughout the sample compared to the less dense thermal glass regime, similarly to overheated solids. Upon further increase of the concentration, local homogeneity is maintained and therefore the yield strain keeps a constant value. This provides a reasonable qualitative explanation in agreement with the observed behavior of the yield strain, although structural evidence and additional data would be required to assert this hypothesis.

The oscillatory yield stress is also measured for each of the solutions of stars and microgels, and its value is plotted against the plateau modulus value in Figure 4-9. We find a linear dependence of the oscillatory yield stress with plateau modulus for both the microgels and the stars. Moreover, the star data seem to fit in the continuity of the microgel data, for which the recorded plateau moduli are much smaller. This may indicate a common behavior of this two types of soft colloids, once the differences in particle size and elasticity is taken into account in the plateau modulus value.

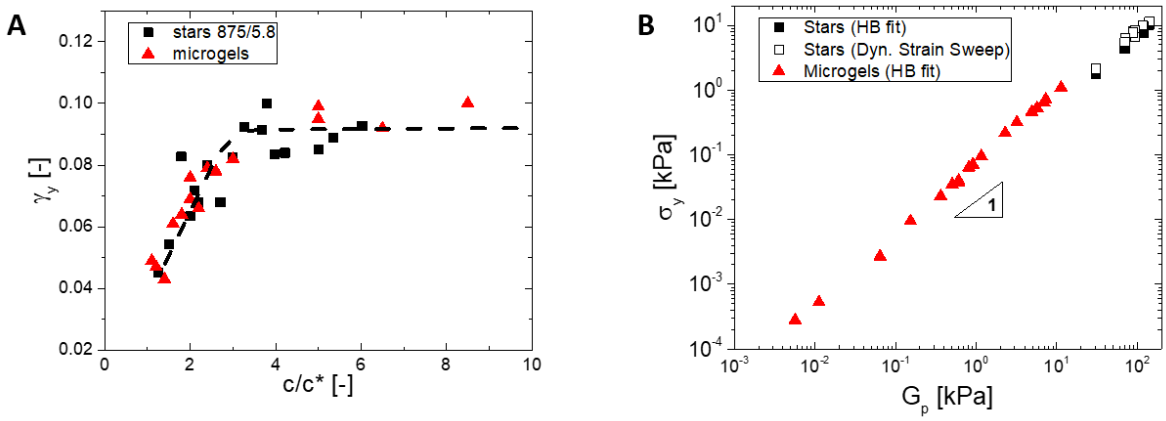

Figure 4-9. A) Oscillatory yield strain for microgel and star polymer solutions. B) Yield stress as a function of the plateau modulus for microgel and star polymer solutions. The yield stress for stars is estimated from oscillatory measurements (empty symbols) and from the fit of the flow curves with a Herschel-Bulkley model (filled symbols).

In conclusion, the analysis of the flow curves and the large amplitude oscillatory shear reveal a change in the flow behavior of star solutions around 2.5 c*, or 40 wt%. This transition was already observed in the evolution of the plateau modulus, and suggests that these stars are able to jam beyond this concentration, by analogy with the results obtained with microgel suspensions. Both systems have remarkable similarities in their nonlinear flow behavior. However, the flow curves obtained with star solutions exhibit a different characteristic shear rate, which severely drops when the concentration is increased beyond the jamming. This may be attributed to one of the biggest differences between these microgels and stars, which is the presence of long dangling ends in the star system.

4.4 - Transient behavior in start-up flow experiments

The transient behavior of the stress-strain curve was measured for stars and microgels and is represented in Figure 4-10. The concentration of stars is 4.2c* (70 wt%) and the concentration of microgels is 3.3 c* (3 wt%). No waiting time was used between the rejuvenation and the start-up flow experiment for the stars. A waiting time of 1000s during which the shear rate was kept to 0 for the microgels. Both systems exhibit a stress overshoot at strains between 10 and 20%, typical of colloidal suspensions of all types[23,37–42]. This is of the same order of magnitude as the typical oscillatory yield strain found in the last section.

Besides this first overshoot, a second broader stress overshoot appears around 300% for the stars only. This second overshoot is peculiar and has not been observed in this type of experiment for purely repulsive soft colloids, however double yielding was suggested in large amplitude oscillatory shear measurements of intermediate functionality polybutadiene stars (f=110) with significantly longer arms (M_a=74.1 kg.mol^{-1})[14]. At the time, the second process was attributed to the disentanglement of the arms and was found to be prone to a strong thixotropic behavior, meaning that the second yielding would disappear in yielded samples.

Examples of a second stress overshoot were also reported for attractive systems, with the first overshoot being attributed to the breaking of the physical bonds between particles, delaying the breaking of the cages to much larger strains and forming a second overshoot[43]. Here, however, the stars are purely repulsive. Overshoots at the same strain were also reported in the case of high molecular weight polymer melts and solutions or low functionality stars[44,45]. In this case, the overshoot corresponds to the extension of the chain by the shear before the retraction and possible tumbling that usually lead to an undershoot. Therefore, this effect is particularly pronounced for long chains and high shear rate, namely at Weissenberg numbers higher than one. Here, the arms of the stars are very short (number of entanglements Z=3), therefore it is difficult to draw an analogy.

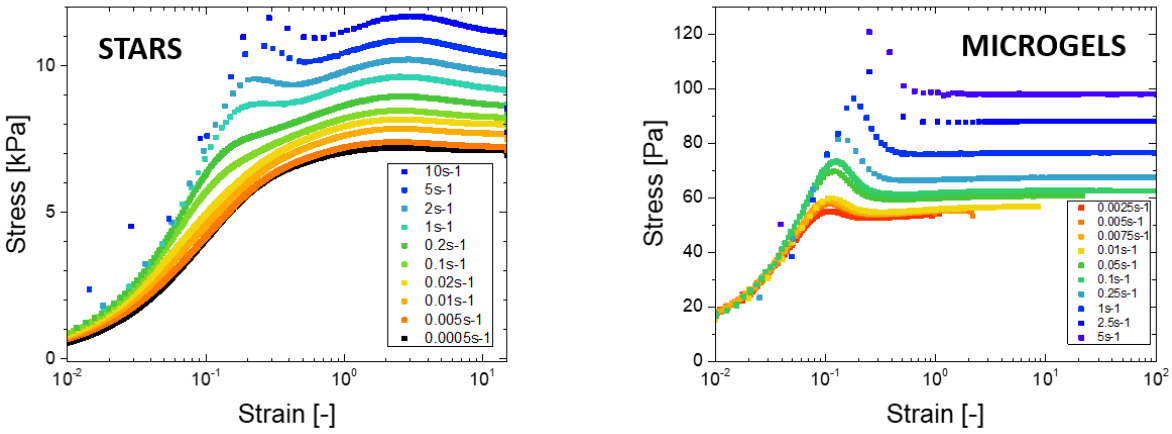

Figure 4-10. Typical series of stress-strain curves for star polymers (left) and microgel solutions (right) obtained during a start-up flow experiment. The concentration of star polymers (left) is 4.2 c (70 wt%) and he concentration of microgels (right) is 3 c* (3.3 wt%).*

Figure 4-11 shows the evolution of the shape of the stress-strain curves for different concentrations from 1.1 c* to the melt. All other parameters that are known to influence the intensity or the position of the overshoots are kept constant, namely the shear rate and the aging time (see below). It is clear from this figure that the first overshoot relatively increases compared to the steady state value, whereas the second overshoot rapidly disappears as the concentration decreases. In fact, below 3c* (which corresponds to 50 wt% of polymer) it is virtually absent. Although the boundary is not very clear, it fits the previously mentioned idea of a transition from a glass regime (c<2.5c*) to a jammed regime (c>2.5c*) that resembles the melt.

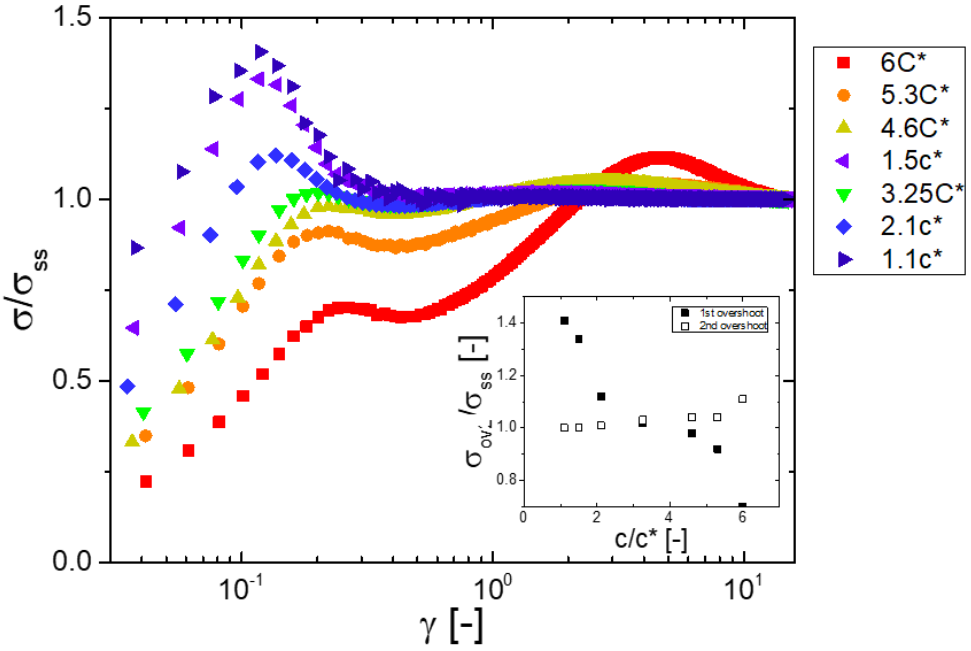

Figure 4-11. Evolution of the stress-strain curves of star polymers as a function of concentration. The stress is divided by the steady state value to make the comparison easier. Inset: Evolution of the first (filled symbols) and 2nd (empty symbols) relative stress overshoot with the concentration of star polymers.

In addition to their dependence in shear rate and concentration, the overshoots, and in particular the first overshoot, also significantly depend on the aging conditions. Each experiment was usually preceded by a rejuvenation step that consisted of a 60s oscillatory shearing at large deformation (100%), so that the material was reset to a reproducible starting state. This rejuvenation has an effect on the results of the

subsequent experiments (see Chapter 5), but this effect is controlled and reproducible. The waiting time between this rejuvenation and the actual experiment that follows is what we call here the age of the sample. It was found, as shown on Figure 4-12, that the waiting time has a significant effect on the relative magnitude of the first overshoot for both microgels and star solutions. The insets in Figure 4-12 represent the evolution of the relative intensity of the overshoots for both stars and microgels. The lin-log representation indicates a logarithmic increase of the 1st overshoot for both systems, while almost no influence is found for the 2nd overshoot.

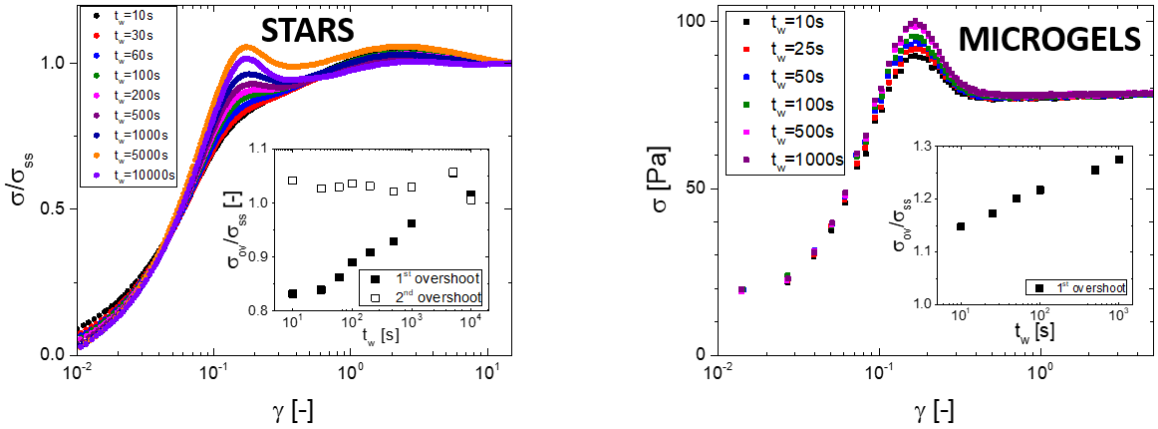

Figure 4-12. Aging of the stress-strain curve for star polymers (left) and microgels (right). The concentration of star polymers is 4.2 c (70 wt%) and the shear rate is 0.1s^{-1}. The concentration of microgels is 3.3 c* (3% wt) and the shear rate is 1s^{-1}. Insets: Aging evolution of the relative intensity of the stress overshoots for star polymers (left) and microgels (right).*

The evolution of the first overshoot with waiting time is a very commonly observed phenomenon in colloidal suspensions, and has been observed in multiple systems with completely different chemistry and structure[40,43,46,47]. While this may point towards a certain universality of the phenomenon, models usually have to account for the particularities of the systems to explain the data. One recurring idea among the different explanations is the build-up of a particular microstructure during the waiting time, which then requires additional energy to break down. This can be for instance the coarsening of a gel, or particle rearrangements towards the thermodynamic equilibrium (crystal) for a glass.

In this case, the 1st overshoot happens at a strain value comparable to the yield strain (10%). This seems to indicate that the overshoot comes from a process at the scale of the particle. Furthermore, the timescale of the build-up is rather long, of the order of 1,000 to 10,000s for both systems. This corresponds very well with the slow decrease of the internal stress resulting from the rejuvenation, which will be described in detail in Chapter 5. The slow relaxation of the internal stress may come from the relaxation of the anisotropy of the particles induced by shear at high deformation[10,48], such as during the rejuvenation experiment. Therefore we suggest that the excess of stress causing the 1st overshoot is due to the deformation of the initially spherical particles along the compression and elongation axes of the shear. Right after the rejuvenation, particles are already anisotropic and therefore no additional stress is needed to deform them. After a long time however, they have relaxed back into a more spherical shape and a higher stress is therefore needed to make them flow. This hypothesis is also in agreement with the observation at different concentrations and shear rates, since we expect the particles to be more pre-deformed at high concentration (therefore the 1st overshoot is relatively smaller) and that a higher shear rate deforms the particles more (therefore the 1st overshoot is relatively bigger).

The case of the 2nd overshoot is peculiar. Based on the strain value, we expect that this overshoot relates to a length scale much bigger than the particles. Since it is absent in microgels, we turn our attention towards the differences between the two systems. One of the main differences is the absence of long dangling ends in the case of microgels, as already mentioned. Based on the understanding developed in the melt rheology (Chapter 3), it seems possible that chains interpenetrate other neighboring stars. This may create an effective transient attraction[49] between neighboring stars, since the disengagement from the neighbors should come at a small but non-zero energy cost.

By analogy with the attractive systems, we may argue that during shear, the stars first deform (origin of the 1st overshoot) and then flow, but bigger clusters are formed. The break-up of these clusters as the flow continues is progressive, thus the very broad character of the 2nd overshoot, and happens at much larger length scales. This may not be the case in more dilute solutions because the interdigitation of the star arms is not

favored, thus explaining the observation that the 2nd overshoot only appears at high concentrations.

By assuming that star arms entangle like linear chains of the same molar mass, we use the well-known scaling law[50] for the diluted entanglement molecular weight $M_e(\varphi) = M_{e(melt)}\varphi^{-1/3}$. When the entanglement molecular weight becomes equal to the arm molecular weight at a concentration of about 40 wt%, or 2.4c* (Figure 4-13), we have the occurrence of entanglements. Although this is an approximation, it is consistent with the experimental data.

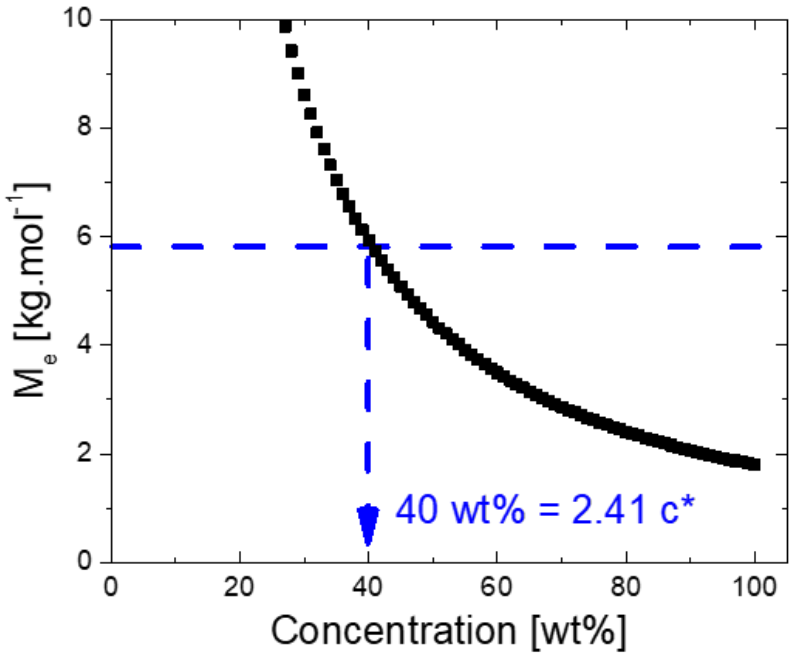

Figure 4-13. Calculation of the effective molar mass between two entanglements for linear 1,4-polybutadiene. The horizontal blue dashed line represent the molar mass of one star arm. The blue dashed arrow points towards the concentration at which one star arm becomes as long as the average length between two entanglements.

In conclusion, the transient behaviors of star and microgel solutions are characterized by a common 1st overshoot, while only the stars exhibit a 2nd overshoot at higher strains. The origin of these overshoots is tentatively (in the absence of structural evidence) attributed to the breaking of microstructure, which is the underlying common explanation for stress overshoots in colloidal suspensions. Based on the evolution of these overshoots with shear rate, concentration and waiting time, we postulate their possible

origin. The first overshoot may result from the slow recovery of the positional anisotropy after shear (in strong connection with Chapter 5), while the second overshoot may arise from the interdigitation of the stars at high concentrations, forming transient clusters. These results need more evidence to be asserted, but the current hypothesis seem to explain the available data.

4.5 - Jamming and the transition towards fragile behavior

Both stars and microgels exhibit a change in the evolution of some of their rheological properties inside the glass regime. For both systems, this manifests as a slowdown of the increase of the plateau modulus vs concentration and a saturation of the oscillatory yield strain to a maximum value of about 10%. In addition, we also observe a peak of the critical shear rate of the flow curves of stars at the same concentration, which seems to roughly correspond to the critical concentration at which entanglements could form in linear polymers of the size of the stars arms. The development of a second overshoot in the transient regime of start-up flow experiments also highlights the importance of the dangling ends in stars, which are absent in the microgels. Overall, we tried to bring more elements towards the understanding of the solid regime in soft colloids, by comparing the two main model systems and linking the macroscopic properties to their microstructure.

Another approach of this question is to consider the liquid-to-solid transition as an effective phase transition, and therefore some properties of the sample should depend not on the absolute value of the concentration, but rather on the distance from the transition. A well-known example is the divergence of the viscosity at the solidification point[17,23]. For hard spheres, different models have been developed through the years[51–53], but they all agree on the divergence of the viscosity as a power law of the distance of the volume fraction to the critical volume fraction, most often called maximum packing fraction[54]. For some colloids, the determination of this critical packing fraction is often delicate, since the softness allows for shape and size changes with the concentration. Experimentally however, the viscosity of many soft systems can be fitted to the same functional form as hard spheres, and allows for the determination of the maximum packing fraction. In Appendix I, we also propose a naïve model for the determination of

the volume fraction of soft colloids based on the mapping to hard sphere viscosity. Here, we focus the idea that properties may depend on the distance from the transition.

In the solid regime, we propose a scaling of the plateau modulus as a function of the difference between the concentration and a critical concentration, that we call c_j (Figure 4-14). This critical concentration is obtained for the stars by manual trial-and-error until a slope of 1 is achieved. Then the corresponding value of the plateau modulus $G_{p,j}=G_p(c_j)$ is used to normalize the value of the plateau modulus. After this step, we manually adjust c_j for all the other systems to superimpose the data on the star data.

By dividing the elastic modulus value by its value at the concentration c_j, we account for the different chemistry, size or suspending medium properties. On Figure 4-14, we see that the data for the stars and the microgels collapses very well, and have a linear dependence on the distance to the critical concentration. In addition, we have also added numerous other systems from the literature, with different chemistry (PB[28,55], PS[56] and PMMAcoPMA[13,16]), structure (stars, microgels and micelles), softness and even shape (cylinders and spheres).

This scaling highlights the possible universality of the evolution of the elastic modulus in numerous, very different soft systems. On Figure 4-14, we show both a log-lin and a log-log scaling to better appreciate the behavior of the different systems before the critical concentration c_j. In particular, we find that for of these systems, the critical concentration is very close to the concentration at which the liquid-to-solid transition occurs, postulating that the jamming regime actually appears very early in the solid regime. In the case of the very high functionality stars studied in detail here, the overlap concentration (16 wt%) and the critical concentration (17wt%) could be considered the same. Although the linear scaling of the plateau modulus in the jammed regime was already reported before for microgels[16], the similarities brought up by this analysis concern all types of systems. In particular, the data set “soft stars” on Figure 4-14 represent data from the literature[28] for stars with a functionality of f=391 and a molecular weight of the arms of M_a=24.4 kg.mol^{-1}. The functionality is therefore much lower than the one of the stars that have been studied here, and the arms are significantly longer as well. Thus this analogy is not limited to extreme cases of star polymers.

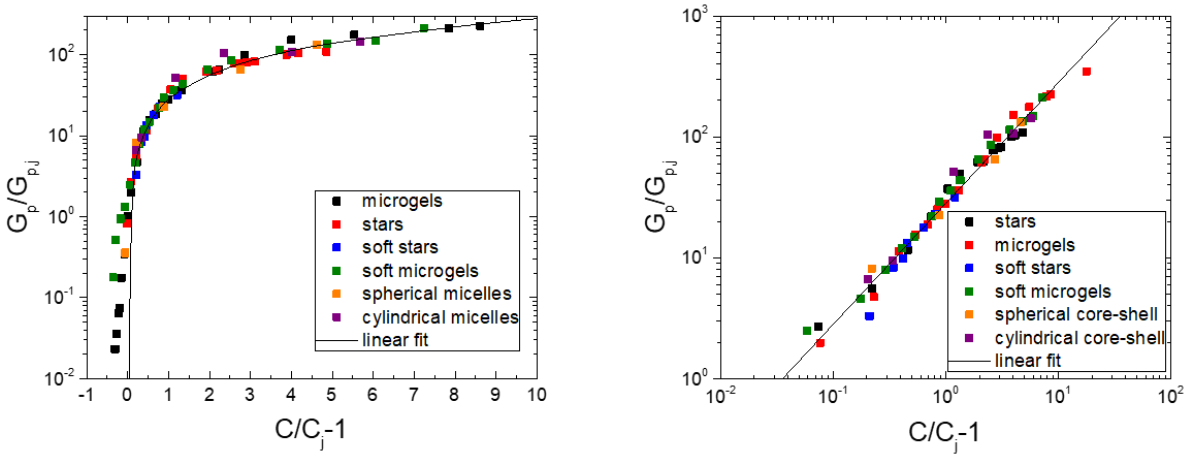

Figure 4-14. The dependence of the elastic plateau modulus G_p, normalized by its value at the critical concentration $G_{p,j}$, as a function of the normalized distance to the jamming point c/cj-1. Left: The log-lin scaling displays the data before and after the critical concentration cj. Right: The log-log scaling shows the linear dependence of the plateau modulus in the jamming region.

In the framework of colloidal glasses, one can distinguish two types of glasses. The thermal glass marks the apparition of the solid regime and the divergence of the viscosity. The elasticity is dominated by excluded volume interactions at the size of the particles, meaning that the particles are effectively trapped in a cage of neighbors, which restricts their long-time diffusion. This is the glass formed by pure hard spheres[3,24,57,58,58], since their interaction potential becomes infinite at contact. This is the reason why the elastic modulus of hard sphere glasses ultimately scales with the thermal energy per unit volume:

$$G_p \sim \frac{k_B T}{R^3} \qquad \text{(Equation 3)}$$

where k_B is the Boltzmann constant, T is the temperature and R is the particle radius.

On the other hand, soft colloids can interact beyond their contact point, which leaves room for denser packings. The transition from an entropy-dominated solid to a contact-dominated solid is what we call jamming[25]. In this regime, we expect the elasticity of the bulk material to come primarily from the deformation of the individual particles composing it. This is accounted for in Figure 4-14 in the rescaling by the critical modulus $G_{p,j}$. Based on this representation, it seems that jamming is a common feature throughout a wide range of soft systems despite different physics and interactions between the particles.

One may then wonder what happens when the concentration keeps increasing way beyond the jamming transition. For the dense stars studied here, the maximum concentration is the melt, where no solvent is present. From the available data shown in this chapter, the transition from the solution to the melt seems gradual, with no specific changes in the rheological properties. From the jamming point up, the material properties evolve smoothly to the melt properties. For microgels, the situation is different. In theory, since c*=0.9 wt%, we may expect that the pure material should have a maximum concentration of about 100 times the overlap concentration. However, it is very difficult experimentally to obtain homogeneous solutions with a concentration beyond 10 to 15 times the overlap concentration.

At these concentrations, we start to observe that the material behaves more and more like a macroscopic gel and less like a typical colloidal glass. From a rheological point of view, it becomes impossible to make the material flow, and any experiment carried out in the nonlinear regime results in the breaking of the sample. This is manifested for example in the absence of steady state in the start-up experiments, even at moderate shear rates, as shown on figure 4-15 below. This behavior was not observed for stars up to the melt state, and steady state could always be obtained consistently at low and moderate shear rates ($\dot{\gamma} < 10s^{-1}$).

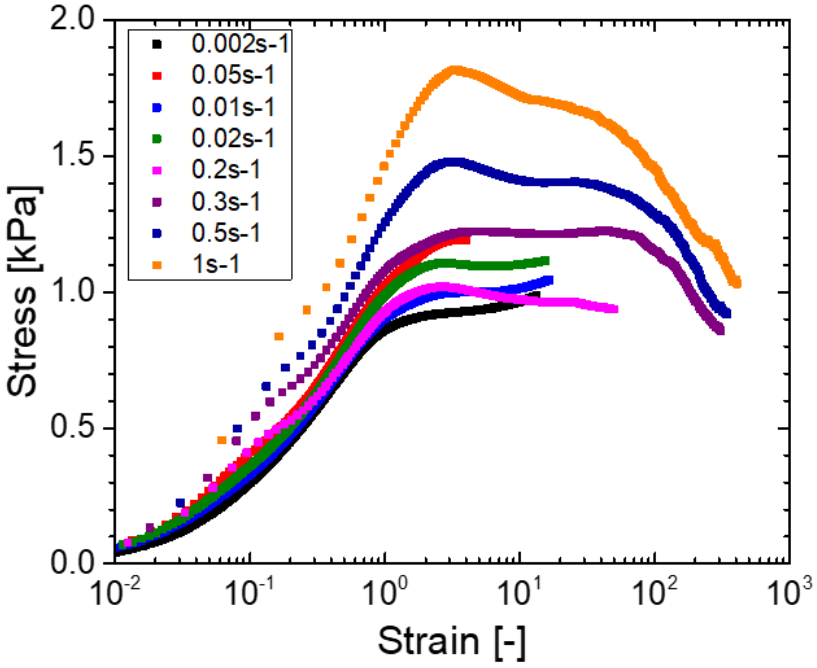

Figure 4-15. Stress-strain curves of a highly concentrated microgel solution (12 wt%) at different shear rates. The steady state is never achieved because the material breaks at high strains.

In situ measurement of the flow profiles during the shearing of highly concentrated microgel solution using particle imaging velocimetry (PIV) were made and showed a significant variation with time. This was interpreted as the signature of transient shear banding, and was coherent with the macroscopic observation that the material could not flow. This is shown on Figure 4-16, along with close-up photographs of the material in this high concentration regime (15 wt%) compared to the jammed regime (5 wt%). The theoretical linear flow profile is also represented as a reference. We used for this experiment a metal cone and a glass plate with a diameter of 40mm and a cone angle of 2. The differences observed at the lower concentration come from the slipping of the sample on the bottom glass plate, as will be further investigated in Appendix II.

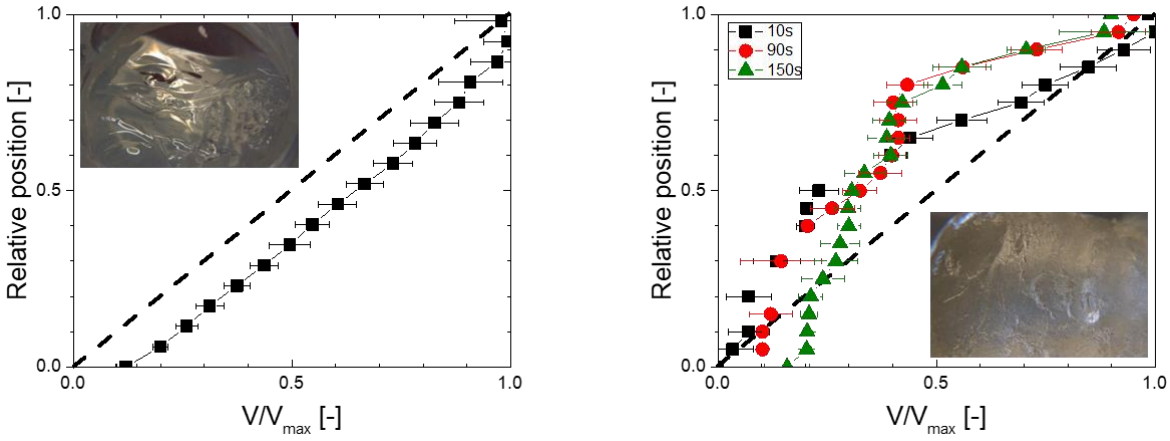

Figure 4-16. Flow profiles of a 5 wt% (left) and a 12 wt% (right) of microgels measured with PIV. The dashed lines represent the theoretical flow profiles. For the 12 wt% solution, flow profiles were measured at different times after the start of the shear (see caption). Close-up photographs of the material are in inset to show the visual differences of the two solutions.

As a conclusion, we showed that the jamming regime of different types of soft systems with different characteristic can be compared using an appropriate scaling based on the distance from the jamming point. When properly rescaled, the elastic modulus of all these different soft colloidal particles has a similar evolution with the concentration, which suggests that jamming may be in fact a common feature of many soft systems. However, the experimentally accessible range of concentrations is different is these different colloidal particles. We took as an example the difference between stars, which can be used in the melt state, and the microgels, which form heterogeneous, breakable solids when the concentration is increased beyond 10 to 15 times their overlap concentration.

4.6 – Conclusions

This chapter presented in details the comparison of the rheological behavior of two model soft systems, star polymers and microgels. The stars were chosen for their extremely high functionality (f=875 arms) and low molecular weight of the arms (Ma=5.8 kg.mol^{-1}) to bridge the softness gap between stars and microgels. The systematic comparison of the two systems revealed striking resemblances, leading to the conclusion that these stars could indeed jam similarly to what had been found for microgels. This elasticity in this regime mostly comes from the elastic contacts between the soft particles,

contrary to the thermal glass where elasticity is dominated by the thermal energy k_BT. This is manifested in rheology by a slower increase of the elastic plateau modulus vs concentration and the capping of the yield strain to about 10%. In addition, we found that stars also exhibit differences compared to microgels in this regime. The appearance of a second overshoot in the transient regime of start-up flow experiments and the non-monotonic behavior of the critical shear rate of flow curves have not been reported for microgels, and we argue that these differences arise from the interdigitation of dangling chains in stars, which are absent in these microgels.

We have extended our analysis by rescaling the concentrations of multiple soft systems to highlight the similar evolution of the elastic plateau modulus in the jammed regime. As is the case for viscosity in the liquid-to-solid transition, the value of the plateau modulus of jammed systems depends on the distance from the jamming point, and we found a linear dependence holds true for various soft colloidal suspensions such as core-shell particles, microgels and star polymers. Finally, we showed that the experimentally accessible range of concentrations is ultimately limited for microgels, which form fragile solids at very high concentrations. For star polymers, there is a smooth evolution from the jammed regime to the melt, which marks a departure from microgels.

References

(1) Weeks, E. R. Three-Dimensional Direct Imaging of Structural Relaxation Near the Colloidal Glass Transition. *Science* **2000**, *287* (5453), 627–631. https://doi.org/10.1126/science.287.5453.627.

(2) Mattsson, J.; Wyss, H. M.; Fernandez-Nieves, A.; Miyazaki, K.; Hu, Z.; Reichman, D. R.; Weitz, D. A. Soft Colloids Make Strong Glasses. *Nature* **2009**, *462* (7269), 83–86. https://doi.org/10.1038/nature08457.

(3) van Megen, W.; Pusey, P. N. Dynamic Light-Scattering Study of the Glass Transition in a Colloidal Suspension. *Physical Review A* **1991**, *43* (10), 5429–5441. https://doi.org/10.1103/PhysRevA.43.5429.

(4) Mason, T. G.; Weitz, D. A. Linear Viscoelasticity of Colloidal Hard Sphere Suspensions near the Glass Transition. *Phys. Rev. Lett.* **1995**, *75* (14), 2770.

(5) van Megen, W.; Underwood, S. M. Glass Transition in Colloidal Hard Spheres: Mode-Coupling Theory Analysis. *Phys. Rev. Lett.* **1993**, *70* (18), 2766–2769. https://doi.org/10.1103/PhysRevLett.70.2766.

(6) Gotze, W.; Sjogren, L. Relaxation Processes in Supercooled Liquids. *Reports on Progress in Physics* **1992**, *55* (3), 241–376. https://doi.org/10.1088/0034-4885/55/3/001.

(7) Schweizer, K. S.; Saltzman, E. J. Entropic Barriers, Activated Hopping, and the Glass Transition in Colloidal Suspensions. *The Journal of Chemical Physics* **2003**, *119* (2), 1181–1196. https://doi.org/10.1063/1.1578632.
(8) Schweizer, K. S.; Yatsenko, G. Collisions, Caging, Thermodynamics, and Jamming in the Barrier Hopping Theory of Glassy Hard Sphere Fluids. *The Journal of Chemical Physics* **2007**, *127* (16), 164505. https://doi.org/10.1063/1.2780861.
(9) Lyon, L. A.; Fernandez-Nieves, A. The Polymer/Colloid Duality of Microgel Suspensions. *Annual Review of Physical Chemistry* **2012**, *63* (1), 25–43. https://doi.org/10.1146/annurev-physchem-032511-143735.
(10) Mohan, L.; Bonnecaze, R. T.; Cloitre, M. Microscopic Origin of Internal Stresses in Jammed Soft Particle Suspensions. *Physical Review Letters* **2013**, *111* (26). https://doi.org/10.1103/PhysRevLett.111.268301.
(11) Seth, J. R.; Cloitre, M.; Bonnecaze, R. T. Elastic Properties of Soft Particle Pastes. *J. Rheol.* **2006**, *50* (3), 353–376. https://doi.org/10.1122/1.2186982.
(12) Bouhid de Aguiar, I.; van de Laar, T.; Meireles, M.; Bouchoux, A.; Sprakel, J.; Schroën, K. Deswelling and Deformation of Microgels in Concentrated Packings. *Scientific Reports* **2017**, *7* (1). https://doi.org/10.1038/s41598-017-10788-y.
(13) Cloitre, M.; Borrega, R.; Monti, F.; Leibler, L. Structure and Flow of Polyelectrolyte Microgels: From Suspensions to Glasses. *Comptes Rendus Physique* **2003**, *4* (2), 221–230. https://doi.org/10.1016/S1631-0705(03)00046-X.
(14) Helgeson, M. E.; Wagner, N. J.; Vlassopoulos, D. Viscoelasticity and Shear Melting of Colloidal Star Polymer Glasses. *Journal of Rheology* **2007**, *51* (2), 297–316. https://doi.org/10.1122/1.2433935.
(15) Bonn, D.; Denn, M. M.; Berthier, L.; Divoux, T.; Manneville, S. Yield Stress Materials in Soft Condensed Matter. *Reviews of Modern Physics* **2017**, *89* (3). https://doi.org/10.1103/RevModPhys.89.035005.
(16) Pellet, C.; Cloitre, M. The Glass and Jamming Transitions of Soft Polyelectrolyte Microgel Suspensions. *Soft Matter* **2016**, *12* (16), 3710–3720. https://doi.org/10.1039/C5SM03001C.
(17) Vlassopoulos, D.; Cloitre, M. Tunable Rheology of Dense Soft Deformable Colloids. *Curr. Opi. Colloid Int. Sci.* **2014**, *19* (6), 561–574. https://doi.org/10.1016/j.cocis.2014.09.007.
(18) Truzzolillo, D.; Marzi, D.; Marakis, J.; Capone, B.; Camargo, M.; Munam, A.; Moingeon, F.; Gauthier, M.; Likos, C. N.; Vlassopoulos, D. Glassy States in Asymmetric Mixtures of Soft and Hard Colloids. *Phys. Rev. Lett.* **2013**, *111* (20). https://doi.org/10.1103/PhysRevLett.111.208301.
(19) Daoud, M.; Cotton, J. P. Star Shaped Polymers : A Model for the Conformation and Its Concentration Dependence. *Journal de Physique* **1982**, *43* (3), 531–538. https://doi.org/10.1051/jphys:01982004303053100.
(20) Pakula, T.; Vlassopoulos, D.; Fytas, G.; Roovers, J. Structure and Dynamics of Melts of Multiarm Polymer Stars. *Macromol.* **1998**, *31* (25), 8931–8940. https://doi.org/10.1021/ma981043r.
(21) Roovers, J.; Zhou, L. L.; Toporowski, P. M.; van der Zwan, M.; Iatrou, H.; Hadjichristidis, N. Regular Star Polymers with 64 and 128 Arms. Models for Polymeric Micelles. *Macromol.* **1993**, *26* (16), 4324–4331. https://doi.org/10.1021/ma00068a039.

(22) Williams, M. L.; Landel, R. F.; Ferry, J. D. The Temperature Dependence of Relaxation Mechanisms in Amorphous Polymers and Other Glass-Forming Liquids. *Journal of the American Chemical Society* **1955**, *77* (14), 3701–3707. https://doi.org/10.1021/ja01619a008.
(23) Mewis, J.; Wagner, N. J. *Colloidal Suspension Rheology*; Cambridge series in chemical engineering; Cambridge University Press: Cambridge ; New York, 2012.
(24) Koumakis, N.; Pamvouxoglou, A.; Poulos, A. S.; Petekidis, G. Direct Comparison of the Rheology of Model Hard and Soft Particle Glasses. *Soft Matter* **2012**, *8* (15), 4271. https://doi.org/10.1039/c2sm07113d.
(25) Seth, J. R.; Mohan, L.; Locatelli-Champagne, C.; Cloitre, M.; Bonnecaze, R. T. A Micromechanical Model to Predict the Flow of Soft Particle Glasses. *Nat. Mater* **2011**, *10* (11), 838–843. https://doi.org/10.1038/nmat3119.
(26) Lin, J.; Wyart, M. Microscopic Processes Controlling the Herschel-Bulkley Exponent. *Physical Review E* **2018**, *97* (1). https://doi.org/10.1103/PhysRevE.97.012603.
(27) Agoritsas, E.; Martens, K. Non-Trivial Rheological Exponents in Sheared Yield Stress Fluids. *Soft Matter* **2017**, *13* (26), 4653–4660. https://doi.org/10.1039/C6SM02702D.
(28) Erwin, B. M.; Cloitre, M.; Gauthier, M.; Vlassopoulos, D. Dynamics and Rheology of Colloidal Star Polymers. *Soft Matter* **2010**, *6* (12), 2825–2833. https://doi.org/10.1039/B926526K.
(29) Truzzolillo, D.; Vlassopoulos, D.; Gauthier, M. Osmotic Interactions, Rheology, and Arrested Phase Separation of Star–Linear Polymer Mixtures. *Macromol.* **2011**, *44* (12), 5043–5052. https://doi.org/10.1021/ma2007078.
(30) Truzzolillo, D.; Vlassopoulos, D.; Munam, A.; Gauthier, M. Depletion Gels from Dense Soft Colloids: Rheology and Thermoreversible Melting. *Journal of Rheology* **2014**, *58* (5), 1441–1462. https://doi.org/10.1122/1.4866592.
(31) Derks, D.; Wu, Y. L.; van Blaaderen, A.; Imhof, A. Dynamics of Colloidal Crystals in Shear Flow. *Soft Matter* **2009**, *5* (5), 1060. https://doi.org/10.1039/b816026k.
(32) F. A. Lindemann. *Physikalisch Zeitschrift* **1910**, *11* (14), 610.
(33) Poon, W. C. K. Colloids as Big Atoms: The Genesis of a Paradigm. *Journal of Physics A: Mathematical and Theoretical* **2016**, *49* (40), 401001. https://doi.org/10.1088/1751-8113/49/40/401001.
(34) Cahn, R. W. Melting from Within. *Nature* **2001**, *413* (6856), 582–583. https://doi.org/10.1038/35098169.
(35) Rousse, A.; Rischel, C.; Fourmaux, S.; Uschmann, I.; Sebban, S.; Grillon, G.; Balcou, Ph.; Förster, E.; Geindre, J. P.; Audebert, P.; et al. Non-Thermal Melting in Semiconductors Measured at Femtosecond Resolution. *Nature* **2001**, *410* (6824), 65–68. https://doi.org/10.1038/35065045.
(36) Pusey, P. N.; van Megen, W. Phase Behaviour of Concentrated Suspensions of Nearly Hard Colloidal Spheres. *Nature* **1986**, *320* (6060), 340–342. https://doi.org/10.1038/320340a0.
(37) Yan, Z.-C.; Costanzo, S.; Jeong, Y.; Chang, T.; Vlassopoulos, D. Linear and Nonlinear Shear Rheology of a Marginally Entangled Ring Polymer. *Macromol.* **2016**, *49* (4), 1444–1453. https://doi.org/10.1021/acs.macromol.5b02651.

(38) Costanzo, S.; Scherz, L. F.; Schweizer, T.; Kröger, M.; Floudas, G.; Schlüter, A. D.; Vlassopoulos, D. Rheology and Packing of Dendronized Polymers. *Macromol.* **2016**, *49* (18), 7054–7068. https://doi.org/10.1021/acs.macromol.6b01311.
(39) Koumakis, N.; Petekidis, G. Two Step Yielding in Attractive Colloids: Transition from Gels to Attractive Glasses. *Soft Matter* **2011**, *7* (6), 2456. https://doi.org/10.1039/c0sm00957a.
(40) Berret, J.-F. Transient Rheology of Wormlike Micelles. *Langmuir* **1997**, *13* (8), 2227–2234. https://doi.org/10.1021/la961078p.
(41) Derec, C.; Ducouret, G.; Ajdari, A.; Lequeux, F. Aging and Nonlinear Rheology in Suspensions of Polyethylene Oxide–Protected Silica Particles. *Physical Review E* **2003**, *67* (6). https://doi.org/10.1103/PhysRevE.67.061403.
(42) Koumakis, N.; Laurati, M.; Egelhaaf, S. U.; Brady, J. F.; Petekidis, G. Yielding of Hard-Sphere Glasses during Start-Up Shear. *Phys. Rev. Lett.* **2012**, *108* (9). https://doi.org/10.1103/PhysRevLett.108.098303.
(43) Moghimi, E.; Jacob, A. R.; Koumakis, N.; Petekidis, G. Colloidal Gels Tuned by Oscillatory Shear. *Soft Matter* **2017**, *13* (12), 2371–2383. https://doi.org/10.1039/C6SM02508K.
(44) Maxwell, B.; Nguyen, M. Measurement of the Elastic Properties of Polymer Melts. *Polymer Engineering and Science* **1979**, *19* (16), 1140–1150. https://doi.org/10.1002/pen.760191603.
(45) Snijkers, F.; Ratkanthwar, K.; Vlassopoulos, D.; Hadjichristidis, N. Viscoelasticity, Nonlinear Shear Start-up, and Relaxation of Entangled Star Polymers. *Macromolecules* **2013**, *46* (14), 5702–5713. https://doi.org/10.1021/ma400662b.
(46) Letwimolnun, W.; Vergnes, B.; Ausias, G.; Carreau, P. J. Stress Overshoots of Organoclay Nanocomposites in Transient Shear Flow. *Journal of Non-Newtonian Fluid Mechanics* **2007**, *141* (2–3), 167–179. https://doi.org/10.1016/j.jnnfm.2006.11.003.
(47) Li, J.; Zhou, C.; Wang, G.; Zhao, D. Study on Rheological Behavior of Polypropylene/Clay Nanocomposites. *Journal of Applied Polymer Science* **2003**, *89* (13), 3609–3617. https://doi.org/10.1002/app.12643.
(48) Mohan, L.; Cloitre, M.; Bonnecaze, R. T. Build-up and Two-Step Relaxation of Internal Stress in Jammed Suspensions. *J. Rheol.* **2015**, *59* (1), 63–84. https://doi.org/10.1122/1.4901750.
(49) Briels, W. J. Transient Forces in Flowing Soft Matter. *Soft Matter* **2009**, *5* (22), 4401. https://doi.org/10.1039/b911310j.
(50) Michael Rubinstein, Ralph H Colby. *Polymer Physics*; Oxford University Press: Oxford, 2003.
(51) Mendoza, C. I.; Santamar?a-Holek, I. The Rheology of Hard Sphere Suspensions at Arbitrary Volume Fractions: An Improved Differential Viscosity Model. *The Journal of Chemical Physics* **2009**, *130* (4), 044904. https://doi.org/10.1063/1.3063120.
(52) Quemada, D. Rheology of Concentrated Disperse Systems II. A Model for Non-Newtonian Shear Viscosity in Steady Flows. *Rheologica Acta* **1978**, *17* (6), 632–642. https://doi.org/10.1007/BF01522036.
(53) Krieger, I. M.; Dougherty, T. J. A Mechanism for Non-Newtonian Flow in Suspensions of Rigid Spheres. *Transactions of the Society of Rheology* **1959**, *3* (1), 137–152. https://doi.org/10.1122/1.548848.

(54) Philippe, A.-M.; Truzzolillo, D.; Galvan-Myoshi, J. The Glass Transition of Soft Colloids. 10.
(55) Gauthier, M.; Munam, A. Synthesis of 1,4-Polybutadiene Dendrimer−Arborescent Polymer Hybrids. *Macromolecules* **2010**, *43* (8), 3672–3681. https://doi.org/10.1021/ma1004056.
(56) Ruan, Y.; Gao, L.; Yao, D.; Zhang, K.; Zhang, B.; Chen, Y.; Liu, C.-Y. Polymer-Grafted Nanoparticles with Precisely Controlled Structures. *ACS Macro Letters* **2015**, *4* (10), 1067–1071. https://doi.org/10.1021/acsmacrolett.5b00408.
(57) Zaccarelli, E.; Poon, W. C. K. Colloidal Glasses and Gels: The Interplay of Bonding and Caging. *PNAS* **2009**, *106* (36), 15203–15208. https://doi.org/10.1073/pnas.0902294106.
(58) Pusey, P. N.; Zaccarelli, E.; Valeriani, C.; Sanz, E.; Poon, W. C. K.; Cates, M. E. Hard Spheres: Crystallization and Glass Formation. *Philosophical Transactions of the Royal Society A: Mathematical, Physical and Engineering Sciences* **2009**, *367* (1909), 4993–5011. https://doi.org/10.1098/rsta.2009.0181.

Chapter 5 - Stress relaxation and internal stresses

Abstract

This chapter focuses on the stress relaxation mechanisms of star polymer solutions and melt following the cessation of steady shear flow, which is obviously in strong relation with the different mechanisms associated with yielding and the flow behavior. Indeed, we find that the stress relaxation is very slow in the concentrated solutions of star polymers, as already suggested by the extremely long relaxation time of the shear modulus and the aging behavior. Similarly to what has been observed in microgels and hard spheres, the stress relaxation of star glasses can be separated into two processes. The fast process appears primarily associated with the relaxation of the viscous stress, described by the Herschel-Bulkley model. The second process is always present, even below the yield stress in the linear regime, and is associated with the slow motion of displaced particles back to their initial configuration. In addition, we show that the typical length scales of both processes seem to scale with the inverse of the pre-shear rate preceding the relaxation. We find that the stress relaxation is extremely sensitive to shear history. Finally, we show that low-stress value creep experiments provide a good way to explore the non-yielded relaxation behavior of the star solutions, which is dominated by the effect of the internal stress.

5.1 - Introduction

Stars with an extremely high number of small arms show a very rich rheological behavior, as demonstrated in Chapters 3 and 4 of this work. At high concentration in a good solvent, they form a solid disordered phase, commonly referred to as a glass, which can be described as a yield stress fluid. At rest, these star solutions do not show any terminal regime[1], meaning that the diffusion of particles is extremely slow compared to the experimental time scale. Effectively, they behave as jammed soft colloids. However, under a stress larger than their yield stress, star solutions are able to deform and/or flow, meaning that their microstructure is able to rearrange in order to accommodate for the relative motion of particles.

This property makes these stars (and yield stress fluids in general) a type of material with solid properties in the linear regime, where the stress and the deformation are small, that turn into liquid properties in the nonlinear regime. This transition is often called yielding, and has been the subject of numerous studies in the field[2]. Under flow, the materials usually stabilize in a steady state, in which the properties of the material are independent of time, but can be different from the properties at rest. In particular, for the case of concentrated soft colloids, it was found that shear can induce large changes in the microstructure, such as a local heterogeneity of the density and particle anisotropy[3]. After cessation of flow, the material relaxes back towards its resting state.

In this chapter, we study the yielding and the relaxation of concentrated solutions of dense stars through as systematic study of the stress relaxation after cessation of flow at different shear rates and concentrations, completed by stress-controlled experiments below and above the yield stress.

In a first part, we show that these experiments reveal a complex relaxation mechanism that can be described by two processes, similarly to what has been reported for microgels[4,5], comb polymers[6] and hard spheres[7]. The magnitude and the decay rate of the stress relaxation is closely linked to the shear characteristics, and in particular we find that the shear rate governs the decay rate of the stress relaxation.

In a second part, creep experiments are used in order to probe the yielding behavior below and above the yield stress. This technique offers some insight at the different relaxation processes happening in the star solutions, and emphasizes the significance of slowly decaying internal stresses,

Finally, a short third part shows the dramatic effect of the internal stress on the results of low-stress creep experiments and gives an attempt at quantifying its magnitude and timescale.

5.2 - Stress relaxation after cessation of flow

This part focuses on the stress relaxation of dense star solutions after the induction of flow at a constant shear rate. A lot of information can be obtained during the start-up flow experiments preceding the relaxation, which has been the main object of

Chapter 3. Here, we describe in details the stress decay of the star solutions following cessation of shear flow ($\dot{\gamma} = 0$) in this experiment. In practice, the shear rates decreases rapidly but not instantly, in about 50 to 100 ms (see chapter 2). We observe that the results strongly depend on the parameters of the start-up experiment, that we consider here as the pre-shear step. In particular, the value of the imposed shear rate seems to govern the timescale of the relaxation.

We compare the stress relaxation of star solutions at different concentrations from the melt (6c*) to 18 wt% (1.1 c*). At the lowest concentration of 1.1 c* (18 wt%), the crossover between G' and G" marking the transition from a liquid to a solid behavior happens at about 1 rad.s^{-1} in linear oscillatory shear (see Chapter 4). This means that this sample is able to relax at long times. The crossover between G' and G" rapidly shifts outside of the frequency window when the concentration is increased, such that already at 1.5c* (24 wt%), the relaxation frequency is too slow to be measured with common commercial shear rheometers. Macroscopically, this means that the sample does not relax over experimentally accessible timescales. This has a clear influence on the stress relaxation after cessation of flow. At the lowest concentration of 1.1c* (18 wt%), the stress in the material rapidly and completely relaxes. On the contrary, for concentrations above 1.5c* (24 wt%), the stress relaxation is much slower and in particular, it is not complete. Indeed, even after considerable relaxation times, the stress value is still significant compared to the initial stress. In this regime of concentration, we identified two modes in the stress relaxation, comparable to what was already observed in other systems[6,7] and especially microgels, in experiments and in simulations[4,5]. Qualitatively, at the end of the first fast relaxation process, the stress remains at a significant fraction of the initial stress, which then decays extremely slowly over time. A complete stress relaxation, if possible, might require between several hours and several days, depending on the pre-shear conditions. The relevant parameters for the description of the stress relaxation will be described in the following.

The shear rate was varied between 10^{-3} s^{-1} and 10 s^{-1}. The lower bound almost corresponds to the slowest shear rate possible with the instrument. The higher bound was chosen to avoid any fracture of the edge of the sample, or any flow instability that would affect the steady state during the shearing. At higher shear rates and at large final strains,

the sample was sometimes expelled from the gap during the experiment, which was immediately visible on the rheometer but also had a strong influence on the repeatability of the experiments. In particular, the values of the elastic and viscous moduli measured during the rejuvenation (see Chapter 2) were found to be very sensitive to any problems occurring during the high shear rates experiments.

All experiments were carried out until the same final strain of 15 strain units was reached, such that low shear rates experiments took several hours and the fastest just 1.5 seconds. As already described in Chapter 3, steady state was reached for all concentrations and we verified that the stress relaxation did not depend on the final strain at which the shearing stopped, as represented on Figure 5-1 for a shear rate of $0.02s^{-1}$. This threshold strain corresponds to the moment the stress reaches its steady state value, which is well within the nonlinear regime.

By stopping the experiments at different strains, we see that the shape of the stress relaxation curve changes from a single-mode to a double-mode relaxation. The data at the lower strain of 2%, in the linear regime, exhibit an almost constant stress even approximately one second after the cessation of the shear, and then decays slowly. After 100s, the residual stress is approximately 40% of the initial stress, showing that this material exhibits extremely slow elastic recoil. As the final strain is increased before the relaxation, we observe the gradual yielding of the material and the apparition of a fast relaxation mode followed by apparently the same slow relaxation mode (Figure 5-1). It is interesting to note that the slopes of stress vs time in this lin-log representation seem to be the same for the intermediate (10% and 20%) and high strains (100% and above), suggestive of a similar mechanism for the stress relaxation. This experiment was repeated at a shear rate of $0.2s^{-1}$ and the results are qualitatively similar (see Appendix A5-1). Due to the minimum response time of the instrument (of about 20 ms), it was difficult to measure the relaxation after a final strain of less than 20% in this case, which is already partly yielded. Although the observed behavior is qualitatively the same for both shear rates, the relaxation is much faster at higher shear rate, which leads to consider the shear rate as the main parameter describing stress relaxation processes.

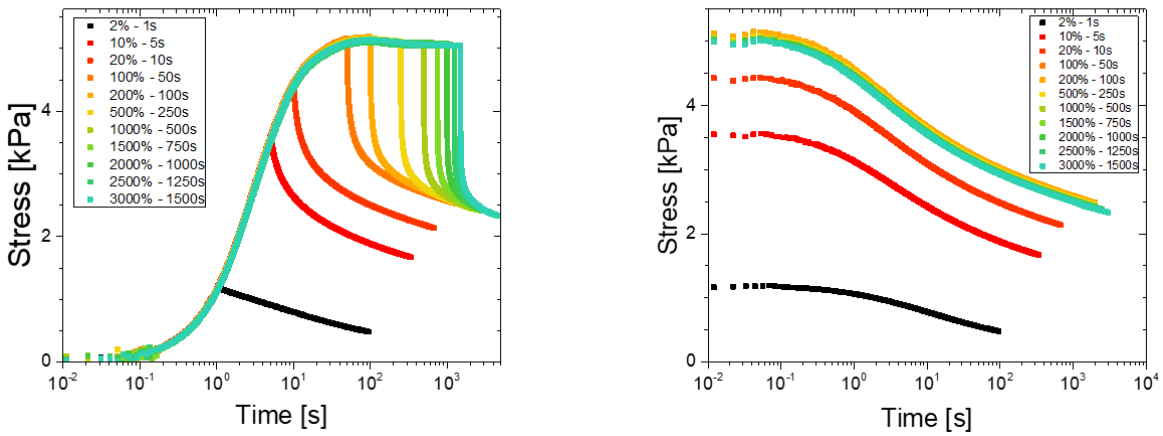

Figure 5-1. Left: Stress evolution during a start-up flow experiment and subsequent stress relaxation ($\dot{\gamma} = 0$) after different final strains before and after the yielding point. Right: Stress relaxation as a function of the time after flow cessation after different final strains ($\dot{\gamma} = 0.02s^{-1}$). The concentration is 3 c (50 wt%) and the yield stress is 4.8kPa.*

Figure 5-2 presents a typical series of stress relaxation curves after cessation of flow. The time origin is taken at the moment of flow cessation where the shear rate is immediately reduced from its imposed value to 0. In reality, the complete cessation of flow takes about 50 to 100ms due to the instrument inertia and lag time, therefore no reliable conclusions can be drawn from data faster than this timescale. This accuracy is sufficient in most of the cases studied here, but effectively puts an additional limitation into the investigation of the higher shear rates. Figure 5-2 shows that the relaxation process depends significantly on the pre-shearing conditions, and especially the value of the imposed shear rate. Although the conditions of the relaxation are the same in all cases ($\dot{\gamma} = 0$), the relaxation of stress becomes faster as the pre-shear rate is increased. The initial stress at the start of the relaxation increases with shear rate, since the steady state stress during the pre-shear follows the Herschel-Bulkley equation (see Chapter 4). At the lowest shear rates, this stress remains almost constant for nearly 10s after the cessation of flow, while it drops faster than the time resolution of the instrument (~20 ms) for the highest shear rates. Therefore, after a given time of stress relaxation, the remaining stress is lower if the pre-shear was carried out at a higher shear rate.

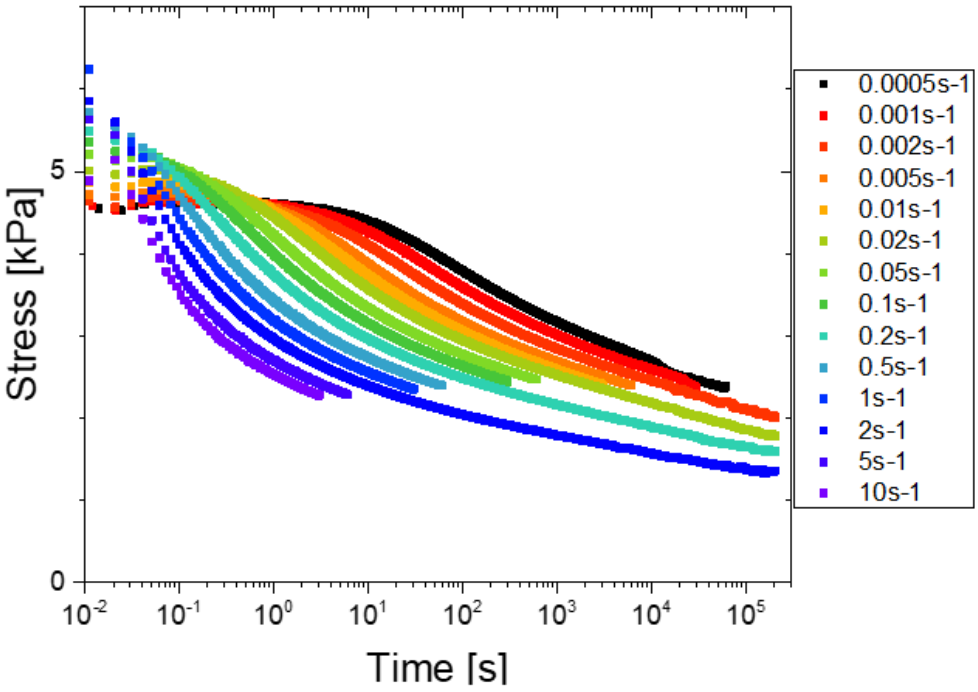

Figure 5-2. Representation of a typical series of stress relaxation after cessation of flow at different shear rates.

As observed before, the relaxation occurs through a two-step process. In microgel suspensions, which have proven to be very similar to these star solutions from a rheological point of view, the two-step process was explained as follows. First, the material solidifies. During this process, the velocity of recoiling particles was found to be ballistic, with a fast return of the number of neighbors to the equilibrium value. During shear, the average distribution of particles is anisotropic, with an accumulation of particles along the compression axis. Although this compresses the particles and allow them to flow, the material must return to an isotropic state after the cessation of shear. Since the particles are trapped in cages formed by their neighbors, this mechanism is very slow and was proposed to explain the second mode of the stress relaxation[4,5].

Interestingly, by scaling the stress relaxation time with the pre-shear rate and the respective relaxing stress with the steady state stress, the relaxation curves always start to decay at the same scaled time (Figure 5-3). This has been observed in most of the experiments conducted at different concentrations from the melt to the limit of the solid regime, with the exception of only a few (the long duration of the experiment makes them very susceptible to slight changes of the environment, in particular room temperature).

The characteristic time of the first relaxation process therefore seems to scale linearly with the inverse of the pre-shear rate. This is slightly different from what has been observed in computer simulations and experiments using microgels viewed as soft elastic spheres. In that case, the scaling for the short time relaxation was found to be $\tau \sim \dot{\gamma}^{-0.7}$ while here we found $\tau \sim \dot{\gamma}^{-1}$. This small albeit significant variation may be due to the different protocols used in the experiments. Here, we used a shear-rate controlled experiment, while the experiments and simulations on microgels were performed controlling the stress. We verified that in the case of stars, the 0.71 power law scaling yielded significantly worse results.

In some cases but not always, the stress seems to drop suddenly during the relaxation (see for example 2.7c*, 5.3c* or 6c* in Figure 5-3). This drop seems to occur very rarely, following different pre-shear rates and at different concentrations. It was also not reproducibly measured following the exact same experimental conditions, although this was not tested thoroughly. Based on this empirical evidence, we may argue that the stress drops during the relaxation due to an avalanche process. This is caused by the progressive accumulation of stress in a localized region of the sample, which can be suddenly released and trigger a chain reaction leading to the reorganization of a significant fraction of the sample and therefore the sudden decrease of the stress. This event generally cannot be detected at the macroscopic level and therefore appears random, and it was observed in hard sphere glasses during stress relaxation and creep[8]. This argument is also in direct agreement with the origin of the slow relaxation that reflects slow particle rearrangement (see the next paragraphs). In addition, the concept of avalanche flows mostly comes from flowing granular materials[9–11], which again is in good agreement with our idea of jamming.

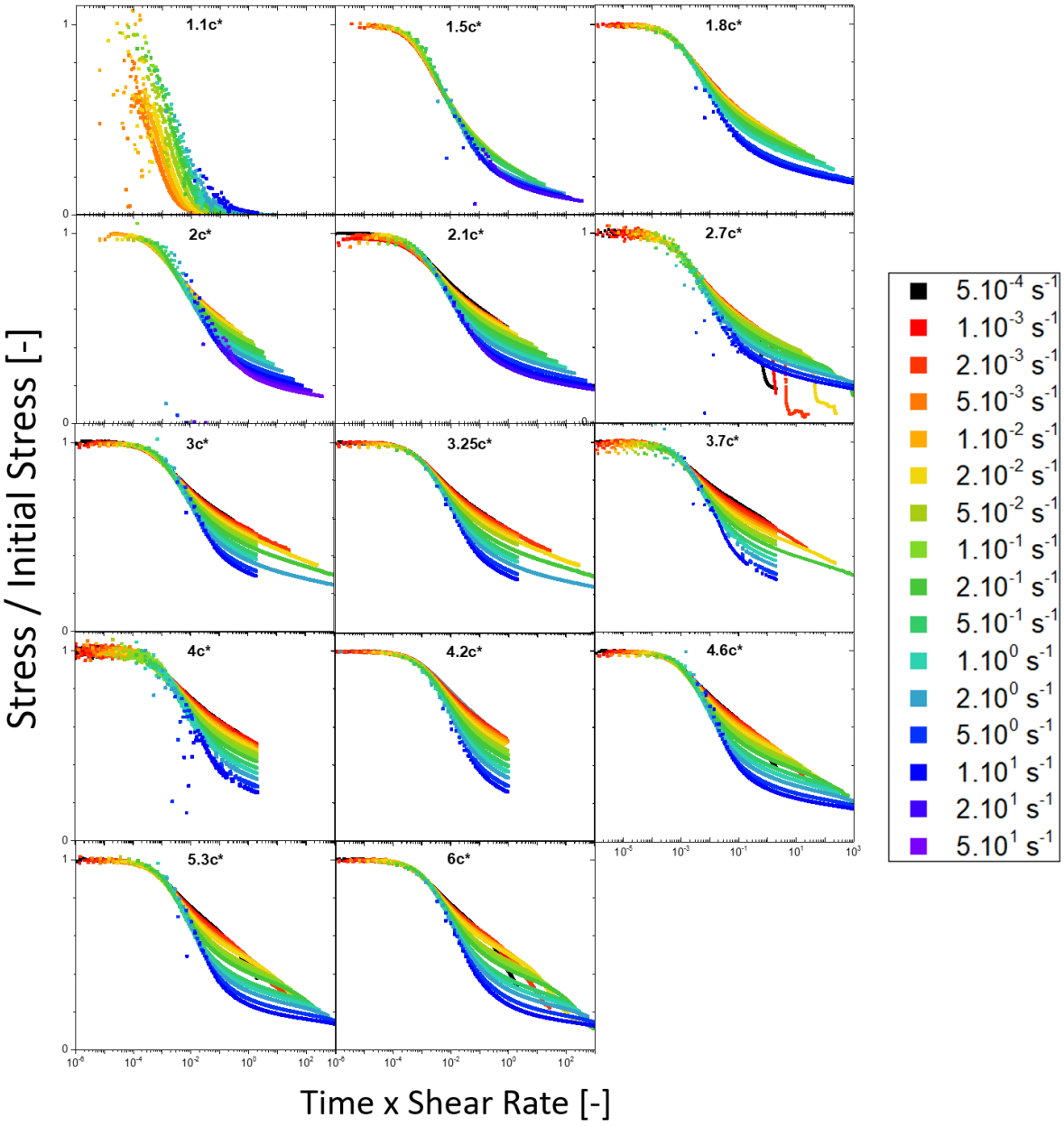

Figure 5-3. Evolution of the stress divided by the initial stress as a function of time normalized by the preshear rate for different shear rates and concentrations. The concentrations vary between the melt and the last solid sample and are given as a function of the overlap concentration c=16.6% wt.*

Additionally, the scaling proposed for microgels also includes a dependence of the relaxation time on the material elastic modulus G_0. In the case of stars, the elastic shear modulus at the minimum of G" was taken as the plateau modulus G_0, and effectively varies between 1 and 100kPa as function of concentration. Figure 5-4 represents the stress relaxation curves at two given shear rates of $0.01s^{-1}$ and $0.1s^{-1}$ for a wide range of concentrations. In this figure, the time was multiplied by the shear rate and the stress was

divided by the initial stress, as described above. The data shows that the relaxation is always very similar for all the concentrations expect the smallest two. At 1.8c* (30 wt%) and above, the stress relaxation is almost independent of the concentration, and therefore independent of the plateau modulus. The non-monotonic evolution of this family of curves suggests that the small variations of the stress relaxation may be attributed to small changes in the experimental conditions, such as loading conditions or room temperature.

Overall, we argue that the scaled stress relaxation above 1.8c* can be considered identical and independent of concentration. At 1.1c* (18 wt%), the linear viscoselastic data shows that the material can relax at timescales of the order of 1s (see Chapter 4), which translates here into a rapidly decreasing stress after the cessation of flow. An interesting case is the one of the 1.5c* (25 wt%) solution as discussed below. The same qualitative behavior as the higher concentrations is observed, but the remaining fraction of the stress after a given time following the cessation of flow is significantly lower than for all the other concentration. Judging by the shape of the curve, the initial scaled relaxation time does not seem to change drastically between the 1.5c* solution and the rest, but the magnitude of the relaxation seems to increase. Obviously, residual stresses cannot exist in a liquid sample with a short relaxation time, as displayed for instance for the 1.1c* solution here, and therefore the 1.5c* solution may exhibit a transition behavior between the liquid-like behavior at low concentrations and the solid behavior at 1.8c* and above.

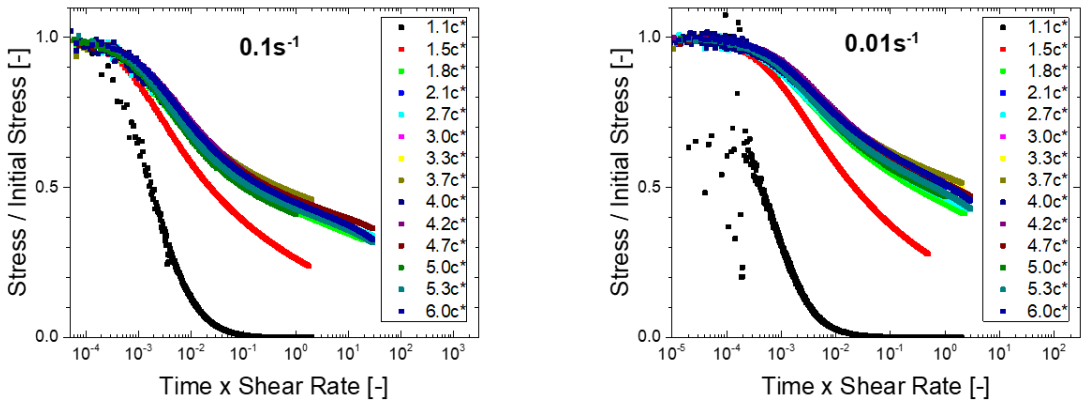

Figure 5-4. Stress divided by the initial stress as a function of time normalized by the preshear rate for a series of start solutions at different concentrations after a start-up flow

experiment with a constant shear rate of 0.1s^{-1} (left) and 0.01s^{-1} (right). The concentrations vary between the melt and the last solid sample and are given as a function of the overlap concentration c=16.6 wt%.*

The second relaxation process is much slower and happens after the fast relaxation described above. Remarkably, at the end of the first relaxation, the absolute value of the stress is almost constant for every shear rate at a given concentration. This can be observed in Figure 5-5 showing the stress relaxation against the scaled time, where all the stress curves seem to group up at the end of the first process. This slow process can be described as a logarithmic decay or a very weak power law, with a decay rate that seems to be independent of or only very weakly dependent on the pre-shear rate. For the lowest achievable pre-shear rates, the magnitude of the first relaxation process is very small and most of the stress relaxation occurs during the second process. Although no quantitative modelling could be developed to understand the stress relaxation, one can qualitatively describe it as follows:

The pre-shear stress is well described by a Herschel-Bulkley model such that the steady state stress at the end of the pre-shear process is a sum of two stress components, the yield stress σ_y and the stress coming from the flow $\sigma_f = k\dot{\gamma}^n$. We observed that the magnitude of the first process depends strongly on the shear rate, while the stress relaxation after the end of this process is very similar for all shear rates. Therefore, it is possible that the excess stress coming from the second term of the Herschel-Bulkley equation is related to the first process. Because it seems to come from the ability of the material to flow, the first fast process may be of viscous origin, while the second, much slower process comes from the elastic recovery of the material. Similarly to what was observed in microgels[4] and hard spheres[7] glasses, the first process describes the solidification of the material, in other words the transition from a yielded to a non-yielded behaviour, with a fast equilibration of the number of neighbors and reformation of the cages. After the first relaxation, the solid material still contains internal stresses that can only relax slowly due to the dense packing of the particles. These stresses originate from the local anisotropy of the centres of mass that have to diffuse back into a more favourable position.

While the slow elastic part of the relaxation is always present, it is possible to change the magnitude of the fast viscous process by applying an infinitely low shear rate. In practice, this is a tedious and long experiment, and a better way to approach this problem is by changing the type of experiments that we use. Indeed, instead of controlling the shear rate, it is possible to control the stress, in which case measurements below the yield stress are possible. This will be described in the following parts. Additionally, the fact that this material can retain stress during such a long time reflects a strong aging behaviour. The effect of aging are very limited on the linear viscoelastic behaviour, but it becomes very apparent in creep, and as mentioned in the last chapter, during the transient regime of start-up flow experiments.

In some cases but not always, the stress seems to drop suddenly during the relaxation (see for example 2.7c*, 5.3c* or 6c* in Figure 5-3). This drop seems to occur very rarely, following different pre-shear rates and at different concentrations. It was also not reproducibly measured following the exact same experimental conditions, although this was not tested thoroughly. Based on this empirical evidence, we may argue that the stress drops during the relaxation due to an avalanche process. This is caused by the progressive accumulation of stress in a localized region of the sample, which can be suddenly released and trigger a chain reaction leading to the reorganization of a significant fraction of the sample and therefore the sudden decrease of the stress. This event generally cannot be detected at the macroscopic level and therefore appears random, and it was observed in hard sphere glasses during stress relaxation and creep[8]. This argument is also in direct agreement with the origin of the slow relaxation that reflects slow particle rearrangement (see the next paragraphs). In addition, the concept of avalanche flows mostly comes from flowing granular materials[9–11], which again is in good agreement with our idea of jamming.

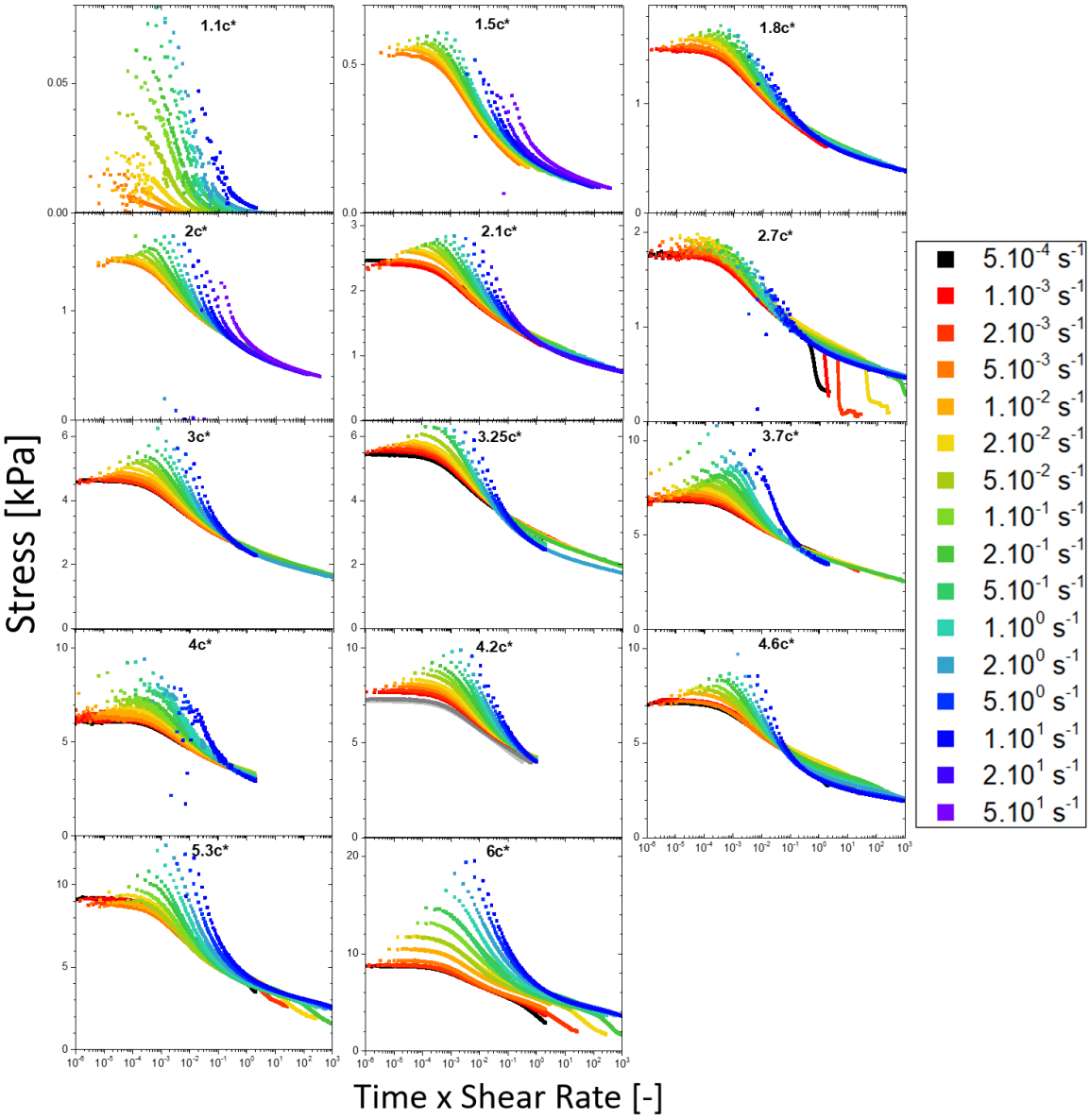

Figure 5-5. Evolution of the absolute stress as a function of time normalized by the pre-shear rate for different shear rates and concentrations. The concentrations vary between the melt and the last solid sample and are given as a function of the overlap concentration c=16.6 wt%.*

5.3 - Investigation of internal stresses through creep and stress relaxation

We performed a series of creep and start-up experiments with a 3c* (50 wt%) solution of high functionality stars 12805 (f=875, M_a=5.8kg.mol^{-1}). The steady state stress of start-up experiments at different shear rates yields a flow curve that can be fitted with

a Herschel-Bulkley model. This provides an estimation of the yield stress of the solution around 4.8kPa. Each experiment was preceded by the usual rejuvenation protocol, which is known to induce internal stresses in the material but has the merit to remove any prior shear history and puts the sample in a reproducible state at the start of each measurement. Unless stated otherwise, there was no waiting between the rejuvenation and the following experiment, such that internal stresses did not relax.

Figure 5-6 shows the evolution of strain during a series of creep experiments at different stresses below and above the yield stress. The creep was followed by a stress relaxation at constant strain (shear rate was set to zero). The results show that the shape of the creep curves changes so that the strain at very long time either increases slowly ($\dot{\gamma} \to 0$) below the yield stress or deviates ($\dot{\gamma} = constant$) above the yield stress[12,13]. This analysis provides a fairly similar result to the analysis of the flow curve, with an estimated yield stress around 4.5kPa.

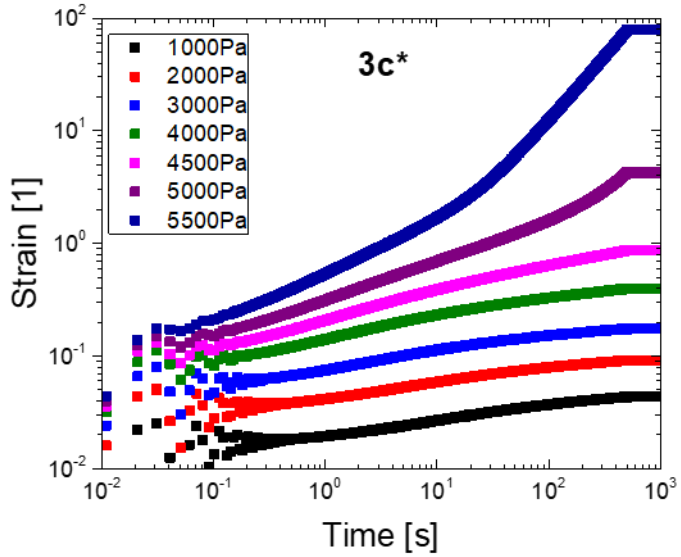

Figure 5-6. Evolution of the strain during creep experiments at various stresses below and above the yield stress for a 3c (50 wt%) star solution. The flat region at the end marks the start of the stress relaxation ($\dot{\gamma} = 0s^{-1}$). The scattering of the data at short times comes from the so-called ringing effect[14] and do not provide useful information in this context.*

Figure 5-7 shows the results of the same experiment in terms of stress evolution. During the creep, the stress is constant and decreases during the relaxation at constant strain. These results show a clear difference in the relaxation of the yielded compared to

the non-yielded state. Well below the yield stress, the stress relaxation appears extremely slow and significant fraction of the initial stress remains in the material after 500s. This observation confirms the decomposition of the stress relaxation into the two processes described above. The fast process seems connected to the flow of the material, which can only occur above the yield stress. The slow process describes the elastic recoil which is always present. The relaxations after the creep at the three lowest stresses are almost the same despite the stress being three times larger. When approaching the yield stress, there is a transition region where the relaxation is both faster and relaxes a greater part of the total stress within the first 500s, while for the two larger stress values, the relaxation shows a clear 2-mode process, as was observed for other concentrations and other systems[4–7]. This sweep across the yield stress shows that yielding appears as a gradual transition rather than a sharp one.

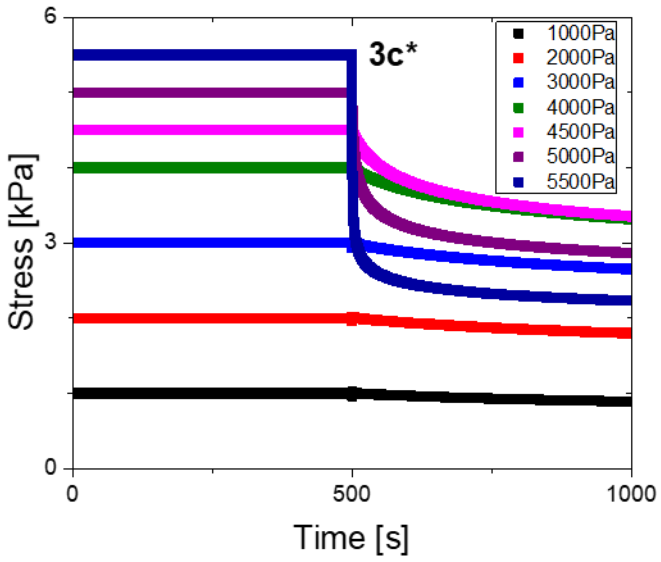

Figure 5-7. Evolution of the stress during creep and stress relaxation ($\dot{\gamma} = 0$) experiments at various stresses below and above the yield stress for a 3c (50 wt%) star solution.*

An analysis of the relaxation mechanisms can be done by plotting the remaining stress after 500s of relaxation as a function of the initial stress. Figure 5-8 shows there is a clear non-monotonicity in the value of the residual stress, that we can be explained with the two-step relaxation process. Below the yield stress, only the slow relaxation takes place as the material remains a solid during the experiment. Therefore, the stress relaxes

slowly, but has a small initial value and therefore the residual stress also remains small. The remaining fraction of the initial stress is however large, close to 90% after 500s. When the initial stress is increased above the yield stress, the fast relaxation mechanism appears due to the effective liquefaction of the sample as discussed above. This mechanism is fast, only acting when the material effectively behaves as a liquid, while the slow mechanism always take place. Therefore, the stress relaxes quickly but no completely during the fast process. This causes both the absolute stress and the relative stress to go down after 500s of relaxation in the yielded material. Importantly, this means that the relaxation is more efficient above the yield stress than just below, and the absolute value of stress after 500s of relaxation is indeed larger for an initial stress of 4kPa compared to 5kPa, which is *a priori* unexpected and showcases the complexity of the relaxation of yield stress materials.

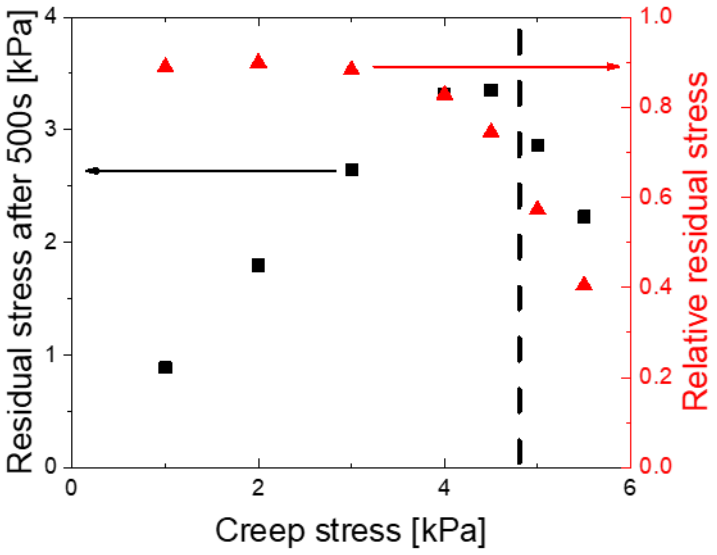

Figure 5-8. Left axis: Value of the remaining stress 500s after the start of the stress relaxation experiment ($\dot{\gamma} = 0$) as a function of the initial stress. Right axis: Value of the remaining stress divided by the initial stress 500s after the start of the stress relaxation experiment ($\dot{\gamma} = 0$). The dashed line represent the yield stress estimated from the Herschel-Bulkley fit of the flow curve. The black and red arrows indicate the correct axis.

To further demonstrate the importance of the internal stress on the material response, we performed creep experiments below the yield stress in the clockwise and anti-clockwise directions. The creep was always preceded by an oscillatory rejuvenation process in the non-linear regime (γ_0=100%, ω=1rad.s^{-1}, 60s), described in more details in

Chapter 2. The final strain at the end of the rejuvenation is given by $\gamma = \gamma_0 \sin(\omega t)$ with ω=1rad.s^{-1} and γ_0=100%. Therefore, after 60s of rejuvenation, we expect that the strain is $\gamma_f \approx -0.3$. Internal forces should therefore be "positive", meaning the elastic recoil of the sample pushes it to the "positive" (in this case, clockwise) direction.

To emphasize the reproducibility of the results, six tests are performed, alternatively in the positive and negative directions. The absolute value of the strain evolution is presented on Figure 5-9. In this representation, the values of strain obtained in the negative direction have been multiplied by -1 to facilitate the comparison. This clearly demonstrates that the strain increases more slowly in the negative direction than the positive, which we attribute to the pre-constrained state of the material at the start of the experiment. Since the positive residual stresses from the rejuvenation effectively act against the imposed negative stress in this case, the result is an effectively lower stress in the negative direction and therefore a weaker driving force for the deformation of the sample. This also translates into an effectively smaller shear rate during the creep, which in turn influences the stress relaxation, as is shown on Figure 5-9. The positive experiments reveal a faster relaxation because the shear rate during the creep is higher. There are a few remarks to be made about this result. First, these experiments were performed well below the yield stress and therefore only the slow mechanism should be at play during the relaxation. The relaxation rate of this mechanism thus also depends on the shear rate, which was already demonstrated in the first part of this chapter. Secondly, the shear rate values during the creep are extremely small, effectively there are below the detection limit (5.10^{-4} s^{-1}) of the instruments and are extremely noisy. The average shear rate can be determined from the final value of the strain divided by the time of the experiment, and in this case it is indeed higher for the positive experiments. However, the steady state during the creep and the following stress relaxation are extremely sensitive to the pre-shear history, and not only the average value of shear rate. In this case, the shear rate during creep remains small and smooth, ensuring the validity of the results.

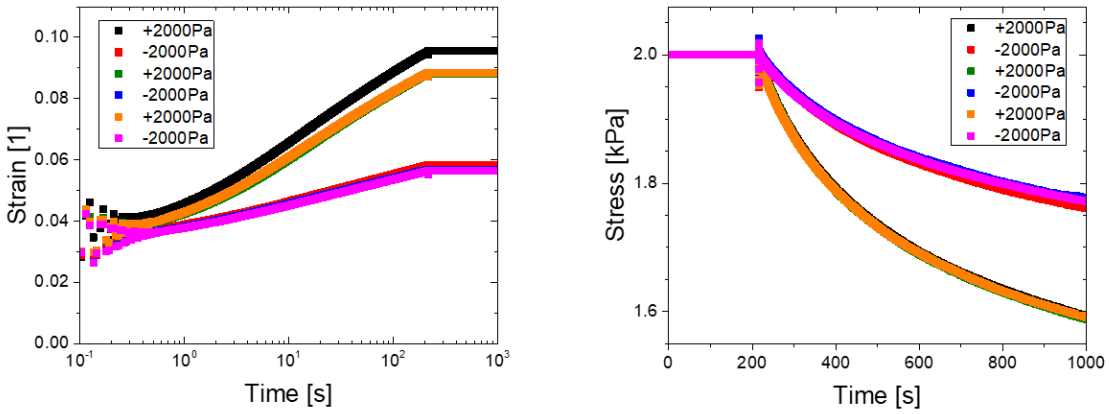

Figure 5-9.Left: Evolution of the strain as a function of time during a series of creep experiments in the clockwise (+2000Pa) and the counter-clockwise (-2000Pa) directions. Right: Comparison of the stress relaxation ($\dot{\gamma} = 0$) after the clockwise (+2000Pa) and the counterclockwise (-2000Pa) creep experiments. Results mostly superimpose such that only the last performed test is visible. We used the same star solution at a concentration of 3 c (50 wt%).*

We also present the evolution of the strain and the stress relaxation after different durations of rejuvenation, which effectively place the sample in different initial strain positions. Figure 5-10 shows the strain at the end of the creep as a function of the initial strain position, which can be changed by varying the duration of the rejuvenation protocol (18s, 36s, 60s and 76s). It also displays on the right axis the stress at the end of the 1000s stress relaxation, which has proven to be extremely sensitive to pre-shear history. The results show that the magnitude of the internal stress increases the further away from the zero position we start, and also that its direction is opposite to the direction of the final oscillation. In other words, the internal stress always pushes towards the zero position with a magnitude that depends on the distance from this zero position. Consequently, the shear rate is the highest when the imposed stress and the internal stress push in the same direction, with a starting position far from the zero position. Thus, the stress relaxation is also faster, since it depends on the shear rate, whereas the resulting stress at any point during the relaxation is smaller. The point corresponding to the shortest rejuvenation of 18s (initial strain of -0.75) does not comply with this scaling. The reproducibility and accuracy of the other results being extremely good, we attribute this difference to the fact that a rejuvenation of 18s was probably not enough to erase

completely the prior shear history, that may have an influence on this particular experiment.

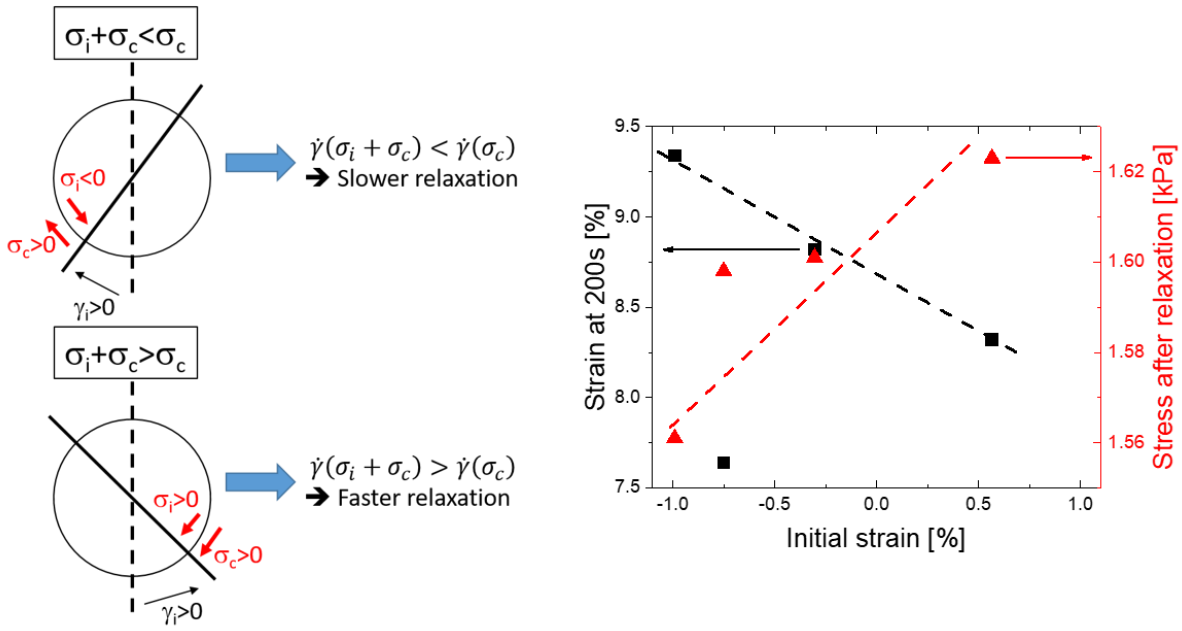

Figure 5-10. Left: Schematic explanation of the effective addition of the internal stress (σ_i) and creep stress (σ_c) in the case of positive (top) or negative (bottom) final strain after the rejuvenation. Right: Left axis: Measured strain after the creep experiment as a function of the initial strain induced by the rejuvenation. Right axis: Absolute value of the stress 1000s after the start of the stress relaxation ($\dot{\gamma} = 0$) following the creep experiments. The red and black arrows indicate the corresponding axis.

Lastly, another point of interest for the study of the internal stresses and stress relaxation is to assess the validity of the creep experiments compared to start-up flow experiments. Below the yield stress, only creep experiments are able to reliably probe the properties of the sample, since even the smallest possible shear rate should impose into at least the yield stress value, according to the Herschel-Bulkley model: $\sigma = \sigma_y + k\dot{\gamma}^n$. Above the yield stress however, one can use either creep or start-up experiments. In theory, there should be a perfect agreement between the two techniques, since a given stress is associated to a given shear rate through the Herschel-Bulkley equation. In practice however, it was observed that this is not always the case.

To illustrate this phenomenon, we first measured the steady state stress of the same solution described above at a constant shear rate of $0.2s^{-1}$. The value of 5.57kPa was reproducibly obtained and robust. Subsequently, we performed a creep at this exact stress value of 5.57kPa, above the yield stress by definition, and Figure 5-11 shows that,

even though the steady state stress is indeed the same, the shear rate during the creep experiment is always higher than $0.2s^{-1}$ and expectedly, this causes the stress relaxation to be faster. In particular, the shear rate at the start of the creep experiment can reach higher values of the order of $1s^{-1}$. However, when the stress is progressively increased from 0 to the desired value using a 5s stress ramp, this regime of high shear rates can be avoided and the shear rate remains fairly low and close to the expected value of $0.2s^{-1}$ during the experiment. This translates into an almost identical stress relaxation, since the shear history conditions became very similar. This simple test illustrates once again that the stress relaxation of this material depends very much on its shear history and seems to be ultimately governed by the shear rate. Additionally, this shows that the shear rate overshoot at the start clearly modifies the steady state that can be reached. Although more precise measurements should be carried out, we expect that the microstructure under shear strongly depends on shear history, and therefore a previously yielded material may exhibit less resistance to shear, hence causing a higher steady state shear rate in the creep experiment.

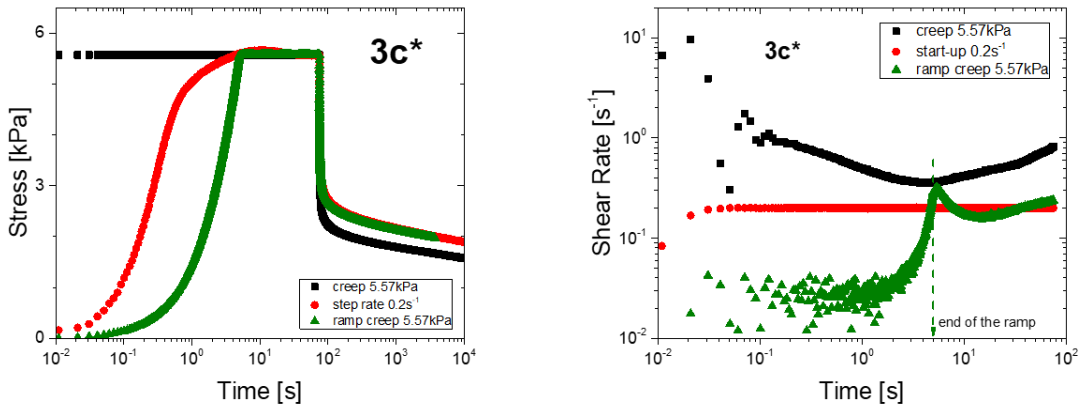

Figure 5-11. Left: Stress evolution during the creep or start-up flow experiments followed by stress relaxation ($\dot{\gamma} = 0$). Right: Representation of the shear rate during the creep or the start-up flow experiments. The concentration is 50% wt.

To conclude, we have demonstrated in this part that the slow part of the stress relaxation is present in both the yielded and non-yielded state of the material. This is in agreement with the proposed explanation for its origin described in the first part, namely the slow return to an isotropic position of the particles after the disruption caused by the

flow. Since the relaxation can take up to several hours, this internal stress has a significant effect on the results of the following experiments, for example in the present case of low-stress creep experiments. In addition, the relaxation of the internal stress is mainly governed by the pre-shear rate, which makes the material very sensitive to the shear history.

5.4 - Quantification of internal stresses using low-stress creep experiments

Although the linear viscoelastic behavior of the studied star melts and solutions is virtually unaffected by ageing, it has a clear influence on the nonlinear shear properties, such as the development of a stress overshoot in start-up experiments. Additionally, internal stresses are also a reason why creep experiments are technically difficult to reliably perform with this material. Since the material retains some of its shear history for extended periods of time, the starting point of any experiment is rarely equilibrium, and therefore the results may depend on the waiting time. The creep results, usually in the form of the creep compliance J(t), can be transformed through a series of mathematical operations[15–17] into the frequency dependent G'(ω) and G"(ω), which describe the linear regime. Therefore, if one wants to use the inversion of creep data to investigate the long time linear behavior, the creep stresses should remain low enough in order to not perturb the material too quickly, so that it stays at all experimental times close to its resting (quasi-equilibrium) state. This is somehow comparable to the quasi-equilibrium conditions sometimes used in thermodynamics, stating that even though the initial and final states may be very different, the system evolves slowly through a series of quasi-equilibrium states and therefore it can be treated as such. This is obviously an approximation, but one that may provide a good representation of the actual process if each transformation is indeed slow enough. To apply this approximation to creep experiments, the use of very small stresses is required, typically less than 1% of the elastic modulus. As a consequence, the imposed stress might become of the order of the internal stress in the material, which is the case for the samples studied here.

This superposition of internal and imposed stresses leads to a large error in the calculation of the creep compliance (Figure 5-12), and therefore prevents the conversion

of the creep data into long-time linear viscoelastic data. One solution to this problem is obviously to wait until all the internal stress has decayed, which can take up to several days in some cases. Beyond the obvious experimental tediousness of such a protocol, one may always wonder whether the internal stresses are effectively relaxed after a given time.

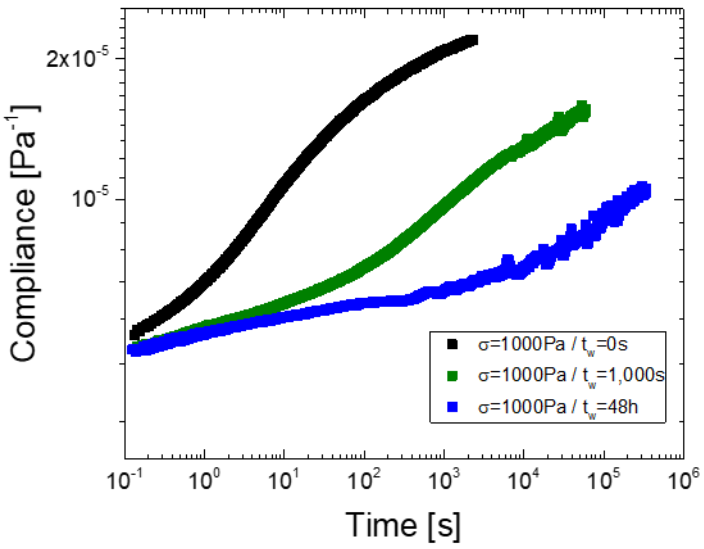

Figure 5-12. Typical creep compliance calculated during a creep experiment at low stress for different values of the waiting time t_w between the rejuvenation and the creep. The sample used here is a high functionality star (f=929, M_a=4.0 kg.mol^{-1}) in the melt state.

The effect of internal stresses on the creep behavior of a dense star melt with f=929 and M_a=4.0kg.mol^{-1} is demonstrated in Figure 5-13. It shows the measured compliance during a creep at very low stress, after two different rejuvenation protocols. As already mentioned above, an oscillatory rejuvenation at a frequency of 1rad.s^{-1} during 60s will end in a negative strain compared to its starting reference point, as sin(60)=-0.30. Therefore, we expect that residual stress from the rejuvenation pushes the material into the positive direction. On the contrary, the same rejuvenation lasting 64s ends in a positive deformation, since sin(64)=+0.92. Therefore in this case, the residual stress pushes the material in the negative direction. When an insignificant stress of 1Pa is applied during the creep, the residual stress is much bigger than the imposed stress and therefore the material moves in the direction of the residual stress. When a higher creep

stress of 1000Pa is imposed, there are two possibilities. Either both the imposed and the residual stresses push in the same direction and there magnitudes add up, resulting in a stronger deformation of the sample; or they push in opposite directions and the stronger stress decides the direction of the deformation. Since the residual stress decays with time, at long times the imposed stress is always larger and therefore the material eventually moves in the positive direction. Thus, an S-shaped curve (see blue curve on Figure 5-13) is obtained when the two stresses add up, since the effective total stress decays to a non-zero value over time; or the strain has a non-monotonic behavior when the two stresses push in opposite directions, with the internal stress being the largest of the two at first, but the imposed stress becoming predominant at long times. This peculiar behavior also provides an approximation of the intensity and timescale of the internal stress. Here, judging by the non-monotonicity of the orange curve, the internal stress seems to have an effect for about 5,000s and is magnitude is comparable but bigger than 1kPa.

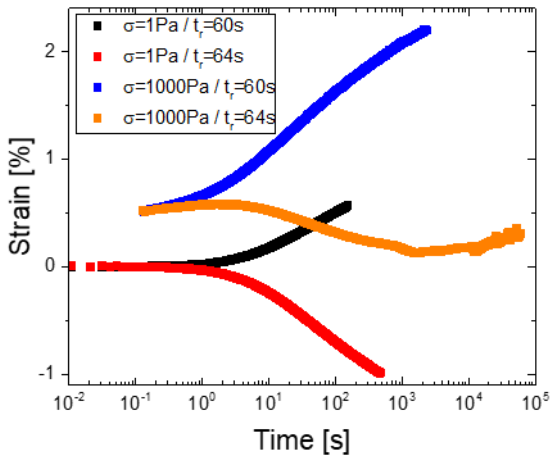

Figure 5-13. Evolution of the strain during a series of creep experiments at different creep stresses and different rejuvenation times t_r. The different rejuvenation times change the initial strain and thus induce either a positive (t_r=60s) or a negative (t_r=64) internal stress. The sample consists of a dense star (f=929, M_a=4.0 kg.mol^{-1}) in the melt state.

In this part we have demonstrated that the presence of slowly decaying internal stresses are enough to macroscopically affect the sample rheological behavior. They are responsible for the apparent aging of the material, meaning that time becomes an important factor in the reproducibility and the analysis of the data, especially for non-linear experiments. Finally, we have tried to quantify both the magnitude and the time

scale of the internal stress in a melt of a dense star with f=929 and M_a=4.0 kg.mol^{-1}, which will be developed more extensively in Appendix 5-2.

Conclusions

The stress relaxation of concentrated star suspensions exhibits an extremely rich behavior. It can be decomposed into two processes, a fast viscous process and a slow elastic process. This decomposition was already proposed for various colloidal and polymeric systems[3–7]. The proposed physical rationalization of these two mechanisms is first, a fast relaxation of the cages (centers of mass and numbers of neighbors), followed by a slower relaxation of the particle anisotropy induced by shear. This explanation may be equally applied to star solutions, although there are some quantitative differences. For example, the characteristic decay rate of the fast relaxation seems to scale linearly with the imposed pre-shear rate, while another slower scaling was proposed for the microgels. The possibility to investigate the behavior of the material below its yield stress with creep experiments opens a way to separate the influence of the fast and the slow relaxation processes, since it appears that the relaxation of stress below the yield stress is done almost exclusively through the slow process. This process is responsible for the accumulation of internal stresses inside the material, coming directly from the flow history, which can have a significant influence on the nonlinear properties several hours after the end of the shear. Therefore, the understanding of internal stresses and their relaxation is important for the analysis and the reproducibility of the results. In the case of star solutions, we demonstrated that very long waiting times of the order of several hours are necessary to get rid of any effect of the internal stress, which is a direct consequence of the extremely long terminal time observed in the linear regime. As such, we may consider these dense star polymer melts and solutions as effectively jammed, similarly to what was observed for microgels[18].

Appendices

A5-1. Stress relaxation after an increasing total strain at 0.2s^{-1}

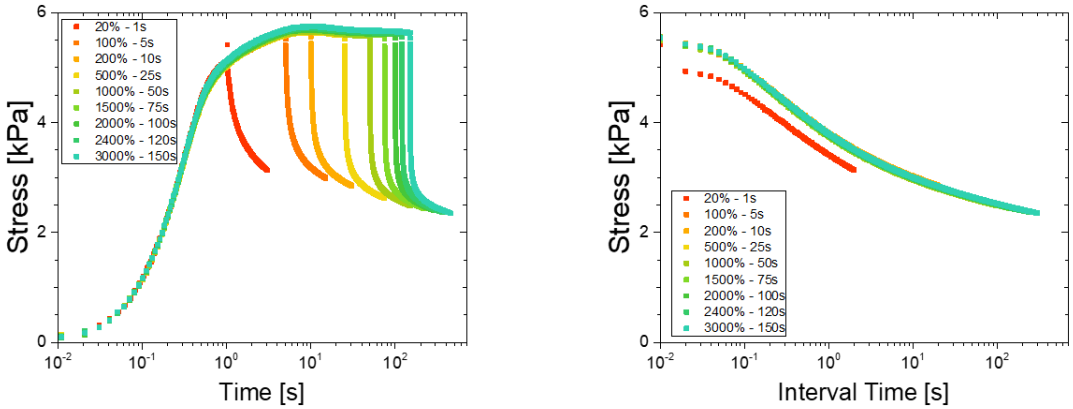

Figure A5-1. Left: Stress evolution during a start-up flow experiment and subsequent stress relaxation ($\dot{\gamma} = 0$) after different final strain before and after the yielding point. Right: Stress relaxation as a function of the time after flow cessation after different final strains ($\dot{\gamma} = 0.2s^{-1}$). See text and Figure 5-2 for more details.

A5-2. Estimation of the internal stresses from creep experiments.

In the following we used a star with f=875 and M_a=5.8kg.mol^{-1}, this time in a 1.8c* (30 wt%) solution. We performed similar creep experiments at very low creep stress and could again observe a strong time dependence due to the slow relaxation of the internal stress. There is an apparent opposition between the rheological behaviors observed in creep and in oscillatory shear. In the linear regime, oscillatory shear at any given aging time and any frequency shows that this material clearly has dominant elastic properties over viscous ones, with G'>>G". However, the fact that we observe a significant increase or decrease of the strain after rejuvenation shows that the internal stress is able to make the material flow, although it is much smaller than the yield stress. This may come from the fact that the material is "pre-yielded", meaning that its microstructure might still be affected by the shear history and therefore is able to flow under a much smaller stress.

Going further into the analysis of these ambiguous results, we may consider the material not like a solid but like a very viscous liquid, which stored elastic energy during the rejuvenation but can only elastically recoil back slowly due to its very high viscosity. In other words, we can consider this sample as a very viscous liquid trying to flow, pushed by its internal stress. In a viscous liquid, the stress becomes proportional not to the strain,

as would be the case for a solid, but to the shear rate. Therefore, we can estimate the shear rate during the creep, which is the time derivative of the strain, and thus calculate the stress needed to push such a material at such a shear rate. Figure A5-2 shows the results obtained for the star solution at 1.8c* (30 wt%). The viscosity is estimated from the complex viscosity at the corresponding shear rate: $\dot{\gamma} \approx \gamma_0 \omega$, where $\dot{\gamma}$ is the shear rate, γ_0 is the strain at which the oscillatory measurement is performed and ω is its angular frequency.

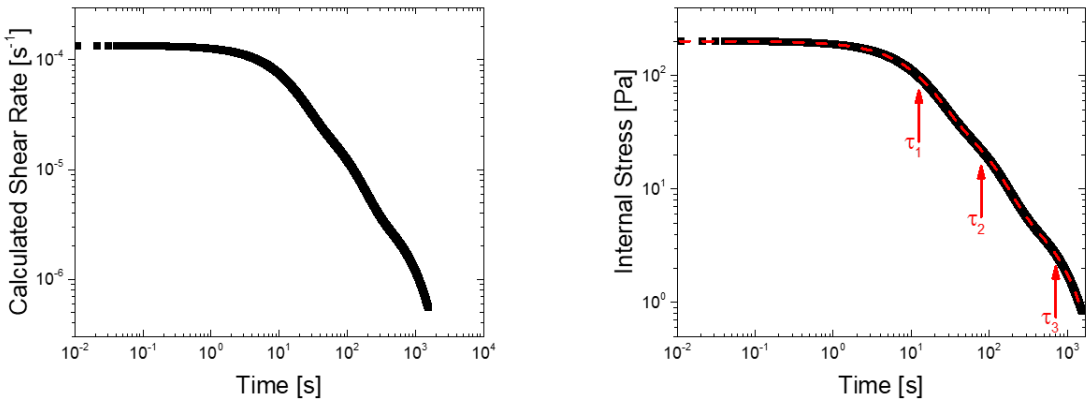

Figure A5-2. Left: Calculated shear rate from the temporal derivative of the strain measured during creep experiments. Right: Calculated internal stress using the method described in the text. Red arrows point towards the values of the three characteristic times of the decay. The sample is a 1.8 c (30 wt%) solution of a dense star with f=875 and M_a=5.8 kg.mol^{-1}.*

The resulting estimation of the internal stress expectedly decays with time and can be well modelled by a two-step exponential decay in this case. Its maximum value is around 300Pa, which is somewhat larger than anticipated, but decays quickly through a first process. The longest relaxation time is about τ=700s, which means that most of the influence of the internal stress should disappear after $5\tau \approx 3500s$, which is close to what was observed experimentally. Although more evidence is needed to confirm it, this time matches the timescale of the overshoot growth during start-up experiments at a comparable concentration, suggesting a possible link between the two phenomena.

References

(1) Gury, L.; Gauthier, M.; Cloitre, M.; Vlassopoulos, D. Colloidal Jamming in Multiarm Star Polymer Melts. *Macromol.* **2019**, *52* (12), 4617–4623. https://doi.org/10.1021/acs.macromol.9b00674.
(2) Bonn, D.; Denn, M. M.; Berthier, L.; Divoux, T.; Manneville, S. Yield Stress Materials in Soft Condensed Matter. *Reviews of Modern Physics* **2017**, *89* (3). https://doi.org/10.1103/RevModPhys.89.035005.
(3) Seth, J. R.; Mohan, L.; Locatelli-Champagne, C.; Cloitre, M.; Bonnecaze, R. T. A Micromechanical Model to Predict the Flow of Soft Particle Glasses. *Nat. Mater* **2011**, *10* (11), 838–843. https://doi.org/10.1038/nmat3119.
(4) Mohan, L.; Cloitre, M.; Bonnecaze, R. T. Build-up and Two-Step Relaxation of Internal Stress in Jammed Suspensions. *Journal of Rheology* **2015**, *59* (1), 63–84. https://doi.org/10.1122/1.4901750.
(5) Mohan, L.; Bonnecaze, R. T.; Cloitre, M. Microscopic Origin of Internal Stresses in Jammed Soft Particle Suspensions. *Physical Review Letters* **2013**, *111* (26). https://doi.org/10.1103/PhysRevLett.111.268301.
(6) Snijkers, F.; Vlassopoulos, D.; Lee, H.; Yang, J.; Chang, T.; Driva, P.; Hadjichristidis, N. Start-up and Relaxation of Well-Characterized Comb Polymers in Simple Shear. *J. Rheol.* **2013**, *57* (4), 1079–1100. https://doi.org/10.1122/1.4804198.
(7) Ballauff, M.; Brader, J. M.; Egelhaaf, S. U.; Fuchs, M.; Horbach, J.; Koumakis, N.; Krüger, M.; Laurati, M.; Mutch, K. J.; Petekidis, G.; et al. Residual Stresses in Glasses. *Phys. Rev. Lett.* **2013**, *110* (21). https://doi.org/10.1103/PhysRevLett.110.215701.
(8) Jacob, A. R.; Moghimi, E.; Petekidis, G. Rheological Signatures of Aging in Hard Sphere Colloidal Glasses. *Physics of Fluids* **2019**, *31* (8), 087103. https://doi.org/10.1063/1.5113500.
(9) Börzsönyi, T.; Halsey, T. C.; Ecke, R. E. Two Scenarios for Avalanche Dynamics in Inclined Granular Layers. *Physical Review Letters* **2005**, *94* (20). https://doi.org/10.1103/PhysRevLett.94.208001.
(10) Courrech du Pont, S.; Gondret, P.; Perrin, B.; Rabaud, M. Granular Avalanches in Fluids. *Physical Review Letters* **2003**, *90* (4). https://doi.org/10.1103/PhysRevLett.90.044301.
(11) Tegzes, P.; Vicsek, T.; Schiffer, P. Avalanche Dynamics in Wet Granular Materials. *Physical Review Letters* **2002**, *89* (9). https://doi.org/10.1103/PhysRevLett.89.094301.
(12) Da Cruz, F.; Chevoir, F.; Bonn, D.; Coussot, P. Viscosity Bifurcation in Granular Materials, Foams, and Emulsions. *Physical Review E* **2002**, *66* (5). https://doi.org/10.1103/PhysRevE.66.051305.
(13) Cloitre, M.; Borrega, R.; Leibler, L. Rheological Aging and Rejuvenation in Microgel Pastes. *Phys. Rev. Lett.* **2000**, *85* (22), 4819–4822. https://doi.org/10.1103/PhysRevLett.85.4819.
(14) Kim, M.; Bae, J.-E.; Kang, N.; Soo Cho, K. Extraction of Viscoelastic Functions from Creep Data with Ringing. *J. Rheol.* **2015**, *59* (1), 237–252. https://doi.org/10.1122/1.4904394.
(15) Vyas, B. M.; Orpe, A. V.; Kaushal, M.; Joshi, Y. M. Passive Microrheology in the Effective Time Domain: Analyzing Time Dependent Colloidal Dispersions. *Soft Matter* **2016**, *12* (39), 8167–8176. https://doi.org/10.1039/C6SM00829A.

(16) Kwon, M. K.; Lee, S. H.; Lee, S. G.; Cho, K. S. Direct Conversion of Creep Data to Dynamic Moduli. *J. Rheol.* **2016**, *60* (6), 1181–1197. https://doi.org/10.1122/1.4961484.
(17) Evans, R. M. L.; Tassieri, M.; Auhl, D.; Waigh, T. A. Direct Conversion of Rheological Compliance Measurements into Storage and Loss Moduli. *Phys. Rev. E* **2009**, *80* (1), 012501. https://doi.org/10.1103/PhysRevE.80.012501.
(18) Pellet, C.; Cloitre, M. The Glass and Jamming Transitions of Soft Polyelectrolyte Microgel Suspensions. *Soft Matter* **2016**, *12* (16), 3710–3720. https://doi.org/10.1039/C5SM03001C.

Chapter 6: Interactions in dilute suspensions of grafted nanoparticles

Abstract

The dynamic properties of a colloids are mainly dictated by the microstructure of the particles it is made of. For soft particles, these properties are a complex function of different parameters. In particular for polymer-grafted nanoparticles, the grafting density and the corona size seem to be the two most significant components. The effect of these two parameters on the interactions between polymer-grafted nanoparticles is studied here. We use light scattering to determine the second virial coefficient (A_2) and a simple 3-component model to calculate the expected interaction potentials for each nanoparticle, from which a theoretical value of A_2 is also derived. Experimental and theoretical results are compared.

6.1 – Introduction

Grafted nanoparticles are made of a solid core covered in polymer chains, tethered to the surface of the core by either physical or covalent bonds, the latter being the case here. The core is usually composed of an inorganic material like silica[1–3], titania[4] or different metal or metal alloys[5] and can be spherical or anisotropic[6], such as ellipsoidal, rod-shaped, flat, or even more complex. The sub-micron size of the grafted particles makes them prone to Brownian motion, so that they can be stable in suspension in a medium by balancing gravity forces. Due to their size, they are also very sensitive to microscopic forces such as electrostatic, depletion or Van der Waals interactions. The interplay between the attractive forces and the thermal noise governs the stability of the suspension. If attractions are too strong, the particles aggregate, and at a certain concentration range (depending on the range of attraction) they can form gels[7–9]. If the interactions between particles are repulsive, the suspensions are stable. With increasing concentration, the particles can form colloidal crystals[10–13] and (metastable) glasses[10,11,14–17], or liquid crystalline phases[18–21] if they are anisotropic.

Since grafted nanoparticles are by nature hybrid materials, there are several ways one can act on the microstructure to influence the material properties. The most fundamental one is the choice of material and suspending medium (good/bad solvent conditions). While various materials can be used, the most common core material is silica, which is an inexpensive, relatively safe and abundant material. The polymer constituting the shell of the particles is selected based on the desired properties and applications of the material. Current synthesis methods offer a broad range of ways of grafting hydrophilic (polyethylene oxide[22,23], polypropylene oxide[24,25], polymethyl methacrylate[26–28] …) or hydrophobic (polystyrene[29–31], polyisoprene[32,33], polybutadiene[34,35] …) polymers. Some polymers such as poly-N-isopropylacrylamide[36] (PNIPAM) or poly(2-(dimethylamino)ethyl methacrylate)[37,37,38] (PDMAEMA) can change their interactions with the suspending medium in response to an external stimulus such as pH or temperature[39,40]. The grafting of such polymers onto nanoparticles allows for the design of responsive materials that can alter their properties at will through a good control of the suspending medium, or can act as nanometer-sized sensors to probe the local properties of the medium around them.

Even without such specific interactions, polymeric shells will swell in the presence of a good solvent, introducing softness into the particles. This means that their interactions become more complex than the so-called hard-sphere potential, which does not allow for ranged interactions or particle interpenetration. These soft interactions can be tuned by changing the microstructure of the particles, mainly through two parameters: grafting density (σ) and chain degree of polymerization (DP)[41,42]. Particles with longer, sparser chains are expected to exhibit softer behavior, which is characterized by a smoother pair correlation function (broader , fewer peaks) and more random ordering compared what is observed for hard spheres[43–46].

The characterization of the interactions of soft nanoparticles is therefore essential for their understanding, tailoring and extending their applications. These interactions are a direct consequence of their chemistry and microstructure, thus the microstructure directly controls the material properties. A good understanding of the significant parameters influencing these properties is thus needed to design new, more efficient materials. In this chapter, we measure and model the interactions of several well-

characterized model polymer-grafted nanoparticles in the dilute regime by means of light-scattering. First, we characterize the size of the particles both with static and dynamic light scattering. Then, we determine the apparent second virial coefficient, which reflects the particle interactions. Finally, we use a simple model to estimate the theoretical value of the second virial coefficient and conclude on the validity of this model.

Details about the light scattering techniques and the microstructure of the particles are given in chapter 2. We used two sets of polymer-grafted nanoparticles. In the first set, the particles have a polystyrene corona of varying length and grafting density, grafted onto a silica core. The second set consists of two PMMA-grafted silica particles in which the chain length and the solvent is varied. Part of the data presented here were collected and analyzed by P. Bogri[47] and S. Kamble[48].

6.2 – Dynamic light-scattering

The hydrodynamic radius of each sample was measured in the dilute regime using dynamic light scattering as described in chapter 2. Since the cores of the particles are almost the same for each sample, it is expected that the total size of the particles depends on the grafting density, the chain length and, of course, the solvent quality. Ohno et al.[42] described a model with two regimes that depend on the monomer density in the brush. Based on scaling arguments, they derived the cut-off size (Equation 1) between the concentrated polymer brush (CPB) for $r<r_c$ and the semi-dilute polymer brush (SDPB) for $r>r_c$.

$$r_c = r_0 \sigma_0^{1/2} \upsilon_0^{-1} \qquad \text{(Equation 1)}$$

where, r_c is the critical cut-off size between the two regimes, r_0 is the hard core radius, σ_0 is the normalized grafting density ($\sigma_0 = \sigma l^2$), υ_0 is the normalized excluded volume parameter ($\upsilon_0 = \sqrt{4\pi}\upsilon$) that depends on solvent quality and l is the Kuhn monomer length.

Qualitatively, three regimes can appear: the chains are in the CPB regime (for high grafting densities and/or small cores); the chains are in the SDPB (for low grafting densities and/or large cores); or there is a transition inside the brush from CPB to SDPB. The size of the particles measured in this study are reported in Figure 6-1 alongside different models

discussed below. The minimum size in the collapsed state and the maximum size at full swelling (maximum extension of the grafted chains) are also reported on the figure to appreciate the degree of stretching of the chains.

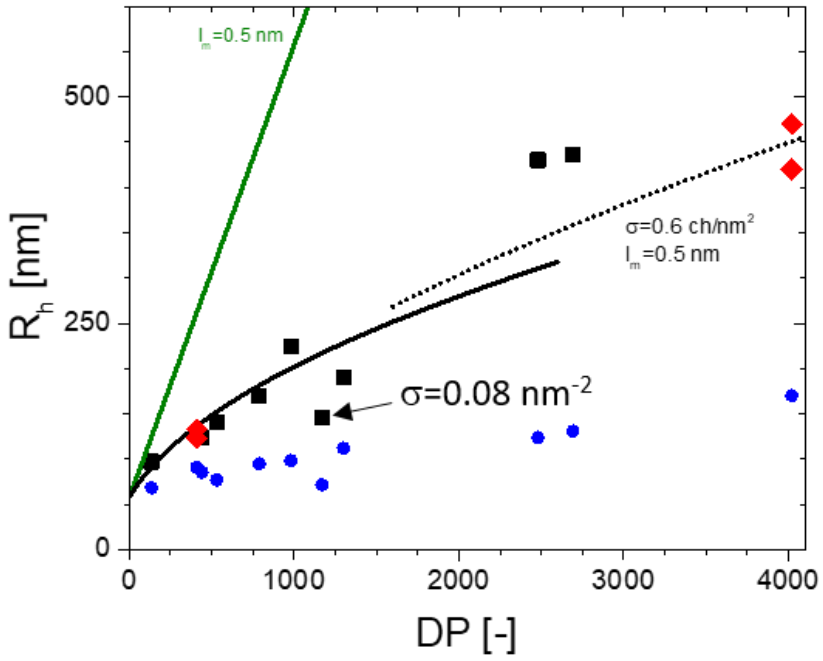

Figure 6-1.Hyrodynamic radius as a function of the degree of polymerization. Black squares represent the Si-PS particles and the red squares represent the Si-PMMA particles. The blue squares are the calculated values of the collapsed size based on the density of PS (1.06 kg.l^{-1}) and PMMA (1.18 kg.l^{-1}). The green line represents the size at the maximum extension of the grafted chains (with Kuhn monomer size of 0.5 nm). The continuous (respectively dotted) black line is the CPB (respectively SDPB) model prediction of Ohno et al.[42] for a grafting density of 0.6 nm^{-2} and monomer length of 0.5 nm.

There is a good agreement with the CPB model for particles with grafting densities close to 0.6nm^{-2} and moderate chain length (DP<1500 monomers). The particles with the longest chains (DP>2000 monomers) seem to fall closer to the SDPB model. Since the CPB line is calculated for a grafting density of 0.6 nm^{-2}, the data from the sample with lower grafting density (σ=0.08 nm^{-2}) fall below the prediction of the CPB model, outlining the role of the grafting density on the stretching of the chains.

6.2 – Static light scattering

Using static light scattering the form factors of the particles were measured. The scattered intensity was normalized and fitted using the "Scatter" software[49] (Figure 6-2). We used the "core and inhomogeneous shell" model provided by the software to represent the hard silica core and the solvent-swollen shell of the particles. The monomer density in the shell was modelled as a power law with exponent $-4/3$ [50]. The other parameters were left free and in this way we could reliably obtain a typical size for each particle.

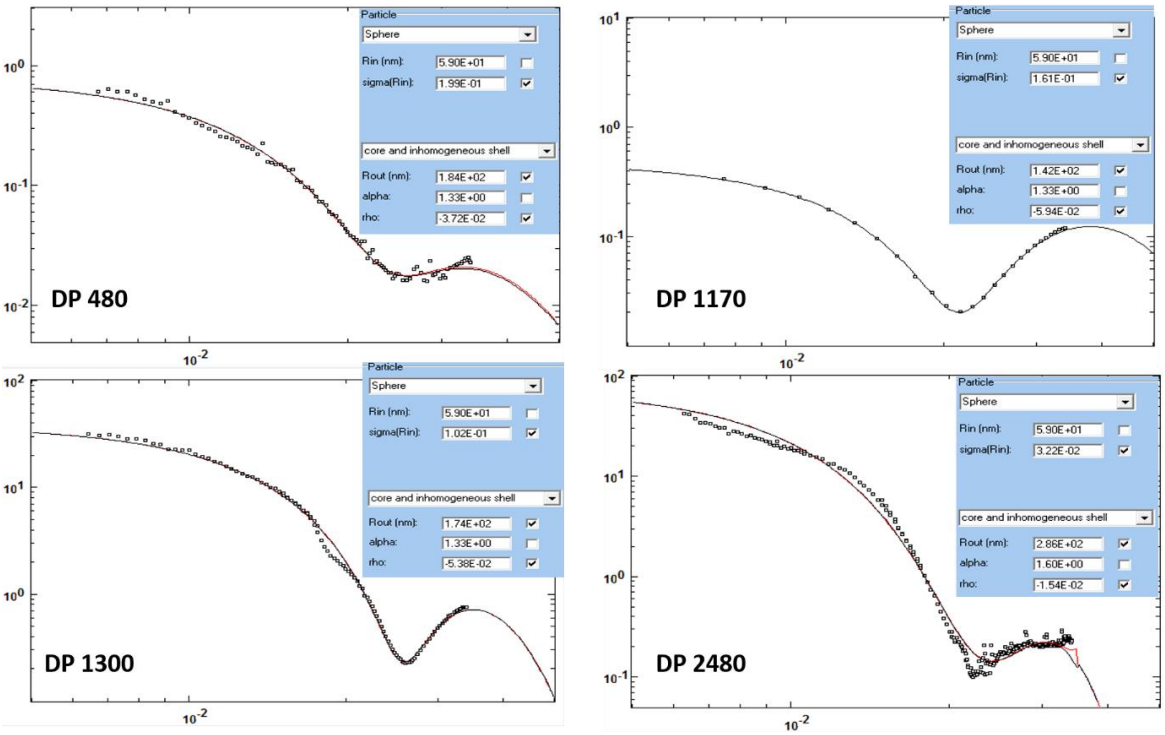

Figure 6-2.Example of the form factors obtained from the static light scattering of four of the Si-PS nanoparticles. Sample codes refer to their degree of polymerization and are given in each plot (see chapter 2 for details). The lines through the data are the best fits using the "Scatter" software (parameters are given in the blue insets).

The size measured with static light scattering is somewhat different from the hydrodynamic radius (which is an apparent size) obtained with dynamic light scattering, as expected for this type of particles. We used the same analysis described above using the Ohno model[42] for grafted nanoparticles (Figure 6-3).

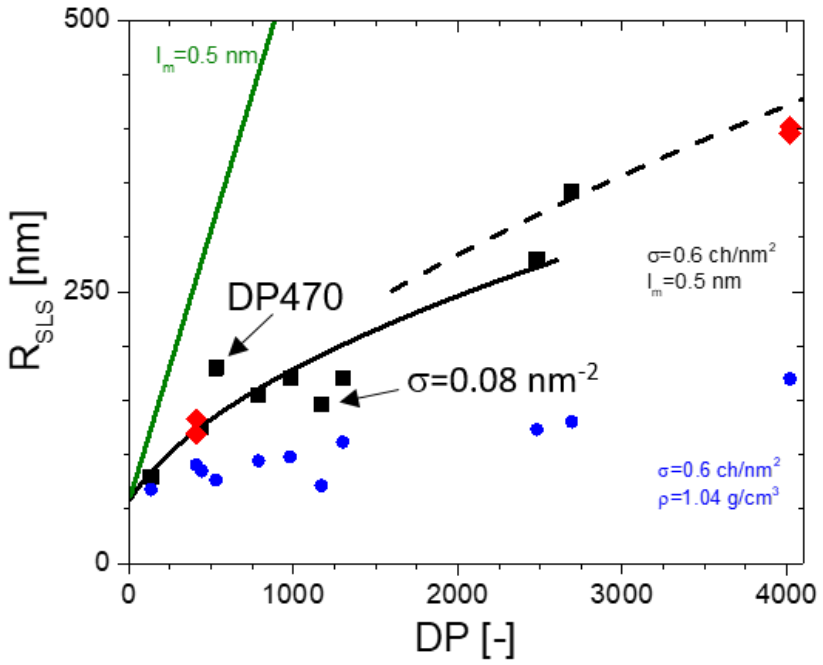

Figure 6-3. Size extracted from static light scattering as a function of the degree of polymerization. Black squares represent the Si-PS particles and the red squares represent the Si-PMMA particles. The blue squares are the calculated values of the collapsed size based on the density of PS (1.06 kg.l^{-1}) and PMMA (1.18 kg.l^{-1}). The green line represents the size at the maximum extension of the grafted chains (with Kuhn monomer size of 0.5 nm). The continuous (respectively dotted) black line is the CPB (respectively SDPB) model prediction of Ohno et al.[42] for a grafting density of 0.6 nm^{-2} and monomer length of 0.5 nm.

The data point at *DP*=480 monomers and σ=0.27 nm^{-2} stands out and does not seem to fit the model or the rest of the data. From the form factor obtained by static light scattering, it was impossible to find an acceptable fit giving a radius under 150nm. However, the auto-correlation function obtained in dynamic light scattering resulted in a diffusion coefficient corresponding to a hydrodynamic radius of 140nm. Therefore we attribute this mismatch between the *DP 480* and the rest of the data to an overestimation of the size by the static light scattering technique.

The rest of the data are in very good agreement with the theoretical model, with a progressive transition from the CPB at low degree of polymerization to the SDPB at higher degrees of polymerization.

6.3 – Second virial coefficient

The analysis of the evolution of the scattered intensity with the concentration provides information about the interactions in the dilute regime via the determination of the second virial coefficient A_2 (see chapter 2). In the limit of small values of the scattering wave vector, q, and dilute conditions, the Zimm equation (chapter 2) is simplified to become:

$$\frac{Kc}{I_0} = \frac{1}{M_w} + 2A_2c \qquad \text{(Equation 2)}$$

The representation of the quantity Kc/I_0 as a function of the concentration was fitted with an affine function with slope $2A_2$ and intercept $1/M_w$ (Figure 6-4). Hence, the slope of this plot provides important qualitative information about the nature of the total interactions between particles in the dilute regime. The experimental values found for the grafted particles studied here are reported in Table 6-1, alongside other microstructural properties.

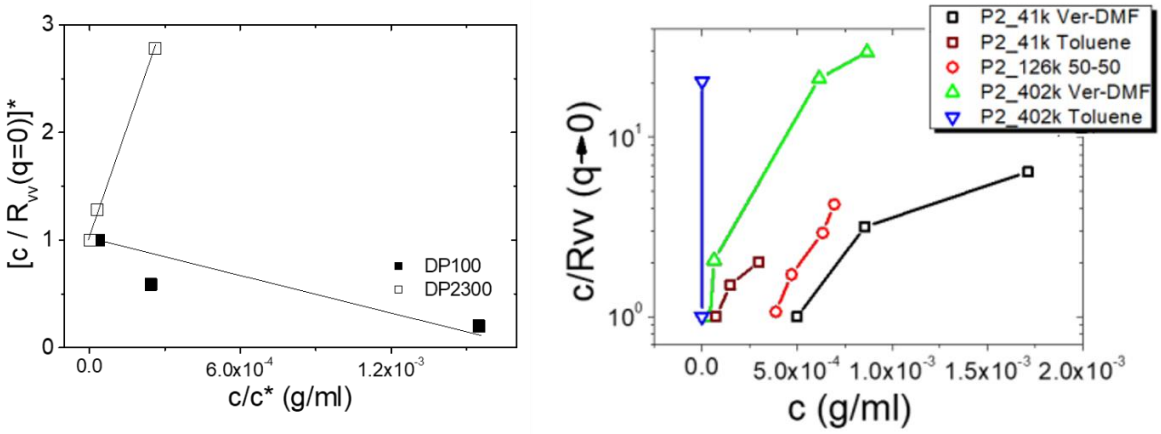

Figure 6-4. Examples of the determination of the experimental value of the second virial coefficient for the Si-PS particles (left) and the Si-PMMA particles (right). Data are taken from S. Kamble[48] and P. Bogri[41,47].

The results show that the samples with the same grafting density and lower degrees of polymerization (shorter chains) have negative values of A_2. This suggests an overall attractive interaction between these particles. However, this attraction is weak and does not lead to aggregation or phase separation in the solutions at these concentrations. This was also observed in the auto-correlation functions measured via dynamic light scattering, which revealed only one diffusive mode at all measured

concentrations (example on Figure 6-5). In the case of the particles with higher degrees of polymerization, A_2 becomes positive, meaning that the net interaction becomes mainly repulsive.

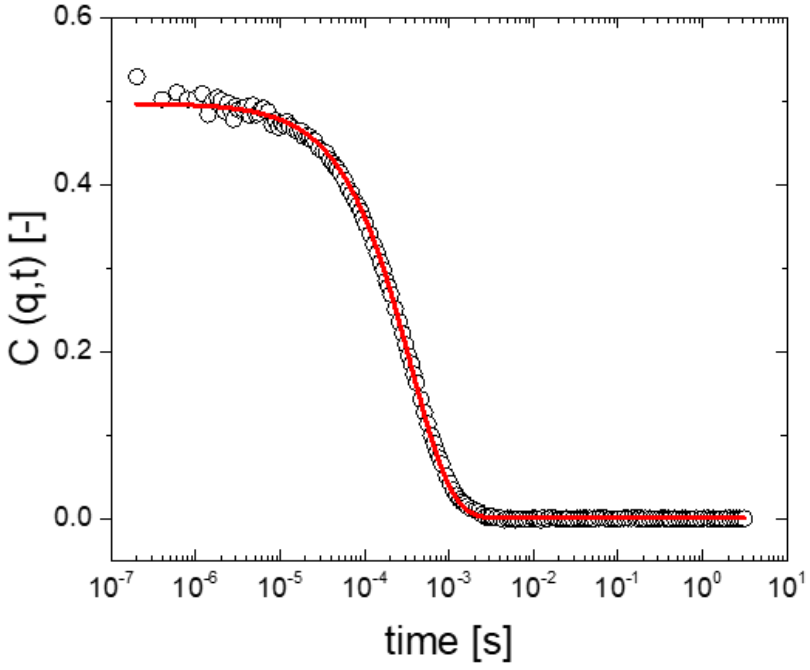

Figure 6-5. Example of a typical field auto-correlation function of a solution of the DP1300 particle at 0.16wt% (highest measured concentration). The angle is 90. The red line is the best fit of the data using a single-mode exponential decay.

Table 6-1. Molecular characteristics of the polymer-grafted nanoparticles and their experimental second virial coefficient.

Code	DP	M_a (kg.mol^{-1})	M_w (10^6 kg.mol^{-1})	σ (nm^{-2})	Rh (nm)	R (nm)	A_2 (mol.cm^3.g.$^{-2}$)
DP130	135	14	1.3	0.61	97	80	-5.62 x10^{-7}
DP440	441	46	2.1	0.61	123	125	-2.69 x10^{-6}
DP790	788	82	2.7	0.52	170	155	-4.97 x10^{-7}
DP980	981	102	3.0	0.49	224	171	-2.36 x10^{-6}
DP2690	2692	280	6.3	0.47	436	343	2.53 x10^{-5}
DP480	480	50	1.8	0.3	140	180	-1.29 x10^{-9}
DP1170	1170	122	1.6	0.08	145	142	8.39 x10^{-9}
DP1300	1300	135	4.3	0.53	190	171	1.84 x10^{-8}
DP2480	2480	258	5.5	0.39	430	227	1.49 x10^{-7}
PMMA 41-ver/DMF	410	41	2.8	0.65	133	133	7.3 x10^{-7}

PMMA 41-toluene	410	41	2.8	0.65	123	119	9.08 x10^{-7}
PMMA 402-ver/DMF	4020	402	15.25	0.65	420	396	3.36 x10^{-6}
PMMA 41-toluene	4020	402	15.25	0.65	470	382	8.97 x10^{-5}

DP: degree of polymerization (number of monomers per chain); M_a: weight-average molar mass of one grafted chain (arm); M_w: weight-average molar mass of the particle; σ: grafting density; R_h: hydrodynamic radius of the particle (DLS); R_{SLS}: radius of the particle (SLS); A_2: second virial coefficient (SLS).

The second virial coefficient can be theoretically computed from the interaction potential. The potential between two grafted particles was modelled by summing three independent components (Equation 3). The model from Likos *et al.*[51,52] was used to model the steric repulsion potential of grafted chains, and a standard Van der Waals potential was introduced to account for the silica core-core dipole interactions. Finally, an additional hard core repulsive contribution was added with an energy value high enough to be considered infinite for all calculations.

$$\beta V(r) = \begin{cases} \infty, & r < 2r_0 \\ \beta U_0\left[-\ln(y) - \frac{9}{5}(1-y) + \frac{1}{3}(1-y^3) - \frac{1}{30}(1-y^6)\right] - \frac{\beta A}{6}\left[\frac{2}{\left(r/r_0\right)^2-4} + \frac{2}{\left(r/r_0\right)^2} + \ln\left(1 - \frac{4}{\left(r/r_0\right)^2}\right)\right], & 2r_0 > r > 2R \\ -\frac{\beta A}{6}\left[\frac{2}{\left(r/r_0\right)^2-4} + \frac{2}{\left(r/r_0\right)^2} + \ln\left(1 - \frac{4}{\left(r/r_0\right)^2}\right)\right], & r > 2R \end{cases}$$

(Equation 3)

where y is a reduced distance such that $y = \frac{r-2r_0}{2(R-r_0)}$, U_0 and A are numerical pre-factors such that $U_0 = \frac{\pi^3}{12}\frac{(R-r_0)^3 r_0 \sigma}{Nl^2}$ and $A = \frac{3k_BT}{4}\left(\frac{n_1^2-n_2^2}{n_1^2+n_1^2}\right) + \frac{3h\nu_e}{16\sqrt{2}}\frac{(n_1^2-n_2^2)^2}{(n_1^2+n_2^2)^{3/2}}$, N is the degree of polymerization, l is the Kuhn length, k_B is the Boltzmann constant, T is the temperature, n_1 and n_2 are the refractive indices of silica and toluene respectively, h is the Planck constant and ν_e is the frequency of the incident light.

The theoretical interaction potentials for the grafted particles studied here are depicted in Figure 6-6. The potential of the particles with the smallest degree of polymerization exhibits considerable short-range attraction compared to the rest of the particles. Due to its substantially lower grafting density compared to the other samples, the grafted nanoparticle DP 1170 exhibits a potential with a smoother increase, which is

an indication of a softer particle. The rest of the samples seem to be very similar in terms of interaction potential, which translates into similar theoretical values of A_2.

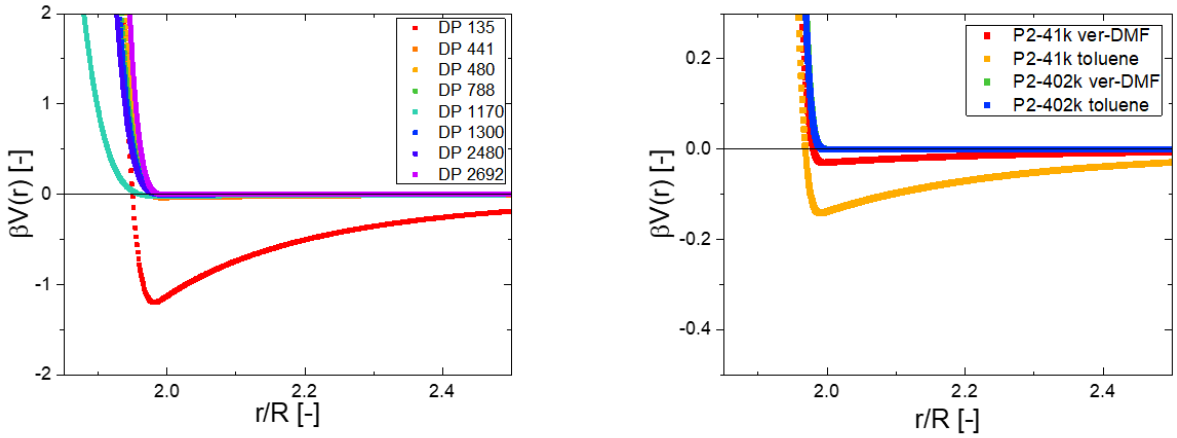

Figure 6-6. Calculated interaction potentials for the Si-PS (left) and Si-PMMA (right) particles. The vertical axis shows the strength of the interactions and is multiplied by $\beta = {}^{1}/_{k_B T}$, the inverse of the thermal energy. The horizontal axis represent the center-to-center distance between two particles divided by their radius (SLS).

A theoretical value of A_2 can be derived from the potential following equation 4[52]. The integral over the center-to center distance r is approximated by a sum over all distance increments $\Delta r=0.1nm$. The radius of gyration R_G is not known and the hydrodynamic size R_h is used instead.

$$\widehat{B_2^{thq}} = \frac{M_w^2 A_2}{N_A R_G^3} = -2\pi \int_0^{+\infty} \left(\frac{r}{R}\right)^2 \left[\exp\left(-\beta V\left(\frac{r}{R}\right)\right) - 1\right] \frac{dr}{R} \quad \text{(Equation 4)}$$

where N_A is the Avogadro number and $\beta=1/k_BT$ is the inverse of the thermal energy.

Although this simple model accurately predicts the negative value of A_2 for the lowest DP, the rest of the data are somewhat overestimated (Figure 6-7). In particular, the prediction for DP 2480 is much larger than the measured value of A_2. Overall, it seems that the core-core attraction and the steric repulsion compensate each other in most of the systems studied here. There is a clear increase of both the predicted A_2 and the measured value for the highest *DP* (DP 2692), which may indicate that the shells are more repulsive after this point. This sample also followed the SDPB model, contrary to the other samples which followed the CPB model (Figure 6-1). This result may be counterintuitive but can be explained by the fact that the shell is now less dense and therefore occupies a

larger volume with respect to the other samples. The respective blobs are larger (cite Daoud-Cotton) and the excluded volume interactions are therefore stronger and may explain the observed increase in A_2. Concerning the sample DP 135, which exhibited more predominant attraction compared to the other samples, this translates into a negative predicted value for A_2, in agreement with the experimental value.

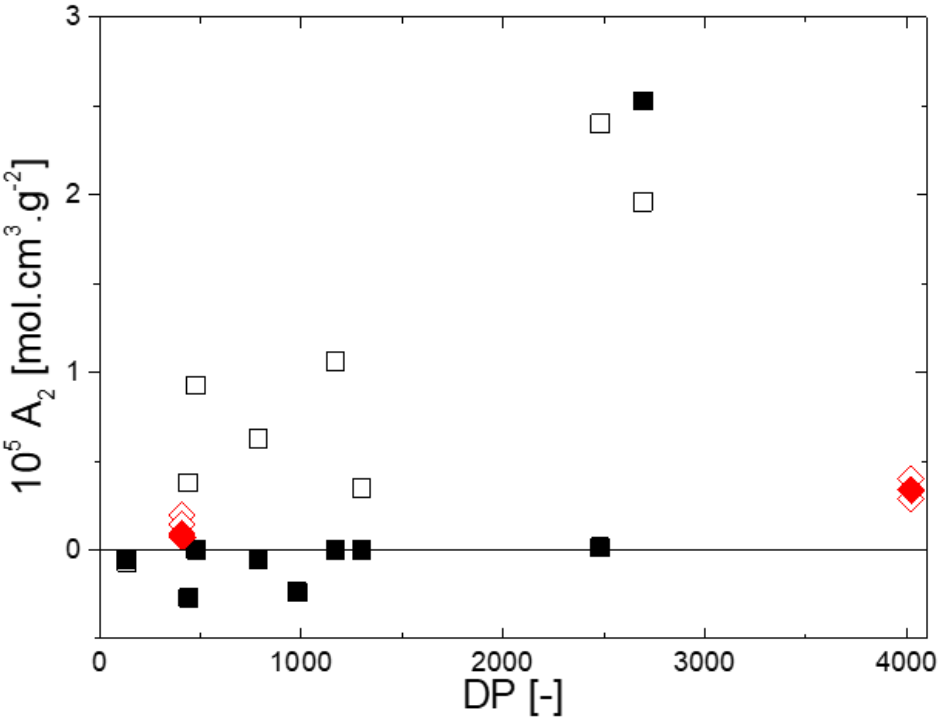

Figure 6-7. Experimental (filled symbols) and calculated (empty symbols) second virial coefficients for the Si-PS (black) and Si-PMMA (red) grafted nanoparticles.

The PMMA core-shell particles were prepared in two different good solvents for PMMA, toluene and a mixture of o-dimethoxy benzene and dimethyl formamide (ver-DMF), to match the optical indices of the shell and the solvent. This has an influence on the Van der Waals electrostatic force between the silica cores through the solvent, which intensity depends on the refractive indices of the materials. The refractive index of the mixture ver-DMF being smaller than the index of toluene, and closer to the index of silica, the Hamacker coefficient dictating the intensity of the attraction between the cores decreases by a factor of about 2. The result can be seen in the interaction potentials plotted in Figure 6-8. The P2-402k sample being much larger than the P2-41k sample, the Van der Waals attraction becomes completely screened by the steric repulsion between the polymeric shells, keeping them far apart. Therefore, the change of solvent does not

translate into a significant change in the interaction potential for the bigger particle. For the smaller particle P2-41k, the size of the shell is also large enough so that the attraction between the cores remains much smaller than k_BT for both solvent, thus not inducing any aggregation or phase separation. The change of solvent has very little effect on the second virial coefficient A_2, which is well predicted by the model described above in this case (Figure 6-7).

6.4 – Conclusions

In conclusion, the polymeric shells of the polymer-grafted nanoparticles studied here are almost always thick enough to efficiently screen the core-core Van der Waals attraction, except in the case of the smallest degree of polymerization (DP 135). The theoretical results are summarized in Figure 6-8, which shows that the chain length has a large impact on the particle size, but not on its potential interactions with neighboring particles. Expect for the shortest chains (DP 470), the corona of the particles is large enough to effectively screen the attractive interactions between the silica cores.

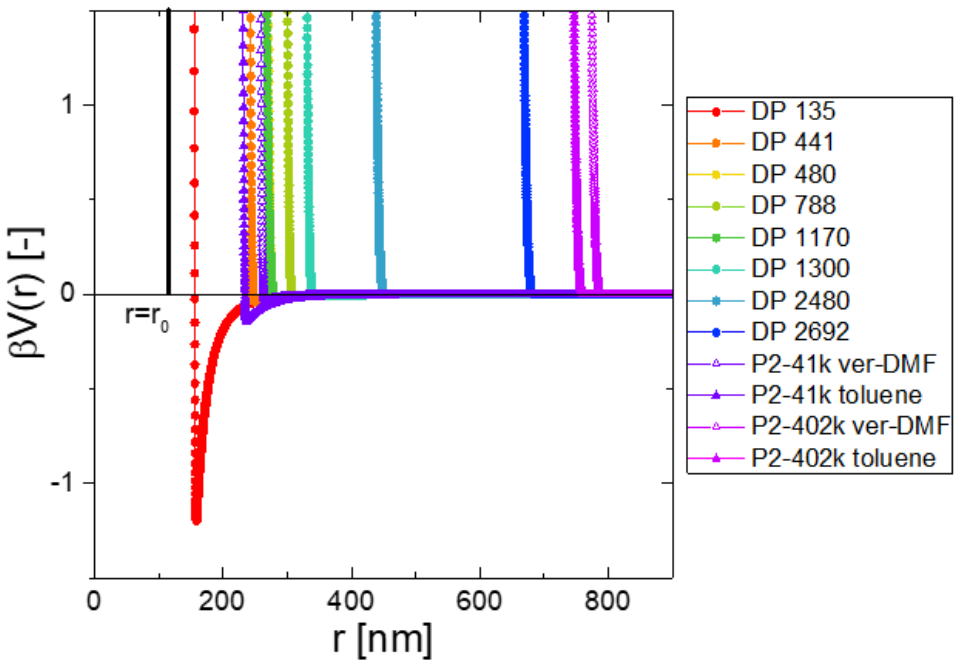

Figure 6-8. Interaction potentials of all particles studied in this chapter. The horizontal axis is the center-to-center distance between two star-like particles. The vertical black line represents the effective hard core of the particles.

Interestingly, the sample with very low grafting density (DP 1170, σ=0.08 nm^{-2}) does not stand out from the other samples despite having a much lower grafting density. Thus we can assume that the polymer chains are long enough to provide a sufficient screening of the Van der Waal interactions. We may expect that this sample would exhibit a significantly different rheological behavior at higher concentrations compared to the other, much more densely grafted particles. The behavior at high concentration was not measured but could represent an interesting question for the future, maybe indicative that interactions in the dilute regime and in the concentrated regime could be different.

References

(1) Ohno, K.; Morinaga, T.; Koh, K.; Tsujii, Y.; Fukuda, T. Synthesis of Monodisperse Silica Particles Coated with Well-Defined, High-Density Polymer Brushes by Surface-Initiated Atom Transfer Radical Polymerization. *Macromolecules* **2005**, *38* (6), 2137–2142. https://doi.org/10.1021/ma048011q.

(2) Rahman, I. A.; Padavettan, V. Synthesis of Silica Nanoparticles by Sol-Gel: Size-Dependent Properties, Surface Modification, and Applications in Silica-Polymer Nanocomposites—A Review. *Journal of Nanomaterials* **2012**, *2012*, 1–15. https://doi.org/10.1155/2012/132424.

(3) Iskandar, F. Nanoparticle Processing for Optical Applications – A Review. *Advanced Powder Technology* **2009**, *20* (4), 283–292. https://doi.org/10.1016/j.apt.2009.07.001.

(4) Gupta, S. M.; Tripathi, M. A Review of TiO2 Nanoparticles. *Chinese Science Bulletin* **2011**, *56* (16), 1639–1657. https://doi.org/10.1007/s11434-011-4476-1.

(5) Pradeep, T.; Anshup. Noble Metal Nanoparticles for Water Purification: A Critical Review. *Thin Solid Films* **2009**, *517* (24), 6441–6478. https://doi.org/10.1016/j.tsf.2009.03.195.

(6) Thorkelsson, K.; Bai, P.; Xu, T. Self-Assembly and Applications of Anisotropic Nanomaterials: A Review. *Nano Today* **2015**, *10* (1), 48–66. https://doi.org/10.1016/j.nantod.2014.12.005.

(7) Moghimi, E.; Jacob, A. R.; Koumakis, N.; Petekidis, G. Colloidal Gels Tuned by Oscillatory Shear. *Soft Matter* **2017**, *13* (12), 2371–2383. https://doi.org/10.1039/C6SM02508K.

(8) Zaccarelli, E.; Poon, W. C. K. Colloidal Glasses and Gels: The Interplay of Bonding and Caging. *PNAS* **2009**, *106* (36), 15203–15208. https://doi.org/10.1073/pnas.0902294106.

(9) Koumakis, N.; Petekidis, G. Two Step Yielding in Attractive Colloids: Transition from Gels to Attractive Glasses. *Soft Matter* **2011**, *7* (6), 2456. https://doi.org/10.1039/c0sm00957a.

(10) Pusey, P. N.; Zaccarelli, E.; Valeriani, C.; Sanz, E.; Poon, W. C. K.; Cates, M. E. Hard Spheres: Crystallization and Glass Formation. *Philosophical Transactions of the Royal Society A: Mathematical, Physical and Engineering Sciences* **2009**, *367* (1909), 4993–5011. https://doi.org/10.1098/rsta.2009.0181.

(11) Pusey, P. N.; van Megen, W. Phase Behaviour of Concentrated Suspensions of Nearly Hard Colloidal Spheres. *Nature* **1986**, *320* (6060), 340–342. https://doi.org/10.1038/320340a0.
(12) Derks, D.; Wu, Y. L.; van Blaaderen, A.; Imhof, A. Dynamics of Colloidal Crystals in Shear Flow. *Soft Matter* **2009**, *5* (5), 1060. https://doi.org/10.1039/b816026k.
(13) Dinsmore, A. D.; Crocker, J. C.; Yodh, A. G. Self-Assembly of Colloidal Crystals. *Current Opinion in Colloid & Interface Science* **1998**, *3* (1), 5–11. https://doi.org/10.1016/S1359-0294(98)80035-6.
(14) Agarwal, P.; Srivastava, S.; Archer, L. A. Thermal Jamming of a Colloidal Glass. *Phys. Rev. Lett.* **2011**, *107* (26). https://doi.org/10.1103/PhysRevLett.107.268302.
(15) Christopoulou, C.; Petekidis, G.; Erwin, B.; Cloitre, M.; Vlassopoulos, D. Ageing and Yield Behaviour in Model Soft Colloidal Glasses. *Philosophical Transactions of the Royal Society of London A: Mathematical, Physical and Engineering Sciences* **2009**, *367* (1909), 5051–5071. https://doi.org/10.1098/rsta.2009.0166.
(16) Mason, T. G.; Weitz, D. A. Linear Viscoelasticity of Colloidal Hard Sphere Suspensions near the Glass Transition. *Phys. Rev. Lett.* **1995**, *75* (14), 2770.
(17) Ballauff, M.; Brader, J. M.; Egelhaaf, S. U.; Fuchs, M.; Horbach, J.; Koumakis, N.; Krüger, M.; Laurati, M.; Mutch, K. J.; Petekidis, G.; et al. Residual Stresses in Glasses. *Phys. Rev. Lett.* **2013**, *110* (21). https://doi.org/10.1103/PhysRevLett.110.215701.
(18) Cortes, L. B. G.; Gao, Y.; Dullens, R. P. A.; Aarts, D. G. A. L. Colloidal Liquid Crystals in Square Confinement: Isotropic, Nematic and Smectic Phases. *Journal of Physics: Condensed Matter* **2017**, *29* (6), 064003. https://doi.org/10.1088/1361-648X/29/6/064003.
(19) van der Kooij, F. M.; Lekkerkerker, H. N. W. Formation of Nematic Liquid Crystals in Suspensions of Hard Colloidal Platelets. *The Journal of Physical Chemistry B* **1998**, *102* (40), 7829–7832. https://doi.org/10.1021/jp981534d.
(20) Kuijk, A.; Byelov, D. V.; Petukhov, A. V.; van Blaaderen, A.; Imhof, A. Phase Behavior of Colloidal Silica Rods. *Faraday Discussions* **2012**, *159*, 181. https://doi.org/10.1039/c2fd20084h.
(21) Lars Onsager. The Effects of Shape on the Interaction of Colloidal Particles. *Annals of the New York Academy of Sciences* **1949**, *51* (4), 627–659.
(22) Srivastava, S.; Shin, J. H.; Archer, L. A. Structure and Rheology of Nanoparticle–Polymer Suspensions. *Soft Matter* **2012**, *8* (15), 4097. https://doi.org/10.1039/c2sm06889c.
(23) Derec, C.; Ducouret, G.; Ajdari, A.; Lequeux, F. Aging and Nonlinear Rheology in Suspensions of Polyethylene Oxide–Protected Silica Particles. *Physical Review E* **2003**, *67* (6). https://doi.org/10.1103/PhysRevE.67.061403.
(24) Erdem, N.; Cireli, A. A.; Erdogan, U. H. Flame Retardancy Behaviors and Structural Properties of Polypropylene/Nano-SiO_2 Composite Textile Filaments. *Journal of Applied Polymer Science* **2009**, *111* (4), 2085–2091. https://doi.org/10.1002/app.29052.
(25) Nelson, A.; Cosgrove, T. Small-Angle Neutron Scattering Study of Adsorbed Pluronic Tri-Block Copolymers on Laponite. *Langmuir* **2005**, *21* (20), 9176–9182. https://doi.org/10.1021/la050680p.

(26) Sugimoto, M.; Ishizuka, K.; Hatano, K.; Sukumaran, S. K.; Aoki, Y. Viscoelastic Behavior of PMMA/Grafted PBA Nanoparticle Systems in the Molten State. *Rheol. Acta* **2017**, *56* (10), 779–785. https://doi.org/10.1007/s00397-017-1037-9.
(27) Akcora, P.; Kumar, S. K.; García Sakai, V.; Li, Y.; Benicewicz, B. C.; Schadler, L. S. Segmental Dynamics in PMMA-Grafted Nanoparticle Composites. *Macromolecules* **2010**, *43* (19), 8275–8281. https://doi.org/10.1021/ma101240j.
(28) Hong, R. Y.; Qian, J. Z.; Cao, J. X. Synthesis and Characterization of PMMA Grafted ZnO Nanoparticles. *Powder Technology* **2006**, *163* (3), 160–168. https://doi.org/10.1016/j.powtec.2006.01.015.
(29) Chevigny, C.; Gigmes, D.; Bertin, D.; Jestin, J.; Boué, F. Polystyrene Grafting from Silica Nanoparticles via Nitroxide-Mediated Polymerization (NMP): Synthesis and SANS Analysis with the Contrast Variation Method. *Soft Matter* **2009**, *5* (19), 3741. https://doi.org/10.1039/b906754j.
(30) Vestal, C. R.; Zhang, Z. J. Atom Transfer Radical Polymerization Synthesis and Magnetic Characterization of $MnFe_2O_4$ /Polystyrene Core/Shell Nanoparticles. *Journal of the American Chemical Society* **2002**, *124* (48), 14312–14313. https://doi.org/10.1021/ja0274709.
(31) Savin, D. A.; Pyun, J.; Patterson, G. D.; Kowalewski, T.; Matyjaszewski, K. Synthesis and Characterization of Silica-Graft-Polystyrene Hybrid Nanoparticles: Effect of Constraint on the Glass-Transition Temperature of Spherical Polymer Brushes. *Journal of Polymer Science Part B: Polymer Physics* **2002**, *40* (23), 2667–2676. https://doi.org/10.1002/polb.10329.
(32) Kongsinlark, A.; Rempel, G. L.; Prasassarakich, P. Synthesis of Monodispersed Polyisoprene–Silica Nanoparticles via Differential Microemulsion Polymerization and Mechanical Properties of Polyisoprene Nanocomposite. *Chemical Engineering Journal* **2012**, *193–194*, 215–226. https://doi.org/10.1016/j.cej.2012.04.008.
(33) Chunzhao Li; Brian Benicewicz. Synthesis of Well-Defined Polymer Brushes Grafted onto Silica Nanoparticles via Surface Reversible Addition−Fragmentation Chain Transfer Polymerization. *Macromol.* **2005**, *38* (14), 5929–5936.
(34) Tancharernrat, T.; Rempel, G. L.; Prasassarakich, P. Synthesis of Polybutadiene-Silica Nanoparticles via Differential Microemulsion Polymerization and Their Hydrogenated Nanoparticles by Diimide Reduction. *Polymer Degradation and Stability* **2015**, *118*, 69–81. https://doi.org/10.1016/j.polymdegradstab.2015.04.008.
(35) Zheng, L.; Xie, A. F.; Lean, J. T. Polystyrene Nanoparticles with Anionically Polymerized Polybutadiene Brushes. *Macromolecules* **2004**, *37* (26), 9954–9962. https://doi.org/10.1021/ma048499v.
(36) Chen, J.; Liu, M.; Chen, C.; Gong, H.; Gao, C. Synthesis and Characterization of Silica Nanoparticles with Well-Defined Thermoresponsive PNIPAM via a Combination of RAFT and Click Chemistry. *ACS Applied Materials & Interfaces* **2011**, *3* (8), 3215–3223. https://doi.org/10.1021/am2007189.
(37) Dong, Z.; Wei, H.; Mao, J.; Wang, D.; Yang, M.; Bo, S.; Ji, X. Synthesis and Responsive Behavior of Poly(N,N-Dimethylaminoethyl Methacrylate) Brushes Grafted on Silica Nanoparticles and Their Quaternized Derivatives. *Polymer* **2012**, *53* (10), 2074–2084. https://doi.org/10.1016/j.polymer.2012.03.011.
(38) Yu, F.; Tang, X.; Pei, M. Facile Synthesis of PDMAEMA-Coated Hollow Mesoporous Silica Nanoparticles and Their PH-Responsive Controlled Release. *Microporous and*

Mesoporous Materials **2013**, *173*, 64–69. https://doi.org/10.1016/j.micromeso.2013.02.012.
(39) Cayre, O. J.; Chagneux, N.; Biggs, S. Stimulus Responsive Core-Shell Nanoparticles: Synthesis and Applications of Polymer Based Aqueous Systems. *Soft Matter* **2011**, *7* (6), 2211–2234. https://doi.org/10.1039/C0SM01072C.
(40) Perruchot, C.; Khan, M. A.; Kamitsi, A.; Armes, S. P.; von Werne, T.; Patten, T. E. Synthesis of Well-Defined, Polymer-Grafted Silica Particles by Aqueous ATRP. *Langmuir* **2001**, *17* (15), 4479–4481. https://doi.org/10.1021/la0102758.
(41) Pamvouxoglou, A.; Bogri, P.; Nägele, G.; Ohno, K.; Petekidis, G. Structure and Dynamics in Suspensions of Soft Core-Shell Colloids in the Fluid Regime. *The Journal of Chemical Physics* **2019**, *151* (2), 024901. https://doi.org/10.1063/1.5091845.
(42) Ohno, K.; Morinaga, T.; Takeno, S.; Tsujii, Y.; Fukuda, T. Suspensions of Silica Particles Grafted with Concentrated Polymer Brush: Effects of Graft Chain Length on Brush Layer Thickness and Colloidal Crystallization. *Macromolecules* **2007**, *40* (25), 9143–9150. https://doi.org/10.1021/ma071770z.
(43) Chremos, A.; Douglas, J. F. Particle Localization and Hyperuniformity of Polymer-Grafted Nanoparticle Materials. *Annalen der Physik* **2017**, *529* (5), 1600342. https://doi.org/10.1002/andp.201600342.
(44) Vlassopoulos, D.; Fytas, G.; Roovers, J.; Pakula, T.; Fleischer, G. Ordering and Dynamics of Soft Spheres in Melt and Solution. *Faraday Discussions* **1999**, *112*, 225–235. https://doi.org/10.1039/a809305i.
(45) Yethiraj, A.; van Blaaderen, A. A Colloidal Model System with an Interaction Tunable from Hard Sphere to Soft and Dipolar. *Nature* **2003**, *421* (6922), 513–517. https://doi.org/10.1038/nature01328.
(46) Pakula, T. A Model for Dense Colloidal Systems with Deformable, Incompressible Particles. *The Journal of Chemical Physics* **1991**, *94* (3), 2104–2109. https://doi.org/10.1063/1.459933.
(47) Bogri, P. Dynamics of Concentrated Colloidal Suspensions, 2018.
(48) Samruddhi Kamble. (Unpublished Data). **2016**.
(49) Förster, S.; Apostol, L.; Bras, W. Scatter : Software for the Analysis of Nano- and Mesoscale Small-Angle Scattering. *Journal of Applied Crystallography* **2010**, *43* (3), 639–646. https://doi.org/10.1107/S0021889810008289.
(50) Daoud, M.; Cotton, J. P. Star Shaped Polymers : A Model for the Conformation and Its Concentration Dependence. *Journal de Physique* **1982**, *43* (3), 531–538. https://doi.org/10.1051/jphys:01982004303053100.
(51) Likos, C. N.; Löwen, H.; Watzlawek, M.; Abbas, B.; Jucknischke, O.; Allgaier, J.; Richter, D. Star Polymers Viewed as Ultrasoft Colloidal Particles. *Phys. Rev. Lett.* **1998**, *80* (20), 4450.
(52) Likos, C. N.; Löwen, H.; Poppe, A.; Willner, L.; Roovers, J.; Cubitt, B.; Richter, D. Ordering Phenomena of Star Polymer Solutions Approaching the Θ State. *Physical Review E* **1998**, *58* (5), 6299.

Chapter 7: Conclusions and Perspectives

The solid regime of colloids, and in particular the suspensions of soft particles investigated here, is a complex topic since it deals with out-of-equilibrium physics and metastable states of matter. Its study requires special attention to be paid to protocols, experimental conditions and data analysis, in order to ensure high quality and reproducibility of the data. At the same time, the potential applications of soft solids are countless, in numerous fields such as the petrochemical industry, plastic and rubber manufacturing, cosmetics, the construction industry, medicine, food products and plenty of others. These applications necessitate the careful design of materials with tunable novel mechanical, optical and/or chemical properties. Therefore, the fundamental understanding of the physical processes at play in these materials and their link to macroscopic performance are of utmost importance.

This work focuses on the thorough examination of well-characterized, model soft colloidal systems and the meticulous description of their linear and nonlinear rheological properties. It is hoped that it advances the current state-of-the-art towards a better understanding of the solid colloidal regime that is necessary for establishing a clear connection between microstructure and material properties. For example, one main conclusion of chapter 3 is the effective jamming of star polymers in the melt, which had not been observed before. This was possible thanks to their extremely high functionality and the short length of the arms, and led to the elaboration of a two dimensional state diagram. This diagrams classifies the stars into three regimes (polymeric, hybrid and jammed) based on their dynamic properties and depends both on the arm size and the functionality. Data from the literature obtained with other high functionality stars and grafted nanoparticles seemed to adhere to this classification, hence strongly suggesting that a generic understanding of soft hairy colloids is possible.

Both the extreme values of functionality and arm size provided a material with polymeric properties at high frequencies or low temperatures, which also exhibits significant elasticity and does not relax stresses at low frequencies or room temperature.

As demonstrated in chapters 4 and 5, this allows to store mechanical energy for very long times. This represents a good example of the way one can tune the properties of a material by only changing its microstructure. It also demonstrates the ability of a purely polymeric material to jam, which is a rich, albeit not fully understood state of colloidal matter.

We called jamming the transition inside the solid regime of colloids that occurs at large concentration and is characterized mainly by the contacts between the particles. The unique properties of soft colloids, and in particular star polymers, to squeeze and deform allows them to pack extremely efficiently at high concentration. Since the center-to-center distance can become smaller than the particle size, due to the interplay of deformation and interpenetration, even small changes in the microstructure may greatly affect the rheological behavior. To elucidate this point, we compared in this work microgels and star polymers, which differ mostly by the presence of dangling ends in the latter case. This small difference did not have a significant effect at low or intermediate concentrations, but was found to be crucially important in controlling their nonlinear viscoelastic response at high concentrations in the jamming regime. This provides an important element to take into account for further investigation of soft colloids.

In the linear viscoelastic regime, a generic behavior can be found in several soft colloids with different chemistries, microstructure and shape, such that a universal scaling of their linear viscoelastic properties (in particular the linear dependence of the plateau modulus on concentration in the jammed regime) may be possible. If further confirmed, this may provide a useful tool to predict the behavior of other soft colloidal systems. The universality of this scaling is however still unclear, and the exact requirements on the microstructure leading to this behavior are still mostly empirical.

In the nonlinear regime, we also reported on the very different mechanical behavior of stars and microgels when the concentration was increased. While star polymers maintained their ability to flow under shear even in the melt, microgels exhibited a much more fragile behavior and fractured under large strains. The exact origin of fracture and, in more general terms, the possible link of ductile or fragile response to details of particle microstructure are still unclear and could represent an axis for further

investigations. The measurement of velocity profiles during shear is an appropriate technique for this purpose.

As mentioned above, the solid state of colloids is by nature a non-equilibrium state. Hence, its physical properties can evolve in time, a process which we referred to in this work as aging. Since the mechanical properties, especially in the nonlinear regime, depended very much on the aging time of a sample, we used a simple rejuvenation protocol able to put the materials back into a reproducible state before conducting further measurements. The exact influence of this protocol on the results of the measurements was thoroughly examined, but the exact nature of aging was not investigated as such. For example, the exact influence of the aging time on the structure of the material is still unclear for this type of soft colloids. Based on previous literature and new results of this thesis, we expect that the rejuvenated material solidifies with time, but an exact quantification (for example, as function and number and size of star arms) is still missing.

Since the synthesis of experimental systems such as star polymers require the use of complex coupling chemistry techniques and purification methods, the final yields are usually low. Therefore experimental systems are scarce and the systematic study of the influence of the functionality and the size of the arms may be better addressed using computer simulations. Indeed, simulations represent a powerful tool in this context, with the possibility to compare to existing experimental data while at the same time being able to extrapolate the results to different microstructures. With current technology, the coarse-graining of the system is still mandatory, since we are primarily interested in high concentration systems. However, careful attention must be given that the coarse-graining does not hide some of the smaller scale effects, such as the arm interpenetration, which seem to be of the highest importance to correctly model the high concentration properties of star polymers.

Different experimental techniques may be used to complete the rheological investigations conducted here. Microscopy, and in particular fluorescence microscopy which often has better resolution, is a well suited technique for the direct observation of the deformation of soft colloids in situ. However it often requires to use either big particles (>1μm) or tracer particles.

Moreover, the coupling of two or more experimental techniques provides a unique opportunity to link observations from two independent instruments. For example, we reported on the development of a rheo-DLS setup in Appendix III that may provide useful structural information on the aging behavior of colloidal glasses. Another setup was also developed in the lab that consists in a miniaturized light scattering instrument that can be attached under the bottom plate of a commercial rheometer to measure small-angle light scattering under shear.

Usual spectroscopic methods may also be used, such as small angle X-ray or neutron scattering. The difficulty mostly lies on the careful design of such experiments, in order to obtain reliable and useful data. Indeed, the interpretation of the data from such experiments (and any spectroscopic data in general) is often left at the discretion of the user. Therefore, a lot of different data (systems, conditions) have to be considered before drawing any conclusion. In addition, these techniques usually require the chemical functionalization of the colloids to increase contrast, which can be both difficult experimentally and/or lead to different properties of the functionalized colloids. At the same time, the specific labelling of precise parts of the sample may be turned to our advantage. In the case of star polymers, this could be the arms, the core or the outermost monomers at the chain ends, which can provide space-resolved information.

Other mechanical tests, such as extensional rheology, may also be performed on jammed colloids. Preliminary results on jammed stars showed that under certain conditions, they may exhibit a brittle behavior and break at large strains. We expect that this behavior very much depends on the experimental conditions, such as the strain rate, however further experiments were not carried out due to the difficulty to obtain reliable, repeatable measurements. This represents a completely new axis of development for further work.

In the everlasting quest of designing better, more efficient or greener materials, the colloidal toolbox does not stop at the microstructure, though. While it is important to develop a better understanding of the basics before going further, one may imagine using more complex approaches to design more sophisticating properties. For instance, responsive polymers are able to change their size, conformation or physical and chemical

properties upon the application of an external stimulus such as an electric or magnetic field, temperature, pH or salt concentration. The introduction of such polymers in colloidal materials therefore opens the door for innovative tunable performances that react to their surrounding medium. Another example is in the combination of two or more particle types. The study of mixtures of colloids is a challenge, as it drastically increases the complexity of the phase diagram, but leads to interesting properties. As an example, we can cite the liquefaction of a colloidal glass by the introduction of a smaller, non-interacting particle (such as a polymer or a smaller colloid), due to depletion effects. Therefore the mixture of colloids is very often much more subtle that the sum of its individual components and is a great system to investigate jamming in view of the present results.

Finally, a whole new set of possibilities also opens-up when attraction is introduced between the colloids. Although strong attractive interactions may lead to phase separation, moderate attraction is the key to the formation of gels, which are essentially solids with a low mass fraction content in particles. The most famous example may be the trendy aerogels, which are extremely light solids with many applications in aerospace engineering and housing, but gels are also a very common state of matter in the everyday life, for example in yoghurts and ice creams. Gels, and by extrapolation suspensions of attractive colloids, therefore represent a large category of materials with extremely rich and complex physics.

Appendix I: Volume fraction of soft colloids

Volume fraction is the ratio of the volume occupied by the particles to the total volume in a colloidal system. For hard spheres, volume fraction is the only parameter of the (one-dimensional) phase diagram. One of the main method to obtain the volume fraction in hard spheres is to centrifugate the particles at high speeds to obtain a master batch[1]. The volume fraction of this mater batch is estimated (for example by drying part of it and weighing the solid content) and other suspensions are prepare by dilution.

It is often used in colloidal suspensions to scale the absolute concentration of particles and compare different systems to each other. In soft colloids, the volume of the particle alters with the concentration, hence the volume fraction is a complex function of the concentration. Therefore, unless one knows exactly how the volume of a soft particle changes with mass fraction, the determination of its volume fraction is a very difficult problem[1]. This goal of this appendix is to present a simple model to estimate the equivalent hard sphere volume fraction of soft colloids based on their viscosity.

I.1 – Introduction

While for hard spheres, the volume fraction can be determined either by dilution of a known sample or by weighting the dry mass of the suspension, there is no clear relation *a priori* between the mass and the volume fraction of soft colloids. The most commonly used method is to scale the concentration using the so-called overlapping concentration c*[2,3], by analogy with polymers. The overlap concentration represents the regime where the average concentrations of monomer inside and outside of a particle become equal (Figure I-1). In other words, this is theoretically the concentration at which two particles effectively touch each other. The calculation of this overlap concentration is usually based on the mass and the size of a particle, which can be both determined by light scattering[4–6]. For this reason, the size that is considered is the size of the particle in the dilute regime, where interactions between particles are negligible. This leads to a gross overestimation of the volume fraction when the size of the particle gets smaller at

higher concentration, very often yielding volume fractions much higher than 1. Although this problem is well known in the soft colloid community, the rescaling of concentration with c* has the advantage to be simple and at least offers a way to compare different types of soft colloids.

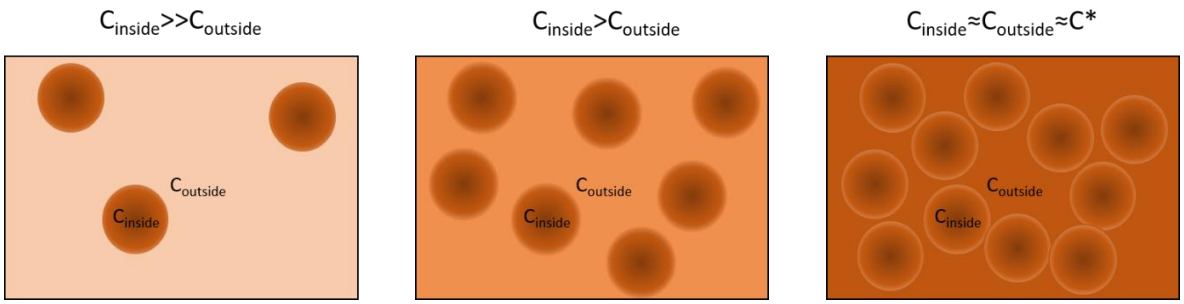

Figure I-1. Schematic representation of the equilibrium of the concentration inside and outside of the particles and the definition of the overlap concentration c.*

The calculation of a more precise volume fraction often requires a way to estimate the concentration dependence of the size, which can be done with microscopy for larger particles[7] or scattering for the smaller ones[8], but is subject to large errors and depends on the interpretation of the data. Finally, some attempts at using theoretical models to predict the volume fraction at a given concentration have been used rather successfully[9,10], although they are usually limited to a given range of concentrations and may not give satisfying results outside of this range. To resolve this problem, we propose a simple model based on the mapping of the zero-shear viscosity of soft colloids on hard spheres.

I.2 – Theoretical model

The model crudely assumes that soft colloids behave as effective hard spheres, except that their size changes with concentration. In the very dilute regime, the interactions between particles are negligible and therefore the exact nature of their potential (as long as it is purely repulsive) does not have a significant influence on the properties of the suspension. For example, the zero-shear viscosity of a very dilute suspension of colloids obeys the Einstein-Batchelor equation (Equation 1). The development of this model is based on the gross assumption that this remains true when the concentration is increased.

$$\eta_0 = \eta_s(1 + 2.5kc + 5.2(kc)^2) \qquad \text{(Equation 1)}$$

where η_0 is the zero-shear viscosity of the suspension, η_s is the suspending medium viscosity, k is a fitting parameter and c is the concentration of the colloids.

The second assumption of the model is that the zero-shear viscosity is only a function of the volume fraction. This is well-known for hard spheres, whose size does not influence the resulting viscosity. This may not hold true for soft particles, because hydrodynamic interactions may depend on the microstructure of the particles. Based on these assumptions, we can estimate the effective hard sphere volume fraction (HSϕ) of soft colloids by mapping their zero-shear viscosity onto the zero-shear viscosity of hard spheres. Several models have been developed for the zero-shear viscosity of hard spheres[11–13], which have only a small influence on the results presented here. Therefore, the choice of the model is not crucial as long as it is used consistently, and we select the model developed by Mendoza et al.[12], which seems to capture well the experimental data and is given in Equation 2. We impose the divergence of the zero-shear viscosity at a maximum packing fraction of 0.64, by analogy with the random close packing of monodisperse hard spheres[1,14]. Using data from this work and the literature (as discussed below), we determine HSϕ for several star polymer and microgel solutions (Figure I-2) by using equation 3, and we invert equation 2 to calculate the HSϕ corresponding to the measured zero-shear viscosity (Equation 4):

$$\eta_{r,hard}(\varphi) = \left(1 - \frac{\varphi}{1-c\varphi}\right)^{-5/2} \qquad \text{Equation 2}$$

$$\eta_{r,soft}(c) = \eta_{r,HS}(HS\phi) \qquad \text{Equation 3}$$

$$HS\phi = \frac{1-\eta_r^{-2/5}}{1+c(1-\eta_r^{-2/5})} \qquad \text{Equation 4}$$

where $\eta_{r,hard}$ and $\eta_{r,soft}$ are the relative zero-shear viscosities of hard and soft colloids, respectively, φ is the volume fraction, $c = \frac{1-\varphi_{max}}{\varphi_{max}}$ and φ_{max} is the maximum packing fraction (0.64).

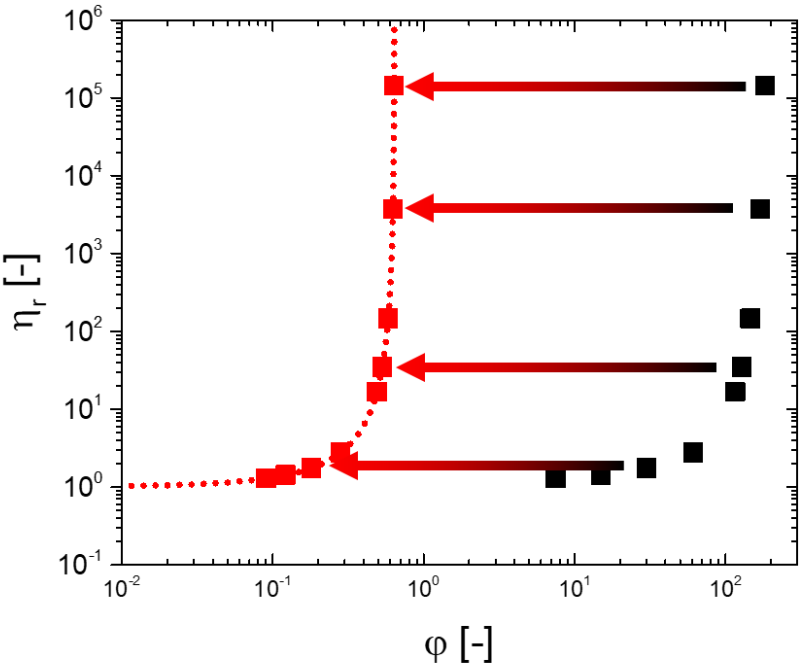

Figure I-2. Graphical representation of the method used to estimate the HSϕ of soft colloids. The black squares (experimental data for the star 875/06) are shifted onto the dotted line (Mendoza model for the viscosity of hard spheres with φ_m=0.64). The obtained red squares give the corresponding HSϕ.

Using this method, we obtain the HSϕ as a function of concentration for the stars and microgels (Figure I-3). The general behavior is always similar in all cases. At low concentrations, there is a linear regime where $HS\phi \sim c$, corresponding to the regime of validity of the overlapping concentration scaling $\varphi \sim \frac{c}{c^*}$. This provides an alternative determination of c*. This regime is followed by a slowing-down of the evolution of volume fraction with concentration due to particle de-swelling. Indeed, since the volume of each particle decreases, the volume fraction increases slowly with the concentration. We then observe for some systems a quasi-plateau of the volume fraction, which becomes almost independent of the concentration.

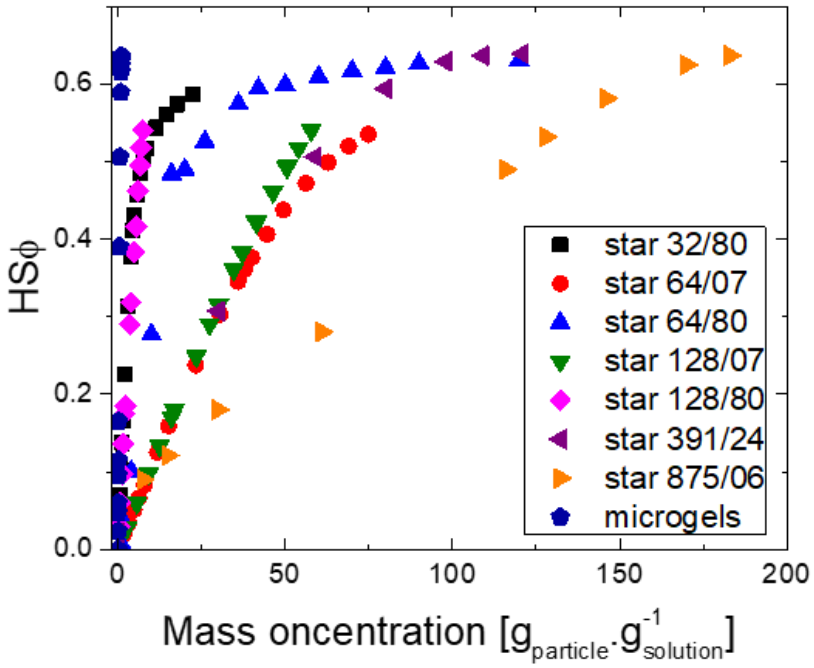

Figure I-3. Effective hard sphere volume fraction (HSϕ) of a range of star polymers and the microgels described in chapter 2.

The microgels and the stars have a different de-swelling mechanism (see chapter 2), because the swelling of the microgels essentially comes from the presence of counter-ions inside the particle. On the contrary, stars only swell due to the effective attraction of the solvent molecules and the monomer molecules (solvent quality). Figure I-3 thus gives a visual representation of the comparative softness of the star systems, with the softer stars on the left (low c*) and the harder stars on the right (high c*). Not surprisingly, the stars with short arms are mainly on the right hand side of the plot, in agreement with the findings of chapters 3 and 4.

Mathematically, the HSϕ is capped at 0.64, which is the maximum packing fraction we chose for this model. Therefore, some of the datasets (star 64/80, star 391/24 and to a lesser degree star 32/80 and star 875/06) seem to reach a plateau at high concentrations. We do not expect that this represents the physical behavior of these systems. At this packing fraction the stars are expected to touch and additional mechanisms to pure de-swelling should be at work, such as shape deformation and interpenetration. Thus for soft particles, the volume fraction is not limited to the hard sphere value of 0.64, but can increase up to 1 through deformation (faceting of the

particle shape) and interpenetration (sharing of the same volume between two or more particles).

Accounting for these processes requires more advanced modelling, however we propose here the simplest approach which involves a linear dependence of the volume fraction when these processes take place. We propose that the transition between this linear dependence and the previously described model (equation 4) should be smooth, therefore the derivative of the HSϕ just before and just after the transition should be equal. By definition, we also know that this volume fraction of polymer in the melt is 1, and therefore we can extrapolate between the transition concentration and the melt (Figure I-4).

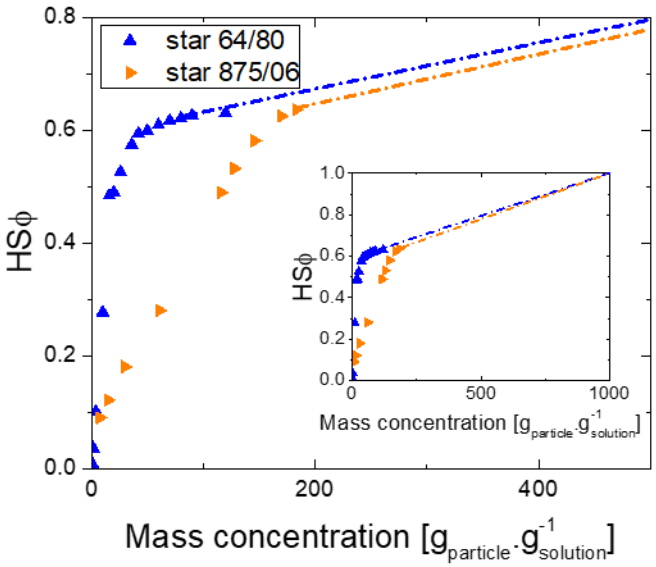

Figure I-4. Extension of the HSϕ of two star polymers in the concentrated regime with a linear extrapolation to the melt (HSϕ=1). Inset: Extrapolation to the melt and HSϕ=1. These particular stars were selected because we had more data at intermediate concentrations.

To conclude, we tried here to lay out the basis for a simple, yet robust model linking the concentration and the volume fraction of soft colloids. This is based on the mapping onto the zero-shear viscosity of hard spheres to provide a simple estimation of the volume fraction in at the low and intermediate concentrations. The extension of this model in the more concentrated regime is however difficult, due to the appearance of other processes affecting the shape and the volume of the particles.

References

(1) Pusey, P. N.; Zaccarelli, E.; Valeriani, C.; Sanz, E.; Poon, W. C. K.; Cates, M. E. Hard Spheres: Crystallization and Glass Formation. *Philosophical Transactions of the Royal Society A: Mathematical, Physical and Engineering Sciences* **2009**, *367* (1909), 4993–5011. https://doi.org/10.1098/rsta.2009.0181.

(2) Cotton, J. P.; Nierlich, M.; Boué, F.; Daoud, M.; Farnoux, B.; Jannink, G.; Duplessix, R.; Picot, C. Experimental Determination of the Temperature–Concentration Diagram of Flexible Polymer Solutions by Neutron Scattering. *The Journal of Chemical Physics* **1976**, *65* (3), 1101–1108. https://doi.org/10.1063/1.433172.

(3) Daoud, M.; Cotton, J. P.; Farnoux, B.; Jannink, G.; Sarma, G.; Benoit, H.; Duplessix, C.; Picot, C. Solutions of Flexible Polymers. Neutron Experiments and Interpretation. **1975**, *8* (6), 15.

(4) Wyatt, P. J. Light Scattering and the Absolute Characterization of Macromolecules. *Analytica Chimica Acta* **1993**, *272* (1), 1–40. https://doi.org/10.1016/0003-2670(93)80373-S.

(5) Kerker, M. *The Scattering of Light and Other Electromagnetic Radiation*; Elsevier, 2016.

(6) *Light Scattering from Polymer Solutions and Nanoparticle Dispersions*; Springer Laboratory; Springer Berlin Heidelberg: Berlin, Heidelberg, 2007. https://doi.org/10.1007/978-3-540-71951-9.

(7) Bouhid de Aguiar, I.; van de Laar, T.; Meireles, M.; Bouchoux, A.; Sprakel, J.; Schroën, K. Deswelling and Deformation of Microgels in Concentrated Packings. *Scientific Reports* **2017**, *7* (1). https://doi.org/10.1038/s41598-017-10788-y.

(8) Pakula, T.; Vlassopoulos, D.; Fytas, G.; Roovers, J. Structure and Dynamics of Melts of Multiarm Polymer Stars. *Macromol.* **1998**, *31* (25), 8931–8940. https://doi.org/10.1021/ma981043r.

(9) Pellet, C.; Cloitre, M. The Glass and Jamming Transitions of Soft Polyelectrolyte Microgel Suspensions. *Soft Matter* **2016**, *12* (16), 3710–3720. https://doi.org/10.1039/C5SM03001C.

(10) Truzzolillo, D.; Vlassopoulos, D.; Gauthier, M. Osmotic Interactions, Rheology, and Arrested Phase Separation of Star–Linear Polymer Mixtures. *Macromol.* **2011**, *44* (12), 5043–5052. https://doi.org/10.1021/ma2007078.

(11) Krieger, I. M.; Dougherty, T. J. A Mechanism for Non-Newtonian Flow in Suspensions of Rigid Spheres. *Transactions of the Society of Rheology* **1959**, *3* (1), 137–152. https://doi.org/10.1122/1.548848.

(12) Mendoza, C. I.; Santamar?a-Holek, I. The Rheology of Hard Sphere Suspensions at Arbitrary Volume Fractions: An Improved Differential Viscosity Model. *The Journal of Chemical Physics* **2009**, *130* (4), 044904. https://doi.org/10.1063/1.3063120.

(13) Quemada, D. Rheology of Concentrated Disperse Systems II. A Model for Non-Newtonian Shear Viscosity in Steady Flows. *Rheologica Acta* **1978**, *17* (6), 632–642. https://doi.org/10.1007/BF01522036.

(14) Pusey, P. N.; van Megen, W. Phase Behaviour of Concentrated Suspensions of Nearly Hard Colloidal Spheres. *Nature* **1986**, *320* (6060), 340–342. https://doi.org/10.1038/320340a0.

Appendix II - Particle image velocimetry of sheared microgel glasses

This aim of this appendix is to measure the flow profiles in sheared microgel solutions to estimate the importance of wall slip, shear banding or other flow instabilities on the rheological properties. This is useful first to ensure the quality of the rheological measurements that were performed on this system, and secondly this gives us an interesting insight in the interplay of yielding and slip.

I.1 – Introduction

Wall slip is one of the many concerns one has when performing rheological experiments with weak solids such as colloidal gels or glasses[1–4]. Although some reports suggest that wall slip may have a significant influence on the oscillatory measurements[5], the most dramatic effects have been observed in steady shear flows[6,7] and can lead to the misinterpretation of the data. Depending on the application and the flow conditions, , wall slip can be beneficial for the process, either by effectively lowering the resistance of the material against flow and therefore saving energy[4], or by modifying the surface of the final product[8]. In some situations, however, slip is detrimental for the final product[9] (stick-slip, melt fracture …). In addition, wall slip is ubiquitous in soft matter, and has been observed for foams[10,11], slurries[12], fresh cement[13], polymer melts[14] and solutions[15], and colloidal glasses[1,2,4,16]. There are several methods to prevent wall slip from happening, including the roughening of the shearing tools, surface treatment to favor surface adhesion or the use of different materials[4,16].

We used an optical microscope coupled with a commercial shear rheometer (Physica MCR 302 from Anton Paar) to measure the flow profile of concentrated suspensions of polyelectrolyte microgels (presented in chapter 2 and used in chapter 4) under shear. A cartoon representation is provided on Figure II-1. The experiments were carried out in the C3M lab at the ESPCI. To visualize the flow, a negligible amount (<0.01% wt) of fluorescent particles was added to the microgel suspension at low volume fraction

and homogenized. The volume fraction was then suddenly increased by addition of sodium hydroxide to the acidic suspension, to cause the deprotonation of the acidic moieties present in the microgels (see chapter 2). The resulting material was a slightly pink (due to the red dye of the tracer particles), weak solid. Its rheological properties essentially depended on concentration, but a weight fraction as low as 1% resulted in solid behavior at all accessible frequencies.

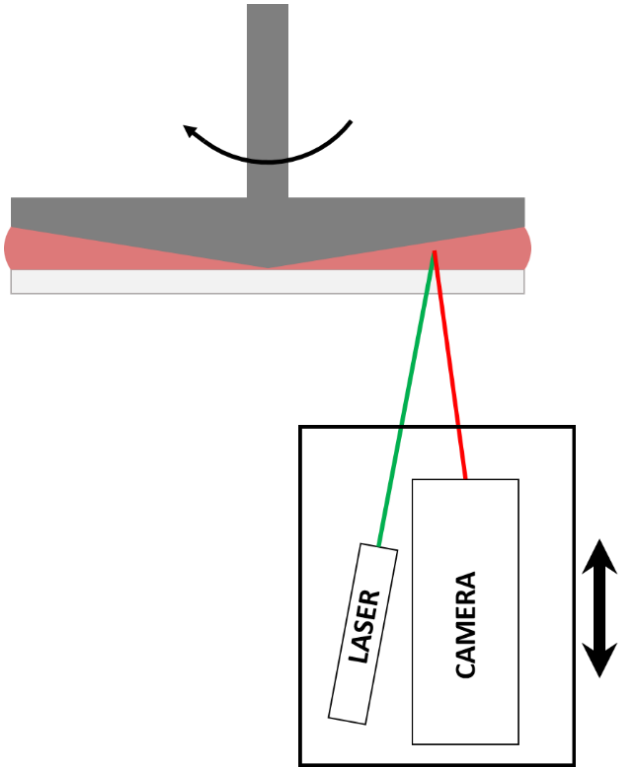

Figure II-14. Cartoon representation of the rheo-PIV setup. The bottom plate is transparent to the incident and fluorescent light (quartz plate). The top cone is a commercial tool of the rheometer. The laser and the camera are mounted on a translational stage to probe the sample at different distances from the bottom plate.

II.2 – Results

We performed particle velocimetry experiments (PIV) on three samples at the weight fractions of 2%, 5% and 12%. Linear viscoelastic characterization was first performed to assess the elastic and viscous moduli G' and G" (Figure II-2). For all three concentrations, G' was found to be higher than G", representative of a weak solid and in agreement with previous studies of these microgel particles[17] (see chapter 4). We then

measured the dynamic yield strain and stress by means of a dynamic strain sweep test (Figure II-3). The three samples exhibited typical colloidal glass behavior with an extended linear regime during which G' and G" are independent of strain amplitude, followed by a fast decrease of G' accompanied by a peak in G", followed by a decrease of G".

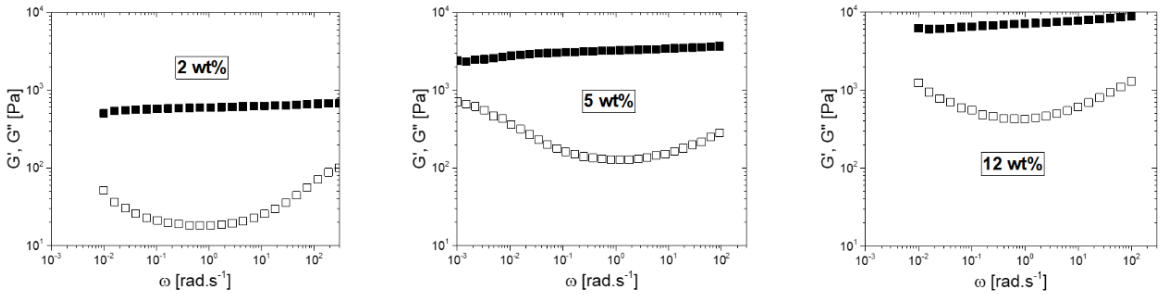

Figure II-2. Dynamic frequency sweeps of the microgel solutions at three different concentrations (from left to right: 2 wt%, 5 wt% and 12 wt%, see figure). The filled black squares represent the elastic modulus and the empty black squares represent the viscous modulus.

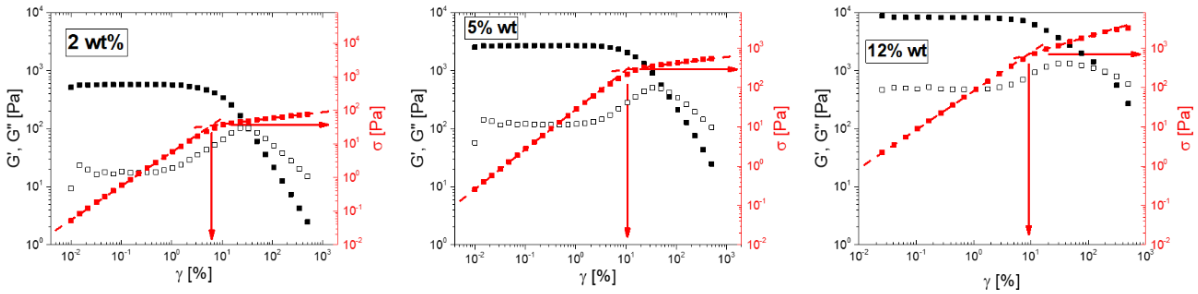

Figure II-3. Dynamic strain sweeps of the microgel solutions at three different concentrations (from left to right: 2 wt%, 5 wt% and 12 wt%, see figure). The filled black squares represent the elastic modulus and the empty black squares represent the viscous modulus, their values can be read on the left axis. The red squares represent the stress whose value can be read on the right axis. The red arrows point towards the yield strain (vertical) and stress (horizontal).

We then performed steady shear experiments with the shear rate being kept constant (start-up flow). The camera positioned under the flow cell allowed recording the motion of the fluorescent tracer particles at various distances from the transparent bottom plate. The optical setup had a depth of field of about 10 µm, which ultimately limited its spatial resolution in the z-direction. Pictures of the moving particles were taken at a constant time interval *dt*. This interval was calculated such that particles moved by

about 2 microns between two consecutive images (assuming the theoretical shear rate imposed by the rheometer). This ensured that the motion of the particles could be accurately measured. The series of pictures were then analyzed using a dedicated Matlab program developed by Maddalena Mattiello[18]. The program correlates two consecutive pictures using a matrix correlation technique to determine the displacement of the particles with an accuracy of less than 1 micron (x-y plane resolution). The velocity of the particles was then calculated for each pair of images. The experiments were carried out recording about 200 pictures for each position, such that a reliable average velocity could be determined.

The velocity of the tracer particles was assumed to be identical to their surrounding environment, such that the sample velocity could be measured throughout the gap. The highest concentration sample (12 wt%) exhibited a time-dependent velocity profile and did not reach a steady state stress during the experiment. These observations suggest the occurrence of shear-banding or the propagation of edge-fracture[19]. Some of these observations have already been mentioned in chapter 4, but we shall discuss them further at the end of this part. The velocity profiles of the 2 wt% and 5 wt% solutions (Figure II-4) show complete slip at low shear rates and the development of the so-called plug-flow regime[20]. The entire material slips at the velocity of the top plate and the shear rate inside the material is effectively 0. We verified that the measured maximum velocity was identical to the theoretical one calculated from the shear rate, ensuring that the slip only happens at the bottom plate. The use of a serrated metallic cone as the top surface proved to be enough to limit the shear to the much smoother glass surface at the bottom[2,4]. The velocity profiles at high shear rates show some irregularities close to the top surface, which are within the experimental error but may suggest that partial slips start to occur at the top surface as well. Since this is a limited effect compared to the slip at the bottom surface, this had no appreciable effect on the analysis of the results.

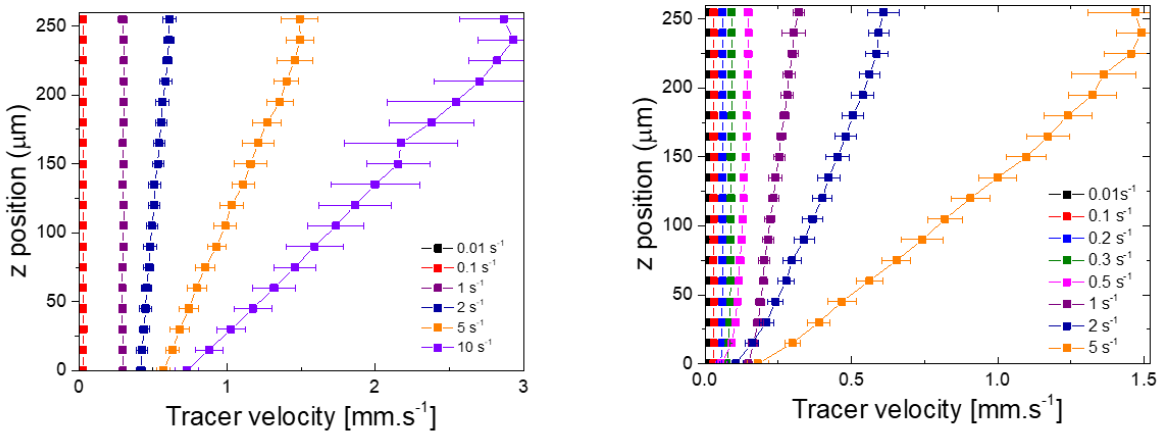

Figure II-4. Velocity profiles of the 2 wt% (left) and 5 wt% (right) microgel solutions. The different shear rates are indicated by different colors as indicated on the plots (insets). The vertical axis indicates the distance from the bottom plate (which is located at z=0). The gap is 255 µm.

When the shear rate was increased, we observed that the slip velocity at the bottom plate also increased for both samples (Figure II-4), but shear also developed inside the material. We represent this behavior by plotting the slip velocity (velocity at the bottom plate at z=0) normalized by the top plate velocity (Figure II-5). This representation shows an apparent critical shear rate after which the plug flow regime disappears. It is replaced by a regime where slip is present but the bulk material is also sheared homogeneously, that we call partial slip regime.

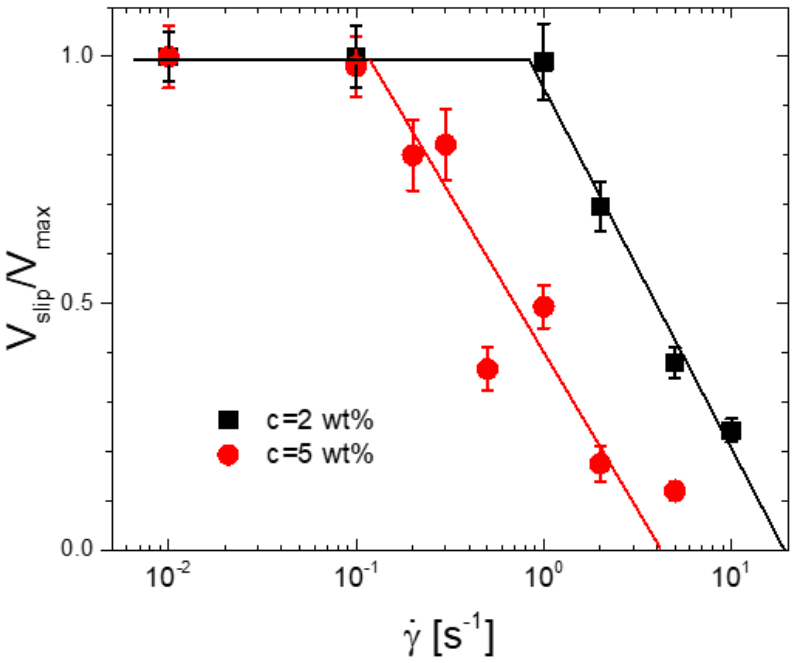

Figure II-5. Slip velocity (at bottom plate) divided by the velocity of the top cone for the 2 wt% (black squares) and 5 wt% (red squares) microgel solutions. Lines are drawn to guide the eye and show the plug-flow region (horizontal lines) and the partial slip region (inclined lines).

At the highest measured shear rate, the slip velocity at the bottom plate becomes a small fraction (<20%) of the top cone velocity. This is also visible in the apparent flow curve of these materials, which recover their non-slipping behavior at high shear rates (Figure II-6). In the plug-flow and partial slip regimes, it is clear that the apparent stress is much less than the real shear stress (under no-slip condition), hence the analysis of the flow curve appears like a good way to estimate the presence of slip in a sheared soft solid.

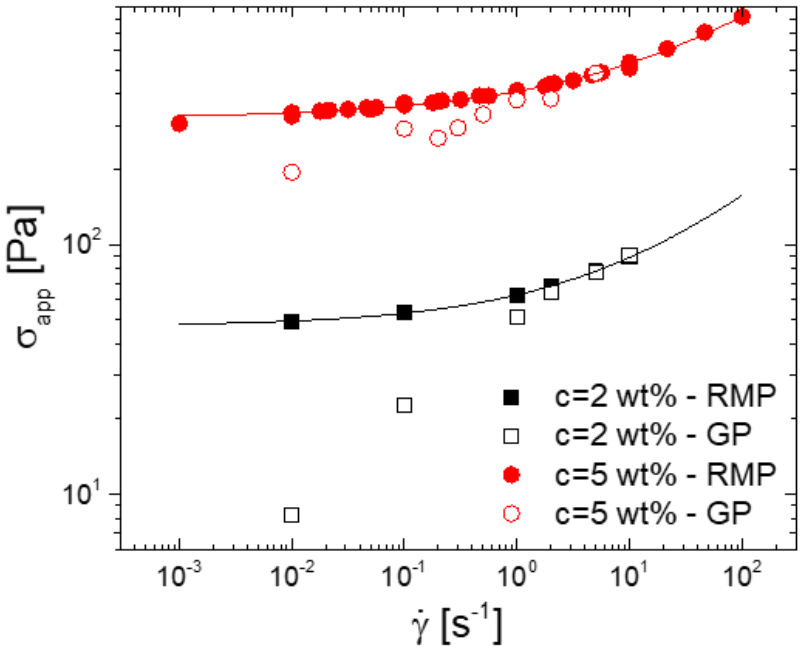

Figure II-6. Apparent stress (measured with the rheometer) as a function of the imposed shear rate for 2 wt% and the 5 wt% microgel solutions. The filled triangles represent the data obtained with a rough stainless steel cone-and plate (RMP) and the empty symbols represent the data obtained with a smooth glass plate at the bottom and the rough stainless steel cone at the top (GP). The lines are the best fits of the RMP data using the Hesrchel-Bulkley model.

As already discussed at the end of chapter 4, the flow profiles of a 12 wt% microgel solution exhibited a strong time dependence and a large deviation from the theoretical velocity profile expected with this geometry (Figure II-7). To verify this behavior, we performed a series of short experiments probing only the middle section of the gap. Form this test, it was clear that the flow velocity inside the sample during shear was rapidly and constantly changing, and no general, constant trend was found. This is a clear example of transient shear banding.

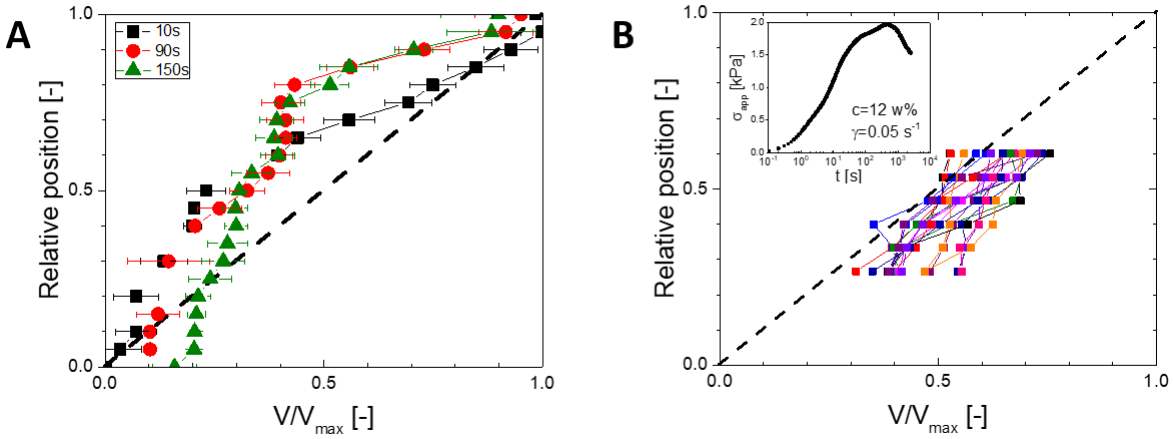

Figure II-7. A) Velocity profiles inside a 12 wt% microgel solution under steady shear at $\dot{\gamma} = 0.05s^{-1}$*. The three profiles were taken at different moments after the start-up of the shear, indicated on the figure (inset). B) Sequential velocity profiles in the middle of the gap (z=50 to z=150* μ*m) for the same 12 wt% microgel solution under steady shear at* $\dot{\gamma} = 0.05s^{-1}$*. Each experiment takes approximately 60 s and there is a short delay of about 15 s between two consecutive experiments. The inset shows the evolution of the apparent stress measured by the rheometer during the steady shearing. The dashed lines represent the theoretical velocity at this shear rate.*

We note in addition, that steady shearing (even at low shear rates) rapidly caused the expulsion of the material outside of the measuring gap (Figure II-8). The stress did not reach a steady state but an erratic behavior was observed until it and eventually decreased with time (Figure II-7). This measurement does not reflect the material's viscoelastic properties, but rather the fact that microgel solutions at high concentrations are unable to flow homogeneously. Instead, the material breaks.

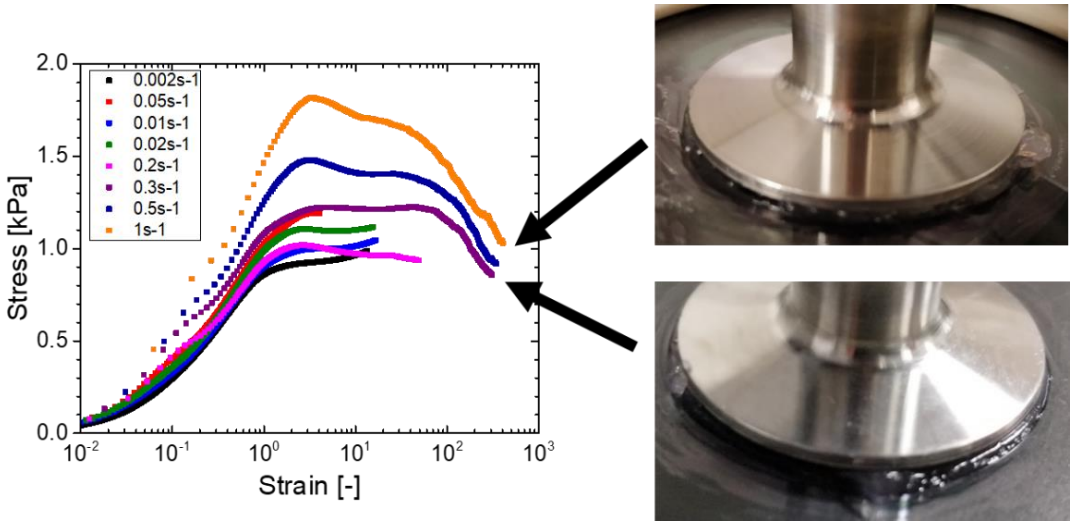

Figure II-8. Apparent shear stress of a 12 wt% microgel solution under steady shear showing the absence of steady state at this concentration. Pictures on the right illustrate the edge of the material at the end of two of the experiments. A large amount of the material was expelled from the gap, which explains the observed apparent stress.

II.3 – Conclusions and perspectives

In conclusion, the wall slip of concentrated microgel solutions strongly depends on the applied shear rate and the concentration. We showed that there are two regimes of slip. At low shear rates, the plug flow regime dominates, therefore the material is not sheared and moves as a block with the top cone. At higher shear rates, the slip is only partial and the material is sheared, although the effective shear rate is much lower than the imposed value. The transition occurs at a critical shear rate that decreases with the concentration, such that the more concentrated solution (and therefore stronger material) was less prone to slip. However, solutions at very high concentrations (c>10 wt%) lose their ability to flow homogeneously under steady shear and will break very early in the nonlinear regime. The flow profiles showed strong transient and steady shear banding inside the gap, consistent with the inability of the bulk material to homogeneously deform at high strains. Macroscopically, we observed that a large amount of the material was pushed out of the measuring gap after the experiment, and therefore the rheological data in the nonlinear regime highly concentrated microgel solutions cannot be trusted.

We tried to replicate this experiment with concentrated star polymer solutions, using glass beads as tracer particles, but without success. The absence of fluorescence of

the tracers induced a large amount of noise from the reflection of the incident light, which made the image analysis impossible. Quantum dots with high fluorescence efficiency and a good chemical affinity for the stars and the suspending medium (squalene) are currently chosen as the best candidate as suitable tracer particles. In addition, the development of a pulsed laser setup should also increase the available range of velocities that can be measured with this technique.

References

(1) Bertola, V.; Bertrand, F.; Tabuteau, H.; Bonn, D.; Coussot, P. Wall Slip and Yielding in Pasty Materials. *Journal of Rheology* **2003**, *47* (5), 1211–1226. https://doi.org/10.1122/1.1595098.

(2) Seth, J. R.; Locatelli-Champagne, C.; Monti, F.; Bonnecaze, R. T.; Cloitre, M. How Do Soft Particle Glasses Yield and Flow near Solid Surfaces? *Soft Matter* **2012**, *8* (1), 140–148. https://doi.org/10.1039/C1SM06074K.

(3) Barnes, H. A. A Review of the Slip (Wall Depletk)n) of Polymer Solutions, Emulsionsand Particle Suspensionsin Viscometers:Its Cause,Character, and Cure. 31.

(4) Cloitre, M.; Bonnecaze, R. T. A Review on Wall Slip in High Solid Dispersions. *Rheologica Acta* **2017**, *56* (3), 283–305. https://doi.org/10.1007/s00397-017-1002-7.

(5) Yoshimura, A. S.; Prud'homme, R. K. Wall Slip Effects on Dynamic Oscillatory Measurements. *Journal of Rheology* **1988**, *32* (6), 575–584. https://doi.org/10.1122/1.549982.

(6) Yoshimura, A.; Prud'homme, R. K. Wall Slip Corrections for Couette and Parallel Disk Viscometers. *Journal of Rheology* **1988**, *32* (1), 53–67. https://doi.org/10.1122/1.549963.

(7) Yilmazer, U.; Kalyon, D. M. Slip Effects in Capillary and Parallel Disk Torsional Flows of Highly Filled Suspensions. *Journal of Rheology* **1989**, *33* (8), 1197–1212. https://doi.org/10.1122/1.550049.

(8) El Kissi, N.; Piau, J.-M.; Toussaint, F. Sharkskin and Cracking of Polymer Melt Extrudates. *Journal of Non-Newtonian Fluid Mechanics* **1997**, *68* (2–3), 271–290. https://doi.org/10.1016/S0377-0257(96)01507-8.

(9) Hatzikiriakos, S. G. Slip Mechanisms in Complex Fluid Flows. *Soft Matter* **2015**, *11* (40), 7851–7856. https://doi.org/10.1039/C5SM01711D.

(10) Andrew M. Krnaik. Foam Flows - Kraynik.Pdf. *Ann. Rev. Fluid Mech.* **1988**, *20*, 325–357.

(11) Cohen-Addad, S.; Höhler, R.; Pitois, O. Flow in Foams and Flowing Foams. *Annual Review of Fluid Mechanics* **2013**, *45* (1), 241–267. https://doi.org/10.1146/annurev-fluid-011212-140634.

(12) Liangyong Chen; Yufeng Duan; Meng Liu; Changsui Zhao. Slip Flow of Coal Water Slurries in Pipelines. *Fule* **2010**, *89* (5), 1119–1126.

(13) Saak, A. W.; Jennings, H. M.; Shah, S. P. The Influence of Wall Slip on Yield Stress and Viscoelastic Measurements of Cement Paste. *Cement and Concrete Research* **2001**, *31* (2), 205–212. https://doi.org/10.1016/S0008-8846(00)00440-3.
(14) Hatzikiriakos, S. G. Wall Slip of Molten Polymers. *Progress in Polymer Science* **2012**, *37* (4), 624–643. https://doi.org/10.1016/j.progpolymsci.2011.09.004.
(15) Mhetar, V.; Archer, L. A. Slip in Entangled Polymer Solutions. *Macromolecules* **1998**, *31* (19), 6639–6649. https://doi.org/10.1021/ma971339h.
(16) Ballesta, P.; Petekidis, G.; Isa, L.; Poon, W. C. K.; Besseling, R. Wall Slip and Flow of Concentrated Hard-Sphere Colloidal Suspensions. *Journal of Rheology* **2012**, *56* (5), 1005–1037. https://doi.org/10.1122/1.4719775.
(17) Pellet, C.; Cloitre, M. The Glass and Jamming Transitions of Soft Polyelectrolyte Microgel Suspensions. *Soft Matter* **2016**, *12* (16), 3710–3720. https://doi.org/10.1039/C5SM03001C.
(18) Maddalena Mattiello. Structure and Dynamics of Dense Suspensions of Soft Colloids with Tunable Short-Range Attraction, 2018.
(19) Schweizer, T.; Stöckli, M. Departure from Linear Velocity Profile at the Surface of Polystyrene Melts during Shear in Cone-Plate Geometry. *Journal of Rheology* **2008**, *52* (3), 713–727. https://doi.org/10.1122/1.2896110.
(20) Isa, L.; Besseling, R.; Poon, W. C. K. Shear Zones and Wall Slip in the Capillary Flow of Concentrated Colloidal Suspensions. *Physical Review Letters* **2007**, *98* (19). https://doi.org/10.1103/PhysRevLett.98.198305.

Appendix III – DLS on stars and a simple rheo-DLS setup for in-situ structural measurements during aging

This appendix focuses on the dynamic light scattering of star solutions at low and intermediate concentrations, up to the solidification transition. It also describes the development of a rheo-DLS setup able to accurately measure the auto-correlation function of the scattered light from sample during or after shear, the latter being the focus here. In particular, this is useful in the context of aging colloidal glasses and crystals.

III.1 – Introduction

When light passes through a fluid, it can interact with the molecules or atoms constituting the fluid in several ways. While the incident light can be absorbed, we focus here on its quasi-elastic scattering, which is a change in the light direction without any change of its frequency. The amount of light that is scattered by a fluid depends strongly on the size of its constituents (the scatterers), which makes colloidal suspensions very good scatterers in general, compared to atoms or molecules. If the optical index difference between the suspending fluid and the colloids is large enough, a significant fraction of the incident light is scattered.

The dynamic light scattering (DLS) technique uses the time auto-correlation of the scattered light to infer structural information on the scattering fluid (see chapter 2). In the dilute regime, DLS is an easy and relatively simple way to access the particle's hydrodynamic size, based on its diffusion coefficient. In more concentrated regimes, additional effects affect the correlation of the scattered light, whose careful analysis can provide valuable structural information.

In practice, a laser beam is used as a coherent light source, which is sent to pass through a cuvette (light scattering cell) containing the sample. Scattered light is detected at various angles around the sample using a goniometer and a photon-sensitive receptor

(camera or photon multiplier). The time-dependent intensity is measured and a correlator calculates the auto-correlation function of this intensity (see chapter 2). The decay of the auto-correlation function is related to the Brownian motion of the scatterers.

III.2 – DLS of star polymers[1] at rest

The auto-correlation function of star polymers (RS128PBD5, f=875, M_a=5.8 kg.mol^{-1}) in dilute solution in a good solvent (squalene) is well captured by the single-mode exponential decay given in Equation 1.

$$C(q,t) = A\exp[-\Gamma(\mathrm{q})t] \qquad \text{(Equation 1)}$$

where C (q,t) is the intensity auto-correlation function, q is the wave vector of the scattered light, t is the time, A is a numerical factor and Γ(q) is the characteristic decay rate.

A similar results is obtained using the CONTIN analysis (Figure III-1). CONTIN is a non-linear regularization algorithm used in the context of DLS to infer the distribution of relaxation times in the auto-correlation function[2]. Since this is an ill-posed problem, this distribution is not unique and the user must make choices based on prior knowledge of the sample or the consistency of the results. For this reason, the careful characterization of the (simpler) dilute regime can provide a useful basis for the analysis of the more complicated higher concentrations.

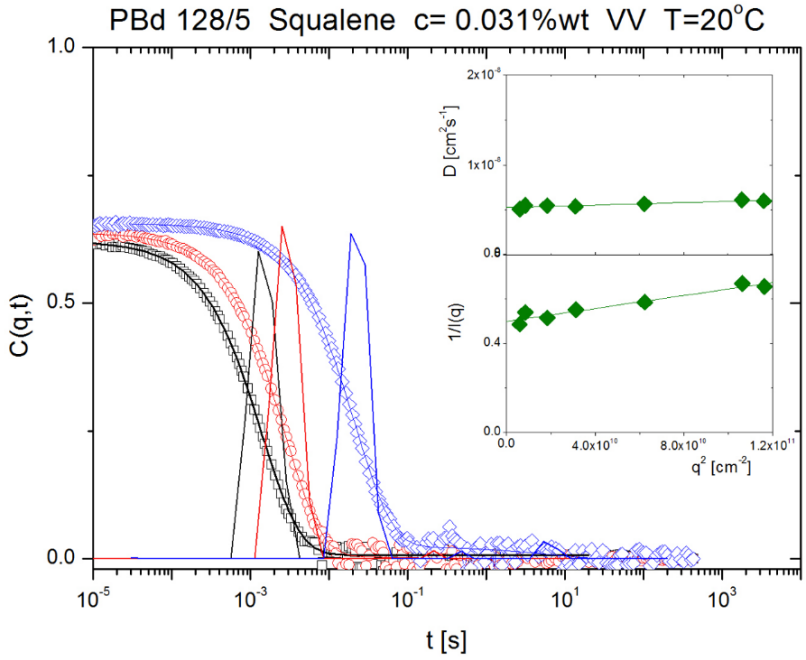

Figure III-1. Field auto-correlation functions at scattering angles of 150° (black squares), 90° (red circles) and 45° (blue diamonds) for a very dilute solution of polybutadiene (1,4-addition) star RS128PBD5 in squalene[1]. The lines through the data represent the fit based on the CONTIN analysis and the relaxation time distribution is also depicted. Inset: Diffusion coefficient (top) and inverse scattering intensity (bottom) as a function of the square of the wave vector.

In the dilute regime, the CONTIN analysis gives a narrow, unimodal relaxation time distribution, in agreement with the theoretical single-mode exponential decay. The diffusion coefficient associated with this characteristic decay rate (see chapter 2) is independent of the angle of observation. This proves that the scatterers are small compared to the scattering volume (flat region of the form factor at qR<1) and that the thermal motion is mainly coming from the translational diffusion of almost monodisperse scatterers. Therefore, we can associate this mode with the translational diffusion of the stars in the solution. Figure III-1 also shows the inverse intensity of the decay, which is slightly increasing at larger wave vectors.

When the concentration of stars is increased, additional relaxation modes appear in the field auto-correlation function (Figure III-2). The complexity of this function makes the analysis based on several exponential modes difficult, therefore the CONTIN analysis is the preferred option in this case. We observe that for this concentration (8.42 wt%), which is approximately half of the estimated c* (16.6 wt%) based on R_h, two to three

relaxation modes can be extracted from the data. The question of the number of modes able to best reproduce the C(q,t) data is usually left to the discretion of the user. The best technique usually consists in assuming the smallest number of modes able to correctly fit the data, in order to avoid over-fitting (each mode introduces new fitting parameters). Then, the user should consider all the available data at different concentrations and angles to rationalize the evolution of the different modes. Finally, it is almost impossible to differentiate between two modes if their characteristic times are less than a decade apart.

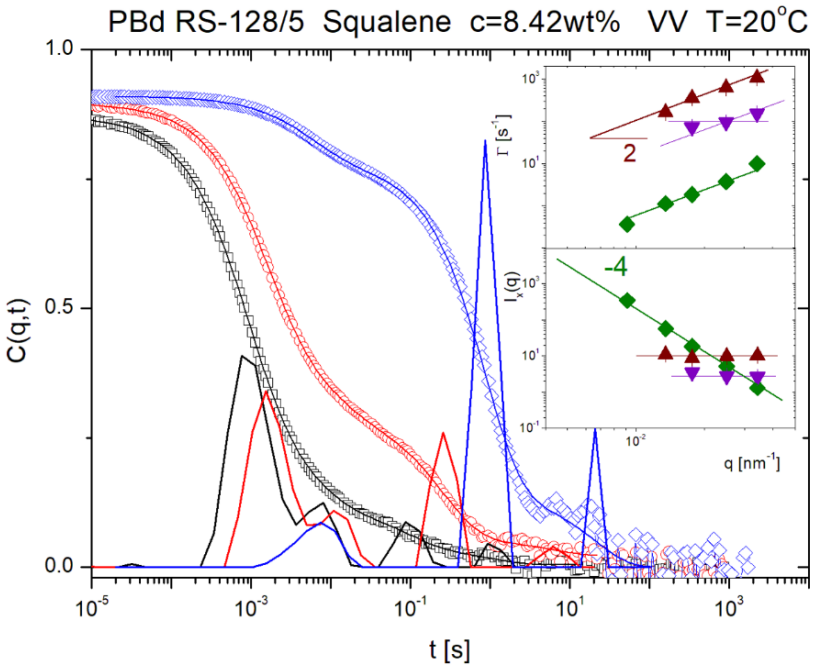

Figure III-2. Field auto-correlation functions at 150° (black squares), 90° (red circles) and 45° (blue diamonds) for a concentrated solution of the stars RS128PBD5[1]. The lines through the data represent the fit based on the CONTIN analysis, and the relaxation time distribution is also represented. Inset: Decay rate (top) and scattered intensity of each mode (bottom) as a function of the wave vector.

In this case, the application of the three guidelines outlined above has led to the decomposition of the auto-correlation function into three modes at high scattering wave vectors and only two modes at low scattering wave vectors. Indeed, the lower inset of Figure III-2 shows that the intensity of the slow mode (green) strongly depends on the observation angle: $I(q) \sim q^{-4}$. Therefore, at low values of the scattering wave vector the other faster modes are overwhelmed by the strong amplitude of the slow mode. The

decay rate of the slow mode is much slower than the other two, which makes its identification easier at all scattering wave vectors. The apparent square dependence of the decay rate on the scattering wave vector (Figure III-2, upper inset) suggests a translational diffusive behavior. All these observations strongly suggest the assignment of this mode to the diffusion of star clusters in the sample.

The first mode is also connected to a diffusive process ($\Gamma \sim q^2$) but its intensity does not depend on the scattering angle. The comparison of this mode to the data at lower concentrations (Figure III-3) shows that it probably comes from the cooperative diffusion of stars. However, unlike stars with lower functionality[3] (up to 128), the evolution of cooperative diffusion coefficient with concentration toward the de Gennes-Brochard[4] 0.75 slope is gradual, implying some difficulty in interpenetration due to the high osmotic pressure of the outer blobs that must be overcome ($\Pi \sim \xi^{-3} \sim f^{3/2}$ with ξ outer blob size[5,6]). The intermediate mode is peculiar. Neither its intensity not its decay rate seem to depend on the scattering wave vector, although the data are very limited. At low wave vectors, its magnitude is small compared to the slow mode and its decay rate becomes comparable to the one of the fast mode. Thus the reliable identification of this mode is difficult. From the available data, it may be possible to associate this mode with the non-diffusive motion of small scatterers, but the exact nature of this process remains unclear.

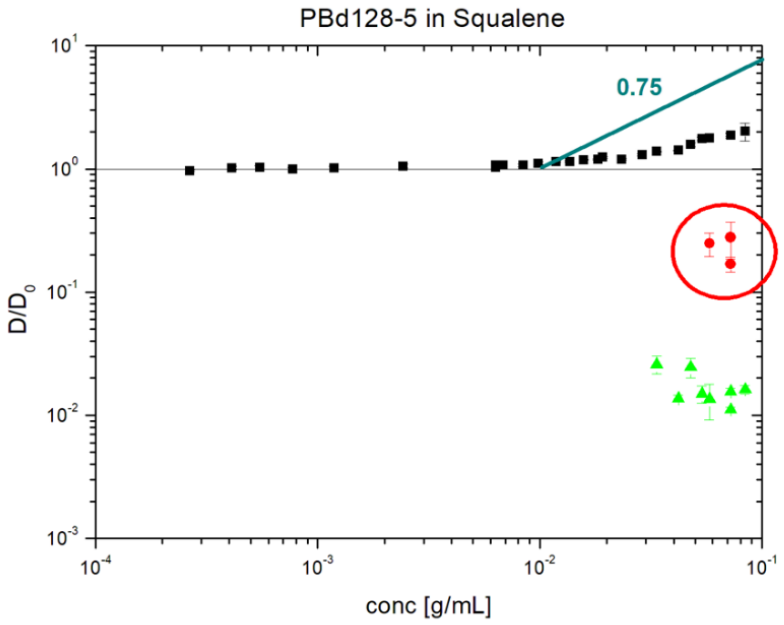

Figure III-3. Diffusion coefficient divided by the diffusion coefficient at infinite dilution as a function of the star concentration for the star RS128PBD5. Up to three modes can be identified: fast (black squares), intermediate (red circles) and slow (green triangles). The slope of 0.75 represent the expected theoretical increase of the cooperative diffusion coefficient of polymers.

Overall, we can distinguish two regimes based on the analysis of the auto-correlation functions. At low concentrations, up to around 6.10^{-3} g.mL^{-1}, the auto-correlation function exhibit only one mode and therefore only one associated diffusion coefficient (Figure III-3). This is what is usually referred to as the dilute regime. Upon increasing the concentration, stars start to interact with their neighbors and more modes appear in the auto-correlation functions. Above 3.10^{-2} g.mL^{-1}, a slow mode is clearly identified and attributed to the diffusion of star clusters. From 5.10^{-2} g.mL^{-1}, a third intermediate mode can be observed, although its physical meaning remains unclear. This analysis shows the complex interactions occurring in star solutions well below their theoretical overlapping concentration (0.17 g.mL^{-1} based on R_h) at which they start to solidify, This is mostly the consequence of the long range interaction of stars compared to hard spheres[7]. Therefore, even though the overlapping concentration may be a practical tool to compare different colloids, it remains a very superficial way to quantify the actual interactions between the particles, such that there are different ways to determine it.

III.3 – Rheo-DLS setup

In addition to their rich behavior at low and intermediate concentrations in the liquid state, star polymers also form aging solids above their overlapping concentration. In some cases, the linear rheological properties of the star glass can evolve significantly over long time scales[8]. The aging of soft glasses is usually associated with a change in its microstructure[9,10], hence the auto-correlation function of an aging glass should change with time. To properly measure the time-resolved auto-correlation function during the aging of a star polymer glass it is needed to design a simple shearing setup that can be adapted on the DLS instrument. Whereas there are several options, here we chose one driven by its overall simplicity and, we believe, usefulness. This setup can use shear to rejuvenate the sample placed in the DLS cuvette, which can then be followed over time during its aging.

The setup is composed of a long stainless steel shaft (homemade) connected to a geared DC motor (gearbox and motor from MFA COMO Drills, 941D Series) (Figure III-4a), such that the torque is sufficiently high to impose a steady shear on soft solids. The DC motor connects to a power supply (homemade) equipped with a potentiometer for the control of the input voltage and ultimately the angular velocity. The whole setup comprised of the shaft, the DC motor and the gears are supported by a plastic platform that precisely fits into the DLS instrument (Figure III-4b). The shaft can therefore fit exactly in the DLS cuvette (Hellma cuvettes from Hellma Analytics) containing the sample. The height of the shaft can be adjusted using a screw on the side of the motor (golden part on Figure III-4).

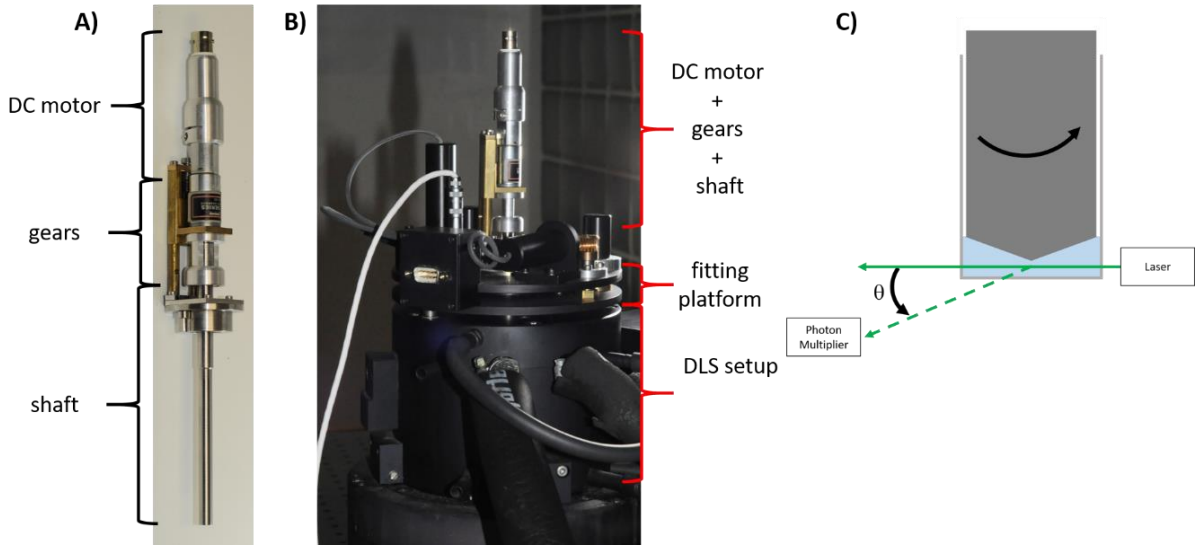

Figure III-4. A) Picture of the shearing device comprising the DC motor, the gears and the rotating shaft. B) The shearing device can be installed in the commercial DLS setup using the fitting platform to help with alignment. C) Representation of the trajectory of the laser beam inside the DLS cuvette. Photography and setup by A. Larsen[1].

The tip of the shaft in contact with the sample is a 6 mm stainless steel cone with an angle of 0.2 rad (11°). The previous design of this experiment was purposely off-centered such that the laser beam from the DLS setup would pass in the gap between the gap and the bottom plate. This version of the design was abandoned but the cone geometry was kept.

The speed of DC motor was first calibrated without any load to estimate the minimum and maximum rotation speed. It was then calibrated again using a solid suspension of microgels (described in chapter 2, c= 5 wt%) with a shear modulus of about 5 kPa as a dummy sample. The two calibration curves were very similar (Figure III-5), thus validating the possibility to reliably shear soft solids and yield stress fluids.

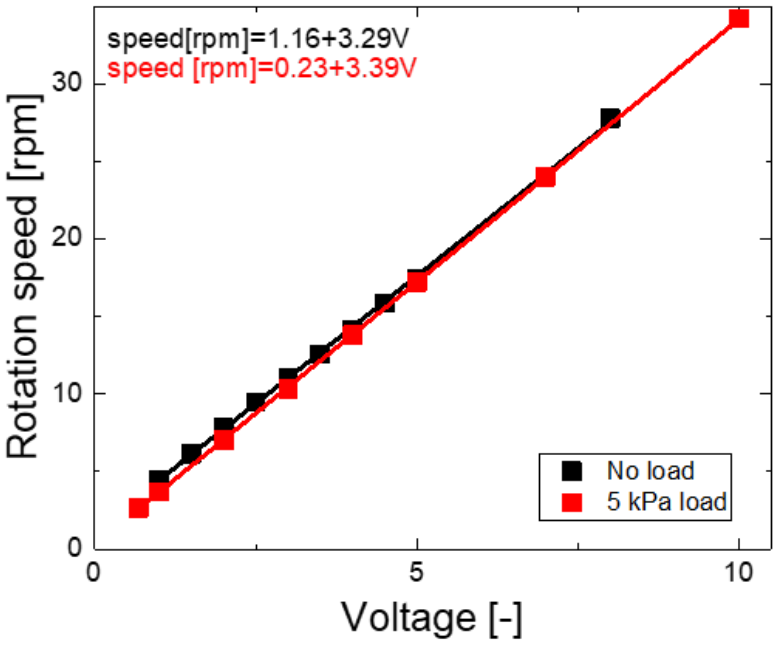

Figure III-5. Calibration of the DC motor angular velocity with (red) and without (black) load.

We used the ALV software to measure the DLS data. The synchronization between the shearing and the light scattering experiments was ensured by the simultaneous pressing of two buttons. The first was the key of the computer keyboard starting the DLS experiments. The second button was mounted on a long shaft and switched-on the DC motor power supply, such that it was possible to push the keyboard key with the motor switch. A timer connects the switch to the power supply to control the time at which the motor stops. It is also possible to delay the start of the DLS experiments, such that it only starts exactly when the shearing stops, with a precision of about 0.1s.

In practice, the shearing time is an input of the timer and the shearing speed is controlled by the power supply. When both buttons are pressed simultaneously, the shearing starts until the timer reaches 0. At this moment, the motor stops (no inertia was observed) and the light scattering experiment instantly starts. Therefore, we can measure the evolution of the auto-correlation function from the moment the shearing stops with a precision of about 0.1s.

Preliminary results obtained with a prior version of the rheo-DLS setup showed that the non-ergodicity of the aging sample is an issue. There are different solutions that can be proposed: It is possible to use the so-called “brute force” method[11] in which the same experiment is repeated multiple times while the sample is rotated between each experiment. This provides a way to recover the ensemble average in non-ergodic samples, however this method requires to repeat the experiment a large number of times, which often takes a very long time. Another solution is to use the echo technique[12,13], which requires to continuously turn the whole cell containing the sample. Then the auto-correlation of the scattered intensity is only carried out using the intensities that are measured at the same position for every period of rotation. This technique allows for the fast measuring of non-ergodic samples but loses the information about the correlation at fast times, since the fastest time scale is set by the time between two consecutive full rotations. Additionally, this technique requires a different correlator, and cannot be performed with the ALV instrument. A third solution is to use the multi-speckle method[11,14], in which thousands of scattering speckles are measured at the same time using a CCD camera, thus effectively recovering the ensemble average of the auto-correlation function. Although none of these techniques have been tried so far, we expect that the multi-speckle technique would be the easiest one to implement with this setup.

III.4 – Conclusions and perspectives

In conclusion, there are a few comments that should be made about the rheo-DLS setup described above. Although the shearing cell coupled with the DLS setup is working, the rheological results showing the strong aging effects of star solutions[8] could not be reproduced, mostly because of the lack of the sample available at that time.

Improvements can also be made on the design of the hardware supporting the DC motor, such as the implementation of screws to facilitate the alignment of the shaft in the DLS cuvette. In addition, the cone geometry should probably be reworked, since the gap control lacks the accuracy necessary for the cone-and-plate geometry to truly have an advantage compared to the parallel plate geometry. Finally, the implementation of the echo technique would require a complete change of the instrument, since our current ALV instrument is not able to perform this experiment. Although possible, this would require

a very large amount of work for trained users, therefore the multi-speckle method would probably be more efficient to tackle the non-ergodicity problem.

References

(1) Antje Larsen. (Unpublished Data). **2019**.

(2) Stephen W. Provencher. CONTIN: A General Purpose Constrained Regularization Program for Inverting Noisy Linear Algebraic and Integral Equations. *Computer Physics Communication* **1982**, *27*, 229–242.

(3) Semenov, A. N.; Vlassopoulos, D.; Fytas, G.; Vlachos, G.; Fleischer, G.; Roovers, J. Dynamic Structure of Interacting Spherical Polymer Brushes. *Langmuir* **1999**, *15* (2), 358–368. https://doi.org/10.1021/la980794j.

(4) Brochard, F.; de Gennes, P. G. Dynamical Scaling for Polymers in Theta Solvents. *Macromolecules* **1977**, *10* (5), 1157–1161. https://doi.org/10.1021/ma60059a048.

(5) Voudouris, P.; Choi, J.; Dong, H.; Bockstaller, M. R.; Matyjaszewski, K.; Fytas, G. Effect of Shell Architecture on the Static and Dynamic Properties of Polymer-Coated Particles in Solution. *Macromolecules* **2009**, *42* (7), 2721–2728. https://doi.org/10.1021/ma802878r.

(6) Witten, T. A.; Pincus, P. A.; Cates, M. E. Macrocrystal Ordering in Star Polymer Solutions. *Europhysics Letters (EPL)* **1986**, *2* (2), 137–140. https://doi.org/10.1209/0295-5075/2/2/011.

(7) Likos, C. N.; Löwen, H.; Watzlawek, M.; Abbas, B.; Jucknischke, O.; Allgaier, J.; Richter, D. Star Polymers Viewed as Ultrasoft Colloidal Particles. *Phys. Rev. Lett.* **1998**, *80* (20), 4450.

(8) Erwin, B. M.; Vlassopoulos, D.; Cloitre, M. Rheological Fingerprinting of an Aging Soft Colloidal Glass. *J. Rheol.* **2010**, *54* (4), 915–939. https://doi.org/10.1122/1.3442901.

(9) Cloitre, M.; Borrega, R.; Leibler, L. Rheological Aging and Rejuvenation in Microgel Pastes. *Phys. Rev. Lett.* **2000**, *85* (22), 4819–4822. https://doi.org/10.1103/PhysRevLett.85.4819.

(10) Stiakakis, E.; Wilk, A.; Kohlbrecher, J.; Vlassopoulos, D.; Petekidis, G. Slow Dynamics, Aging, and Crystallization of Multiarm Star Glasses. *Phys. Rev. E* **2010**, *81* (2), 020402. https://doi.org/10.1103/PhysRevE.81.020402.

(11) Cipelletti, L.; Ramos, L.; Manley, S.; Pitard, E.; Weitz, D. A.; Pashkovski, E. E.; Johansson, M. Universal Non-Diffusive Slow Dynamics in Aging Soft Matter. *Faraday Discussions* **2003**, *123*, 237–251. https://doi.org/10.1039/b204495a.

(12) Pham, K. N.; Egelhaaf, S. U.; Moussaïd, A.; Pusey, P. N. Ensemble-Averaging in Dynamic Light Scattering by an Echo Technique. *Review of Scientific Instruments* **2004**, *75* (7), 2419–2431. https://doi.org/10.1063/1.1753105.

(13) Petekidis, G.; Moussaïd, A.; Pusey, P. N. Rearrangements in Hard-Sphere Glasses under Oscillatory Shear Strain. *Physical Review E* **2002**, *66* (5). https://doi.org/10.1103/PhysRevE.66.051402.

(14) Cipelletti, L.; Weitz, D. A. Ultralow-Angle Dynamic Light Scattering with a Charge Coupled Device Camera Based Multispeckle, Multitau Correlator. *Review of Scientific Instruments* **1999**, *70* (8), 3214–3221. https://doi.org/10.1063/1.1149894.